University of Alberta

Development of a Shape Memory Alloy Actuator for an Intelligent Eye Prosthesis

by

Tonya Bunton

A thesis submitted to the Faculty of Graduate Studies and Research in partial fulfillment of the requirements for the degree of Master of Science.

Department of Mechanical Engineering

Department of Biomedical Engineering

Edmonton, Alberta

Fall 2002

National Library of Canada
Acquisitions and Bibliographic Services
395 Wellington Street
Ottawa ON K1A 0N4
Canada

Bibliothèque nationale du Canada
Acquisitions et services bibliographiques
395, rue Wellington
Ottawa ON K1A 0N4
Canada

Your file Votre référence

Our file Notre référence

The author has granted a non-exclusive licence allowing the National Library of Canada to reproduce, loan, distribute or sell copies of this thesis in microform, paper or electronic formats.

L'auteur a accordé une licence non exclusive permettant à la Bibliothèque nationale du Canada de reproduire, prêter, distribuer ou vendre des copies de cette thèse sous la forme de microfiche/film, de reproduction sur papier ou sur format électronique.

The author retains ownership of the copyright in this thesis. Neither the thesis nor substantial extracts from it may be printed or otherwise reproduced without the author's permission.

L'auteur conserve la propriété du droit d'auteur qui protège cette thèse. Ni la thèse ni des extraits substantiels de celle-ci ne doivent être imprimés ou autrement reproduits sans son autorisation.

0-612-81375-4

Canada

University of Alberta

Library Release Form

Name of Author: **Tonya Bunton**

Title of Thesis: **Development of a Shape Memory Alloy Actuator for an Intelligent Eye Prosthesis**

Degree: **Master of Science**

Year this Degree Granted: 2002

Permission is hereby granted to the University of Alberta Library to reproduce single copies of this thesis and to lend or sell such copies for private, scholarly or scientific research purposes only.

The author reserves all other publication and other rights in association with the copyright in the thesis, and except as herein before provided, neither the thesis nor any substantial portion thereof may be printed or otherwise reproduced in any material form whatever without the author's prior written permission.

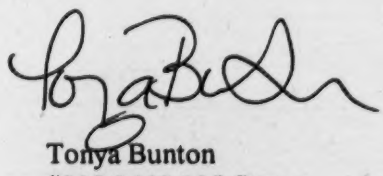

Tonya Bunton
#205 9640 105 Street
Edmonton, Alberta
T5K 0Z7

July 10, 2002
Date submitted to the Faculty of Graduate Studies and Research

University of Alberta

Faculty of Graduate Studies and Research

The undersigned certify that they have read, and recommend to the Faculty of Graduate Studies and Research for acceptance, a thesis entitled **Development of a Shape Memory Alloy Actuator for an Intelligent Eye Prosthesis** submitted by Tonya Bunton in partial fulfillment of the requirements for the degree of Master of Science.

Dr. M.G. Faulkner (Supervisor)

Dr. J. Wolfaardt (Co-Supervisor)

Dr. D. Raboud

Dr. R. Eadie

Date: July 8/02

Abstract

The quality of life of patients who have undergone an exenteration of the orbit and wear an orbital prosthesis would be improved if the ocular section of their prosthesis were made more realistic by means of vertical and horizontal motion. A method of actuation that fits the design constraints of an orbital prosthesis and mimics movement of the normal eye is currently not available. This thesis develops a system that meets the design constraints and follows a design philosophy of biomimicry, simplicity and space optimization. Various methods of actuation were considered, and shape memory alloys (SMA) were chosen for their high power density and high displacements. The behaviour of SMAs as an actuator was investigated including the forces delivered, the transformation temperatures and the thermomechanical processing. Forces up to 1.3 N were obtained with SMA springs. Pulse width modulation was chosen to control the SMA springs, where combinations of current, frequency and duty cycle achieved a rotation of the ocular element of ±30° from neutral. A prototype model with movement in the horizontal direction was constructed to validate the design.

Acknowledgements

Without Eric and his unconditional support and love, I would have been back at Dofasco making steel. To him, I am grateful for his observations to the many stages required in completing a thesis and for imposing breaks to the self-induced stress. And for believing in me.

I would like to thank Dr. Gary Faulkner, for his understanding though the surgeries, World Games, Girl Guides, trips to Ontario and general insanity in the writing of this thesis. You are a true free spirit.

A special thank you to my other dungeon dwellers Steve Hurst, Kristin Miller, Ryan Swain, Demetri Giannitsios, Kajsa Duke and Karla Collinge.

Thanks to Dave Pape in the shop for much patience in the many iterations to get from the initial concept to the final design.

And thank you to my mom and dad, Elizabeth and David, for guiding me though all of the paths of life; who knew that I'd end up out here?

Contents

1 Introduction

1.1 Overview of Problem 2

1.2 Overview of Thesis 4

2 Selected Design

2.1 General Design Criteria 8

2.2 Philosophy of Design 9

2.3 Actuator Feasibility Study 10

2.3.1 Traditional Motors 10

2.3.2 Microelectromechanical Systems 11

2.3.3 Thermal, Phase Transformation and 'Smart' Actuation Systems 15

2.4 Actuator Selection 20

2.5 Background on Shape Memory Alloys 21

2.5.1 Metallurgy 21

2.5.2 Constitutive Models of Shape Memory Alloys 23

2.5.3 Processing for Design 25
2.6 Design Constraints of Shape Memory Alloys 26
2.7 Development of Design 26
2.8 Final Design 28

3 Analysis of Proposed Design
3.1 Force Model of the Design 37
3.1.1 Moment Return Requirements 39
3.1.2 Attachment Point and Stroke 42
3.1.3 Moment of Inertia of Rotary Components 43
3.1.4 SMA Force Requirements 44
3.2 Heat Transfer Between the SMA Spring and Surroundings 44
3.3 Spring Design 47

4 Experimental Considerations
4.1 SMA Spring Actuator Construction 63
4.2 Determination of Transformation Temperatures 66
4.3 Spring Characterization Apparatus 67
4.3.1 Isothermal Force-Displacement Equipment 67
4.3.2 Pulse Width Modulation 69

5 Results and Discussion
5.1 Actuation Forces of the SMA Spring 77
5.2 Current Activation by Pulse Width Modulation (PWM) 80
5.3 Transformation Temperatures 82
5.4 Prototype Validation 87

6 Conclusions and Future Research

6.1 Conclusions of Current Work 101

6.2 Future Research 102

References 104

Appendix A: Detailed Analysis of Heat Transfer Coefficient 108

Appendix B: Validation of Negligible Deflection at Cantilever Beam End 111

Appendix C: Electrical PWM Circuit Diagrams 114

Appendix D: CAD Drawings of Prototype Design 120

List of Tables

Table 2.1: Comparison of Energy Density for various actuators 21

Table 3.1: Changes made to geometry of triangular cam bias element 41

Table 4.1: Anneal cycles used for spring construction 64
Table 4.2: Flexinol™ SMA Wire Properties 65

Table 5.1: Transformation temperature estimated by the water bath apparatus 80
Table 5.2: Results of DSC analysis for austenite transformation temperatures for thermomechanical treatments of Flexinol™ SMA 83
Table 5.3: Results of DSC analysis for the transformation temperatures from As-Is Flexinol™ SMA 83
Table 5.4: Transformation temperatures SMA springs 85
Table 5.5: Summary of angle of rotation available for PWM variables with an input current of 0.8A 88

List of Figures

Figure 1.1: An orbital prosthesis in situ in a cast 6

Figure 2.1: A mold of a typical exenterated orbit 30
Figure 2.2: Schematic of the anatomy of the eye 30
Figure 2.3: Schematic of the NanoMuscle® 31
Figure 2.4: Thermal cycle of SMA with respect to crystal type 32
Figure 2.5: Location of transformation temperatures of SMA 33
Figure 2.6: Stress-strain behaviour of austenite and martensite 33
Figure 2.7: General relationship between stress and temperature of SMA 34
Figure 2.8: Schematic of maximum possible rotation with SMA wire 34
Figure 2.9: Schematic of the SMA actuated orbital eye prosthesis 35

Figure 3.1: Length of initial SMA spring 51
Figure 3.2: Detail of changes in length of SMA spring with respect to angle of rotation 51
Figure 3.3: Detail of free body diagram about the pivot 52
Figure 3.4: Cantilever beam bias return element 53
Figure 3.5: Schematic of the active bias spring element 53
Figure 3.6: Schematic of moment calculation 54
Figure 3.7: Expected moments of elliptical cantilever beam bias element 54
Figure 3.8: Schematic of the rectangular cantilever bias element 55
Figure 3.9: Expected moments of rectangular cantilever beam bias element 55
Figure 3.10: Schematic of the triangular cam shaped bias element 56
Figure 3.11: Moment of triangular cam bias spring and effects of geometry on the moment 56
Figure 3.12: Detail of triangular element within a rotation of 10° 57
Figure 3.13: Schematic of spring bias element with triangular cam 57

Figure 3.14: Calculated moment for bias system with springs and triangular element 58
Figure 3.15: Stroke-attachment point relationship 58
Figure 3.16: Stroke of the SMA spring required for eye rotations between 10° and 30°, based on attachment point 59
Figure 3.17: Expected shear strain in terms of attachment point for angles of rotation between 10° and 30° 59
Figure 3.18: Predicted minimum force required by SMA spring to rotate eye based on attachment point 60
Figure 3.19: Predicted heating for SMA wires in still air for 250μm wire and the 100μm wire at various current inputs 60
Figure 3.20: Predicted cooling behaviour for the 100μm wire in still air and the 250μm wire in forced air 61
Figure 3.21: Heating cycle of SMA actuator 61

Figure 4.1: Phase diagram and corresponding time-temperature-curve for NiTi 71
Figure 4.2: Schematic of apparatus for setting SMA springs 71
Figure 4.3: Example of output from DSC 72
Figure 4.4: Isothermal force displacement apparatus 73
Figure 4.5: Calibration of strain gauges on cantilever beam 74
Figure 4.6: Step output of PWM denoting frequency and duty cycle 74
Figure 4.7: Schematic of PWM circuit 75
Figure 4.8: Assembly for PWM experimentation of SMA spring 75

Figure 5.1: Isothermal Force-Displacement results for Spring 250-2.38-65 89
Figure 5.2: Isothermal Force-Displacement results for Spring 250-2.38-20 89
Figure 5.3: Shear stress-strain relationship for Spring 250-2.38-20 90
Figure 5.4: Isothermal Force-Displacement Results for Spring Spring 100-0.8-55 90
Figure 5.5: Change in mechanical properties with temperature 91
Figure 5.6: Isostrain relationship between stress and temperature to estimate transformation temperatures 91
Figure 5.7: Change in transformation temperatures with differing initial strains on Spring 250-2.38-65 92
Figure 5.8: Change in force with increasing duty cycle for Spring 250-2.38-20 92
Figure 5.9: Increase in force with frequency based on duty cycle 93
Figure 5.10: Actuation Speed with frequency based on duty cycle 93
Figure 5.11: Step-like force changes for Spring 250-2.38-20 with low frequency, and increase in force with increase in stroke 94

Figure 5.12: Transformation tempertures for Flexinol™ 250μm high temperature SMA at anneal temperatures up to 500°C 94
Figure 5.13: Transformation tempertures for Flexinol™ 250μm low temperature SMA at anneal temperatures up to 500°C 95
Figure 5.14: DSC output for high temperature material annealed at 500°C for 15 minutes Flexinol™ 250μm 95
Figure 5.15: DSC output for high temperature material annealed at 400°C for 15 minutes Flexinol™ 250μm 96
Figure 5.16: Photographs of the Prototype model 97
Figure 5.17: Top view of prototype in active state 98
Figure 5.18: Full view of active system 99

1 Introduction

The motivation for developing an intelligent orbital prosthesis is presented in terms of the needs of the patients of the Craniofacial Osseointegration and Maxillofacial Prosthetic Rehabilitation Unit (COMPRU) at the Misericordia Hospital in Edmonton, Alberta. The developments to date of a realistic ocular prosthesis are presented. The scope of this thesis with respect to the development of an actuation system for movement of the ocular prosthesis element of an orbital prosthesis is discussed.

1.1 Overview of Problem

Patients who have either been born with head and neck deformities, or those who have lost these features due to cancer or injury, have the option of wearing a prosthesis to aid in rehabilitation. COMPRU specializes in the reconstruction of head and neck features. Their mandate is to help these people reintegrate back into society through surgery, prosthesis construction, audiology and speech pathology, and psychological rehabilitation.

A significant amount of research has been completed, and is currently in progress, to create an orbital prosthesis that appears as realistic as possible. In the past, prostheses were attached to the skin with adhesives or held in place with mechanical retention such as with spectacle frames. Without reliable and predictable retention, the prosthesis was not secure and this limited usefulness of the prosthesis to patients. A more permanent and secure method of prosthesis retention was developed to improve the value of facial prostheses to patients.

An implant technology, initially used for tooth replacement, was developed by Professor P.I. Brånemark in Gothenburg, Sweden. A titanium implant is inserted in the bones of the face, and after a healing period to establish osseointegration, the implants are connected to percutaneous abutments. The facial prosthesis is retained by magnetic or mechanical means to the percutaneous abutments. This provides a reliable retention of the facial prosthesis and prevents displacement of the prosthesis. Development of secure retention of the facial prosthesis is thought to provide improved confidence for the patient.

The construction of a facial prosthesis is not a trivial process. Several complex processes have been developed to create a prosthesis that replicates the patients original facial features. Spectrophotometry and computerized colour matching allows for the silicone prosthesis to match the colour of the patients' skin. Rapid

prototyping has been incorporated to precisely dimension the prosthesis to assist replication of the patients' facial features.

Other research activities investigate surgical techniques, the biomechanics of craniofacial osseointegrated implants, psychological assessments, and basic science studies on the skin-implant interface. All of these endeavours have led to aesthetically excellent but static prostheses, an example of which is shown in Figure 1.1. For an orbital prosthesis in particular, this is very limiting to the value of the prosthesis for a patient. Patients complain that the static ocular element is aesthetically displeasing and causes distraction during social interaction. A common complaint is that during conversation others are distracted by the fixed gaze of the orbital prosthesis.

To better understand the patients' views and desires, a study was conducted to ask what would make the orbital prosthesis more realistic. This study was organized by the anaplastologists at COMPRU and was directed at their patients who wore an orbital prosthesis in the spring of 2001. Patients rated their main desires as return of vision, horizontal and vertical eye movement, and eyelid blinking. The development of a blinking eyelid dates to Alexandridis in 1976 (Miranda and Habakuk, 2000), who incorporated the electronics in an eyeglass frame and used an electromagnet for actuation. Recent research (Honda et al, 1999, and Klein et al, 1999) has used surface mounted technology, including the Brånemark implants to retain the actuator and electronics. In addition, the signal was obtained by a surface electromusculogram (EMG) which would detect the contraction of the ocular muscles. The major problems in this application included housing the power supply, miniaturization of the actuation unit and determining a reliable method for obtaining the blink muscle reflex.

Dobelle (2000) has developed a method of delivering vision to blind patients by means of a sub-miniature TV camera. The camera is supported on the lens of eyeglasses and sends a signal to an electrode array implanted on the surface of the

right occipital lobe. Patients have been reported to 'see' black and white images, including letters of the alphabet. This technology could be used to return vision of the patients missing eye. However, this research was conducted on for completely blind patients, not those with one functional eye.

COMPRU is heading a project with the Department of Mechanical Engineering and the Department of Electrical Engineering at the University of Alberta to produce an orbital prosthesis in which the ocular element can follow the movement of the functional eye by moving in the horizontal and vertical directions. The control system, utilizing the concepts of electrodes to capture the ocular muscles signal, is under development in the Department of Electrical Engineering. The electro-oculogram signal obtained from the existing orbital muscles will be conditioned in order to determine the rotation of the functional eye (Gu, Meng, Cook and Faulkner, 2001). This conditioned signal provides a reference for the rotation of the prosthetic eye to follow the functional eye. The development of the actuation system is the subject of the current thesis.

1.2 Overview of Thesis

In Chapter Two, the general design criteria desired by COMPRU for the robotic orbital prosthesis and the design philosophy aided in the selection of an actuation system. A feasibility study revealed that shape memory alloys had the greatest potential as a potential actuator.

Chapter Three investigates the design of the support structure for the robotic eye as well as the actuation system by considering both the forces the shape memory alloy could obtain and that of the design bias spring. Heat transfer of the shape memory alloy element was studied to predict the actuation cycle time.

The equipment required to measure the forces that are delivered by the shape memory element are discussed in Chapter Four. The development of a control system using pulse width modulation was examined.

The forces obtained from the SMA springs from the experimental apparatus are analyzed in Chapter Five to produce a five-times life prototype model for motion only in the horizontal direction.

Conclusions regarding this project are found in Chapter Six, and topics of further investigation are briefly discussed.

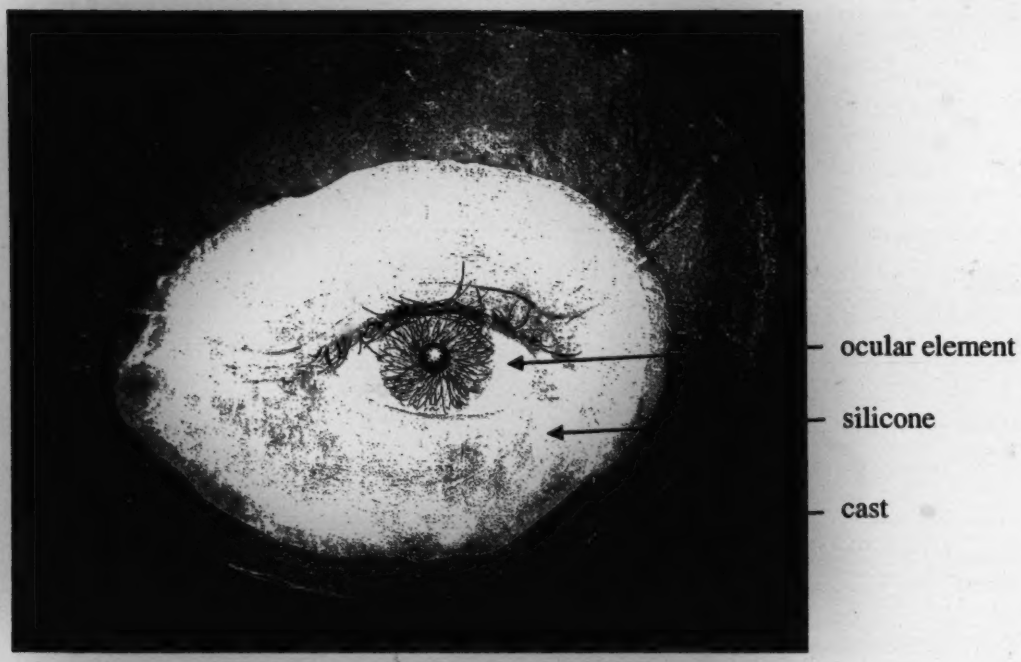

Figure 1.1: An orbital prosthesis in situ in a cast. Note that the ocular element is held in a fixed position within the silicone body of the orbital prosthesis. Since the body of the ocular element is in a fixed position, it is typically positioned in a forward downward gaze.

2 Selected Design

The evolution of the design of the actuator component of the robotic orbital prosthesis is discussed. The general design criteria imposed by COMPRU and their patients' served as the initial constraints to focus the design. The design philosophy, which considers biomimicry, simplicity and space optimization, is explained followed by a feasibility study of the potential techniques of actuation including electric motors and a magnetic system. It is believed that shape memory alloys have the greatest potential for this actuation system. The background into the behaviour of these novel materials is reviewed. The constraints on the design due to the incorporation of shape memory alloys are given with a description of the final actuation design.

2.1 General Design Criteria

The general criteria suggested by COMPRU and their patients for the robotic orbital prosthesis indicated that the operation of the ocular element, including all supporting components, should reside inside the prosthesis. This was to be done such that the actuation unit cannot be detected by the patient or by observers. Shown in Figure 2.1, is a mold of a typical orbital exenteration which reveals the dimensional constraints of the project.

To accomplish this general goal, the specific design criteria which were used in the initial stages were:

- To use an actuator which is undetectable by the patient by vibrational, electrical or thermal means;
- To restrict the size of the system to a maximum depth of 30 mm and width of 30 mm so that the actuator could fit into the orbital defect;
- That the entire prosthesis was to be sealed from the environment;
- That the actuation of the ocular element not lag that of the functional eye such that it would be visibly noticeable;
- That the actuator provide a rotation of the ocular element of ±30° from a neutral position (looking forward);
- That the ocular element and prosthesis could be altered from the present stationary design as long as the entire prosthesis is not greater than the volume of the orbit.

Specific criteria such as quantifying range, frequency, ocular velocity and acceleration, and load could be developed as the design progressed.

2.2 *Philosophy of Design*

The overall philosophy of the actuator design was based on three factors: biomimicry, simplicity and space optimization.

Biomimicry is a concept that is used when engineering designs and processes are modelled after biological processes (Benyus, 1997). In the eye, the extraocular muscles are linked in three pairs of agonist and antagonist muscles to provide vertical, horizontal and rotary motion. These muscles attach to the sides of the ocular globe and converge at a point behind the eye, as shown in Figure 2.2. Electrical potentials from the brain are sent along neurons to cause the muscles to contract and pull the eye to the desired direction, with a particular force and for a certain duration. The force of the contraction process is significantly larger than the relaxation process. The objective of the actuator would be to mimic the contraction of a muscle upon stimulation of the actuator.

To simplify the design, and to mimic the eye muscles, no gears or electric motors were to be utilized in the actuator. The number of components was to be minimized so as to diminish the possibility of actuator failure.

The actuator was to utilize the space inside the hemisphere of the ocular element. It was also suggested that the mechanical structure be designed so that it contains the ocular element and the entire actuation system. These components would be independent of the exterior silicone prosthesis. Since the available space is minimal, the power required to activate the actuator must also be minimized. The power supply would, most likely, have to be housed within the prosthesis, and as a result, there would be a balance between the size of the power supply and the size of the actuator. Ideally it was hoped that the actuator would have a high power to density ratio which will optimize the power available in the space of the prosthesis orbit.

2.3 *Actuator Feasibility Study*

Actuators are devices that produce motion in the form of a force or torque that creates displacement or acceleration on another body. Actuators vary in size from atomic to large structures, and are designed according to the limitations in place for their application. A number of actuators, which could be considered as potential systems for the orbital prosthesis, were identified. These are discussed considering the general design criteria and the design philosophy.

2.3.1 Traditional Motors

The traditional methods of actuation include solenoids, electric motors, and hydraulic and pneumatic cylinders. Solenoids and electric motors operate on the basis of electromagnetic forces which are produced when a current is moved within a magnetic field. The force created is perpendicular to that of the current and magnetic fields. Hydraulic and pneumatic cylinders have a piston which is forced to move by the presence of fluid or air in a constrained chamber.

- Solenoids are difficult to control and are most appropriate for on-off switch applications. Since the robotic orbit will need continuous control to mimic eye movements, solenoids were not considered appropriate.

- Electric motors could provide the required force given the size and power constraints. A gear box would have to be coupled with the motor to obtain the required torques and speeds. The addition of the gear box increases the number of components of the actuation system, and is undesirable from the simplicity philosophy. In addition, the rotary motion of these motors inevitably causes vibration of the system. As the motor is housed inside the orbital defect of the patient, these vibrations would be a significant annoyance to the patient. In addition, the high start torques of

the motors result in a high start acceleration, which is also unnatural to the movement of the eyes.

- A light servomotor (LightServoNG, WES-Technik GmbH, Oberboihingen, Germany), was used to actuate the ocular element in prior investigations. At 2.4 g, these motors are thought to be the lightest servomotors available internationally, and can deliver a maximum output force of 1.7 N with use of less than 100 mA of current and 3 to 5 V. The maximum deflection of 14 mm can be achieved in 0.2s. However, there was a significant amount of vibration caused by the servomotor.

- In another example, the Super Micro RC Motor (#3-787, Mondo-tronics, Inc., San Rafael, CA, USA) delivers a torque of 17.8 Nm, requires 4.8 V, and is approximately 2.32 cm x 1.3 cm x 2.5 cm, with a mass of 14 g. Power requirements were in the order of 0.5 W to 3 W. Essentially, the size of the motor consumed the entire volume of the prosthesis within the orbital defect space.

- The hydraulic and pneumatic systems require many components: a pump, a pressure regulator, valves, a distribution system and a linear or rotary actuator. These systems are too complex and do not readily adapt to the space requirements for the orbital prosthesis.

2.3.2 Microelectromechanical Systems

Microelectromechanical system (MEMS) is a new term that brings together interdisciplinary fields of engineering, including mechanics, electronics and electrical components to support a control system applied on a micrometer scale.

Many of these types of actuation methods are considered to be two dimensional due to their small size.

MEMS are being explored as the traditional methods of actuation are not applicable to small sized problems. This category of actuation produces displacements in the order of micrometers, and so is not sufficient for actuation of the orbital prosthesis. The MEMS technologies are novel, and could possibly be modified for a prosthesis sized system.

- Piezoelectric materials have the ability to deform when an electric voltage is applied, as well as to produce an electric voltage when deformed. Piezoelectric crystals have been limited to applications where low displacements are required at high frequencies. These crystals can be used by applying a high voltage to obtain a displacement, or by deflecting the crystal to obtain a high voltage. Piezoelectrics are widely used in vibration control and load sensors.

  - A step like motor can be made of piezoelectric crystals which can obtain displacements in the order of 6 μm over a 1 cm length of the material. Even though the forces obtained by piezoelectrics are in the order of 450 N, the displacements required to rotate the prosthetic eye are in the order of millimetres and a crystal with a sufficient length change would exceed the space constraint of the prosthesis.

  - An inchworm motor made of a piezoelectric stack has been able to overcome the small displacements of a single piezoelectric crystal. Traditional inchworm motors would not be applicable in the scale of the prosthetic eye application as they create displacements in the order of micron, which is not suitable for the prosthetic eye. However, an actuator called the Penn State H3C (Galante et al., 1999), which is an

acronym for high force, high displacement and high energy density, overcomes traditional micron displacements.

The inchworm consists of three parts: two clamping mechanisms and one pusher. The motor 'inches' along a linear path by alternating between the clamping and pushing modes. The function of the pusher is to transmit the actuation force into an external displacement. The Penn State H3C can produce a holding force of 200 N at a maximum stroke of 6 mm. It was reported that the maximum velocity of the unit is 5.4 mm/s at a drive frequency of 900 Hz. The complete dimensions of the H3C are 40 mm x 60 mm x 20 mm. This illustrates that as the mechanism is scaled up from micro- to milli-size in order to produce the force or displacement required to rotate the ocular unit, that the volume of the mechanism exceeds the volume inside the prosthesis and as a result, the piezoelectric inchworm motor could not be considered for the application.

- Koga and Suzumori (1999) have developed an electrostatic linear microactuator for use in focusing cameras at the end of an endoscope. These actuators have two stators with four two-phase comb-electrodes and a slider between the stator. By applying a voltage to the electrodes, a slider vibrates between the stators which results in a macroscopic displacement. Operational problems include accumulated charge on the stator. The dimensions of the microactuator are 8 x 8 x 1.2 mm, and the stroke of the unit is 1 mm. With the application of 100 V, an output velocity of 2.0 mm/s and an output force of 0.18 mN are obtained. The force output of the electrostatic linear microactuator is not sufficient to rotate the ocular unit.

- A linear drive using thin magnetic layers was proposed by Kube et al. (2000). Electromagnetic actuators are simple as there are no bearings in the design. These actuators operate by magnetic forces between moving and resting parts.

The magnet used was Neodymium-Iron-Boron (a rare earth permanent magnet) at a size of 50 x 50 x 1 mm. Forces of 1.5 N were produced using 10 A of current. The force depends of the magnetic flux density, the current and the length of the wires. Movements of up to 50 mm were reported. The temperature of the magnetic layers increases during operation due to the imposed current. The maximum working temperature was 100°C, so the working time was limited to a few minutes. The force of the electromagnetic actuators is adequate, however, continuous operation of the actuation over a time period of a few minutes would be required. Since the orbital prosthesis would be in operation for more than a few minutes at a time, this configuration is not applicable.

- An actuator composed of electromagnetic elements was constructed by Torii, Kato and Ueda (2001). A Y-shaped rotor, with legs made of piezoelectric crystals wound with wire has been shown to move with three degrees of freedom. The electromagnets hold the actuator to the floor and the piezoelectric element pushes the unit. The large electromagnetic forces produced by the magnets can hold the actuator on an incline. The application for this actuating system has been for precision positioning systems. Linear motion and rotation is achieved by applying voltage to various legs of the Y-shaped frame, in sequence. The size of the unit is described as 5 mm in diameter. The forces produced were up to 2.7 N, with linear displacements of 20 μm in 6 s. This actuator possesses potential, as the force range and size are ideal. It could be assembled on the inner surface of the ocular element and would act to move the iris around on the outer surface of the ocular. However, the displacement of the device is considerably less than required.

2.3.3 Thermal, Phase Transformation and 'Smart' Actuation Systems

Non-traditional actuators may utilize thermal and phase transformation energy to produce actuation. These actuators are generally free of mechanical machines such as gears and pumps.

Critical issues are response and recovery time. Heat conduction occurs through diffusion into the surrounding element, which is governed by Fourier's law. Dependent variables are the temperature distribution, the conduction area and the coefficient of heat conductivity of the heated element. Transfer of heat can be accelerated with forced convection. Heat transfer is dependent mainly on the difference in temperature between the element and the surrounding medium. The speed of the actuator is dependent on both the time to heat the element to a specific temperature and the time required to remove the heat from the element.

- When gases are heated, they expand. If the gas is contained within a certain volume where one side of the volume is a flexible diaphragm, when the gas expands, it will exert a pressure against a diaphragm resulting in a displacement. Such examples are thermo-pneumatic micro pumps for delivering microlitres per minute of fluids in pharmaceutical applications and thermal inkjet print heads (Tabib-Azar, 1998). A system for heating and pressurizing the gas is required, and this is thought to be too complex for orbital prosthesis actuation. In addition, the amount of displacement available is not sufficient for the desired rotation.

- Electrorheological fluids are composed of small particles suspended in organic oils. These particles control the fluids' ability to support shear stress upon application of an electric field. These aggregates, in the order of 1 to 10 μm, can prevent fluid flow at lower stresses. An electric field will cause fibrils, which are small chains, to form in the fluid in the direction of the field.

The fibrination, which occurs in a few milliseconds, prevents any fluid motion. When the field is released, the fluid can flow and a shear strain occurs in the fluid. Reapplying the electric field normal to the fluid flow will cause fibrils to form, and some fibrils are immediately broken due to the motion of the fluid. The fibrils continue to reform as the field as applied. The breaking and reforming of these chains leads to a controlled force resistive mechanism. The shear stress increases with increasing field strength. Electrorheological fluids have been shown to have excellent potential in active vibration control (Bandyopadhyay, 1999).

Magnetorheological fluids are similar to electrorheological fluids, except they are activated by the application of a magnetic field as opposed to an electric field. Fine magnetic particles are suspended in the fluid. They have been shown to be more limiting than electrorheological fluids as the system which provides adequate magnetic fields are heavy and bulky when compared to the structure itself.

- A bimetallic strip consists of two dissimilar metals bonded to each other, which have dissimilar coefficients of thermal expansion. Upon an increase of temperature, the structure bends to compensate for the varying deflection of the layers. Advantages of this method of actuation are that fabrication is limited to material deposition, large forces can be developed and the design is simple. However, proper heat sinks must be developed and large amounts of power are consumed. The forces are adequate for rotation of the ocular prosthesis; however, the displacements and response time (1 Hz) are insufficient for the requirements necessary to mimic eye movements.

- Large actuation strains can be evolved from polymers having a low stiffness and high dielectric constant resulting from the application of an electrostatic field. Electroactive polymers (EAP) are composed of a perfluorinated ion exchange membrane with platinum electrodes deposited on either side. The

films are required to remain moist at all times to operate, since a balance is required between the elastic forces of the polymer and the water's affinity to the ion-exchange sites. If a voltage of at least 2V is applied to the film, the film will bend towards the anode due to the Coulombic forces. Increasing the voltage level increases the bending displacement. Displacements up to 1 inch were observed with alternating voltage frequencies of 0.1 to 0.01 Hz, which relates to a displacement of over 10% (Bar-Cohen et al, 1997). However, only longitudinal extensions evolve, not contractions. A four fingered gripper was developed to lift a 10 gram mass. EAP materials are light, low cost, easily formed and are produced similar to traditional polymers. The reaction speed occurs within microseconds to seconds, with a drive voltage of 4 to 7 V and power consumption in the order of milliwatts.

Liu, Bar-Cohen and Leary (1999) produced a silicone film which produced an extension of 12% in the longitudinal direction when 2500 V was applied.

Electroactive polymers appear to behave within the constraints imposed by the ocular eye challenge in terms of displacement, however the electric field required to actuate EAP is between 50 and 169 V/μm. This translates to an unusually large potential in a small area. To obtain several percent of actuation strain, which would be required to rotate the eye, voltages between 1 and 2.5 KV are necessary. In addition, the EAP will result in large displacements only at frequencies in the order of 0.1 Hz. This is insufficient for the required magnitude of the displacement for the ocular prosthesis. EAP's do not act to mimic muscles in that they only actuate in expansion, not contraction. The fact that EAP must stay moist to operate poses a severe design problem.

- Shape memory alloys (SMA) are a class of solid actuators, in which a phase transformation occurs at a specific temperature where the change in volume is orders of magnitude larger than those experienced by thermal expansion. This

change in shape is up to 8% in the axial direction for NiTi (nickel titanium). As the SMA is heated, a phase transformation occurs which results in a contraction of the material. The forces exerted due to this contraction are large, and are dependent on the size of the specimen. For example, a 100 μm wire can lift 150 g, whereas a 375 μm wire can lift 2000 g. Upon cooling, the phase transformation is reversed and the SMA returns to its original extended length. In typical applications, the phase transformation is obtained by heat produced from electrical resistance and 99% of the energy goes to heat production, thus resulting in a very low efficiency. The cyclic actuation frequency at which these transformations can occur is limited by heat dissipation; however, selecting smaller diameter wires will increase the actuation frequency up to 1 Hz. Shape memory alloys are non-linear materials in that the temperatures for shape change upon heating are different than cooling. This presents difficulty when attempting to use the actuator in position control. One of the greatest benefits of shape memory alloys is that they have the largest energy density per volume compared with other actuation methods. Shape memory alloys do have the ability to function in an actuating environment; but, design problems such as response time and fatigue life need to be overcome.

Shape memory alloys can mimic the behaviour of a contracting muscle: as when the temperature of the SMA changes, the wire contracts or expands. They are simple, in that the component consists of a wire and a current source. NiTi has a high resistivity of approximately 80 μΩ/cm, such that currents of up to 2A can be used for electrical resistive heating. This type of heating results in fast changes in temperature of the SMA element, thus allowing SMAs to be viable actuation systems.

As SMAs allow for up to an 8% contraction in the axial direction, they are suitable for the desired magnitude of ocular prosthesis rotation, especially if the SMA is formed into a spring. Recovery forces of up to 5 N for 100μm

diameter wire have been reported (Mondo-tronics, Inc., San Rafael, CA, USA). Control of the nonlinear material and a low response time may pose boundaries for operation of an actuator composed of SMA for the orbital prosthesis.

SMA actuators have been developed since 1986, as described in the review by Reynaerts and van Brussel (1998), with the first design as a sigma shaped pulley system. Further work considered the hysteresis and possible linearization using two counteracting shape memory elements. Position feedback using electrical resistance was attempted. Actuator frequencies of 1 Hz were reported with a series of SMA-based antagonistic actuators. SMA's have been incorporated into micro robots and mechanisms (such as brakes, oscillators, valves, robot arm joints, and mollusk type grippers (Homma, Miwa and Iguchi, 1990)), due to their high power to weight ratio.

- Grant and Hayward (1995) initially developed an SMA actuator consisting of thin NiTi wires woven in a helical pattern around discs. This application was to control the movement of a camera in a robot. Since then, Grant and Hayward (1997, 2000) have focused their research on variable structure control design of non-linear SMA.

- A biomimetic underwater robot has been developed by Witting, Ayers and Safak (2000), which is based on the movement of a lobster. Antagonistically acting artificial muscle pairs were used to produce motion around each leg joint. The movement was controlled using pulse width modulation with a pulse frequency of 100 Hz, delivered at 7 V and a 70% duty cycle.

- The Nano-Muscle® (NanoMuscle, Inc., Antioch, CA, USA) utilizes shape memory alloys to obtain linear actuation. A schematic of the layered sliding design is shown in Figure 2.3. The technology involves a number

of 50 μm SMA wires, which cause the plates to contract by controlling the amount of current applied. The stroke available is 4 mm, with forces ranging from 0.3 N to 0.7 N. The recommended voltages for the Nano-Muscle® are 2 to 4 V at 160 mA to 350 mA of applied current. The ranging power requirements are due to the choice of high speed or high efficiency units. The power levels and displacements are adequate for the orbital prosthesis. The response time of the Nano-Muscle® is 165 ms for contraction and up to 625 ms for extension. Although this technology may be appropriate for the project, the full dimension of the actuator at 56.53 mm is beyond the limits of the depth of the orbit.

2.4 Actuator Selection

The method of actuation that appeared to best fit the design constraints and the design philosophy are so-called smart materials, in particular, shape memory alloys (SMAs). The word *smart* alludes to being clever, however, it is more accurate to say that it is a word for the ability to respond to changing environments in a useful way. Bandyopadhyay (1999) defines smart structures as "as system or structure which has attached or embedded sensor, actuator and control mechanism such that it has capability of sensing external stimuli and responding to them in an appropriate fashion". The actuator for the orbital prosthesis should incorporate an element of smart technology, as the general biological operation of the eye fits within Bandyopadhyay's definition.

Tabib-Azar (1998) compiled the energy density for various actuators, and the results are summarized in Table 2.1. Shape memory alloys provide the highest energy density of the actuators discussed.

Actuator Type	Energy Density (J/m^3)
Gas bubble	3.4×10^2
Muscle	1.8×10^4
Piezoelectric	1.2×10^5
Electrostatic	1.8×10^5
Electromagnetic	4.0×10^5
Bimetallic	5.0×10^5
Thermopneumatic	1.2×10^6
Shape memory alloy	6.0×10^6

Table 2.1: Comparison of Energy Density for various Actuators (Tabib-Azar)

Detailed information regarding these novel materials follows in the next section, along with additional constraints imposed by the nature of SMAs.

2.5 *Background on Shape Memory Alloys*

Shape memory alloys (SMA) have the unique property that a change in shape of up to 8% in the axial direction occurs with a change in temperature or applied stress. In addition, the shape change is reversible and repeatable. Recovery stresses of up to 600 MPa have been reported. There are a variety of materials which possess the shape memory ability such as AgCd, CuZn and NiTi. The most widely used SMA is NiTi, due to its superior mechanical properties such as a modulus of elasticity of 80 GPa and a yield strength of 690 MPa - for austenite phase only.

2.5.1 Metallurgy

The change in shape occurs due to a phase transformation of the crystal structure. The low temperature phase is called martensite and the high temperature phase is called austenite. The thermal cycle of SMA with respect to their crystal structure is shown in Figure 2.4. If the SMA is initially austenitic, the atoms in the crystal

are aligned at the corners of a square. As the metal cools, the martensite begins to form. The crystal structure of martensite is similar to a parallelogram, with the atoms on the corners. However, if all the crystals shifted from a square to a parallelogram, a net change in shape would occur and as such, this configuration is not energetically preferred. To overcome this, the crystals will 'twin', that is, the boundary between two crystals will act as a mirror. The observed shape change when the material is loaded at the lower temperature occurs by deforming the SMA which acts to remove the twin boundaries. As the SMA is heated, the crystal will change back to its austenitic form.

The phase transformation occurs within specific transformation temperatures. Shown in Figure 2.5, as the SMA is heated the change in length begins at the austenite start temperature (A_s) and ends at the austenite finish temperature (A_f). Likewise, the original length is regained by cooling the SMA so that it becomes fully martensitic. Martensite begins to form at the martensite start temperature (M_s) and the SMA is fully martensitic beyond the martensite finish temperature (M_f). As can be seen from the schematic in Figure 2.5, the process is hysteretic and highly non-linear.

Due to the change in crystal structure, the mechanical, thermal and electrical properties of austenite and martensite are not identical and as a result, the properties of SMA are often defined by the martensite volume fraction. The large variation in mechanical properties can be seen from stress-strain curves of SMA in the austenite and martensite phases, illustrated in Figure 2.6. The austenite phase has a higher Modulus of Elasticity than the martensite phase. The loading and unloading of SMA in the austenite phase follows the same path. However, a large amount of residual strain remains in the martensite phase after removal of the stress, due to the elimination of the twin boundaries.

2.5.2 Constitutive Models of Shape Memory Alloys

The strain behaviour of linear elastic materials is based solely on the elastic strain. With thermoelastic materials, such as shape memory alloys, three types of strains contribute to the total strain observed. These strains are the elastic strain, the thermal expansion strain due to a change in temperature, and the phase transformation strain. The phase transformation is described by the martensite fraction of the SMA.

Hence, the stress (σ) in SMAs depends on strain, ε, martensite fraction, ξ, and temperature, T, shown in 2.1 (Tanaka, 1986).

$$\sigma \equiv \sigma(\varepsilon, \xi, T) \tag{2.1}$$

$$d\sigma = \frac{\partial \sigma}{\partial \varepsilon} d\varepsilon + \frac{\partial \sigma}{\partial \xi} d\xi + \frac{\partial \sigma}{\partial T} dT \tag{2.2}$$

In this representation, the strain term is the combined strain of the elastic, thermal and phase transformation factors. By assuming that the partial derivatives in 2.2 are constant leads to a constitutive model as shown in 2.3 (Tanaka, 1986), where D is the modulus of elasticity, Ω is the phase transformation tensor, and θ the thermoelastic tensor, which can be found experimentally.

$$d\sigma = Dd\varepsilon + \Omega d\xi + \theta dT \tag{2.3}$$

For a general state, D, Ω, and θ are tensors. In a 1-D model, the tensors are reduced to their axial values.

There are several models to describe the martensitic fraction: Liang and Rogers (1990) evolved the cosine relationship, Cunfu *et al.* (2000) used a linear model and Tanaka (1986) chose an exponential relationship. For the martensite to

austenite transformation, the respective relationships are shown in 2.4, 2.5 and 2.6.

$$\xi = \frac{\xi_o}{2}\left\{\cos\left(a\left(T - A_f - \frac{\sigma}{C}\right)\right)+1\right\} \tag{2.4}$$

$$\xi = \frac{\xi_o}{A_f - A_s}\left(A_f - T + \frac{\sigma}{C}\right) \tag{2.5}$$

$$\xi = 1 - \exp\left[a\left(T - A_f - \frac{\sigma}{C}\right)\right] \tag{2.6}$$

These equations can model the martensitic fraction at any point during the phase transformation, as long as the initial martensite fraction, ξ_0, is known. The parameter a is a function of the transition temperatures and C is the slope of the linear portion of the σ-T curve, shown in Figure 2.7.

A statistical model often used in numerical analyses of the martensite fraction, (Amalraj, Bhattacharyya and Faulkner (2002)) is shown in 2.7, where P($\check{T}$, σ) is distributed normally.

$$\xi = 1 + \int_{M_s+\frac{\sigma}{C}}^{T} P(\check{T},\sigma)\, d\check{T} \tag{2.7}$$

The choice of model is dependent on the complexity of the problem to be solved.

The modulus of elasticity, D, in experimental testing, has been shown not to be constant for SMA, but a function of the martensitic fraction. Brinson (1993) suggested the rule of mixing of the high temperature modulus and the low temperature modulus, shown in 2.8.

$$D(\varepsilon,\xi,T) \equiv D(\xi) = D_A + \xi(D_M - D_A) \tag{2.8}$$

The subscript A refers to the austenite phase and M the martensite phase. Since the phase transformation property is a function of the modulus of elasticity, Ω will also be a function of martensitic fraction.

2.5.3 Processing for Design

To create the shape memory effect for a particular application, the desired shape must be set using thermomechanical processes. This is accomplished by deforming and constraining the SMA element, and applying an appropriate heat treatment.

Heat treatment parameters must be adequate such that the shape is set and the properties are sufficient for the application. These parameters, which are usually determined experimentally, are the temperature and duration of the furnace anneal. Mihálcz (2001) suggested that rapid cooling is preferred to using, for example, water quenching or forced air cooling.

SMA, Inc. suggests a temperature range of 400°C for 1-2 minutes to 500°C for 5 minutes, depending of the size of the SMA element. In the biomimetic shape memory alloy actuators for use in underwater ambulatory robots as developed by Witting, Ayers and Safak (2000), the anneal for the 250 μm diameter Flexinol® was 500°C for 30 minutes in an Argon atmosphere. The wire was etched with HNO_3 and HF to remove the surface oxide which resulted in more uniform electrical resistance and better electrical connections at the terminals. Waram (1993) suggested an anneal temperature of 400°C for a duration of 30 minutes.

While the fatigue life of SMA material has been reported to be limited, others have shown that it can survive over 1 million cycles (Clark, 1999). The lifetime of these materials is a direct function of the stress cycle, temperature cycle and previous heat treatment. Clark also reported that fatigue failure of SMA in

actuators does not occur from failure of the SMA element itself, but degradation in performance from creep. This creep is a result of permanent deformation from thermal cycling. To increase the life of the SMA actuator Clark suggested that the temperature the SMA is exposed to should be limited to less than 250°C and the strain limited to less than 4%. As the cyclic strain decreases, the number of cycles before failure increases.

2.6 Design constraints of Shape Memory Alloys

The limitations of the actuator due to the use of SMA material that were established in the design of the present study were:

- A maximum shear strain cycle of 1.5% to 2% to minimize fatigue failure of the metal;
- The duration of the full contraction of the SMA to be less than 1 s so that an actuation frequency of around 1 Hz could be obtained;
- A transition temperature range greater than body temperature and less than 100°C. This is to allow the full phase transformation to occur while limiting the temperature to preserve the silicone prosthesis.

2.7 Development of Design

The initial conceptual design sought to replicate the function of the extraocular muscles. Using the biomimetic approach, motion is produced around a joint by antagonistically acting muscle pairs. By attaching SMA wires to the ocular element of the prosthesis in the same manner that muscles are inserted into the eye, a system of agonist and antagonist pairs would be able to pull the eye from side to side. The forces of the SMA wire are very small in the relaxation phase compared to the activation phase. Consequently, this dual system would only use the activation phase.

As proof, a single wire on the side of the eye does not provide the deflection required for a 30° rotation of the eye. The SMA can contract a maximum of 8% of its axial length. If the wire were 20 mm in length (maximum size available for the anterior-posterior dimension of the orbital prosthesis components), the resulting stroke would be less than 2 mm. If the ocular globe were considered a sphere of radius 10 mm, a 2 mm stroke on the surface would yield a rotation around the centroid of approximately 9°, shown in Figure 2.8, and this would not fulfill the design criterion of ±30° of rotation.

If a spring of SMA is considered, the deflection obtained is significantly increased, since the effective length is increased. This increase in deflection comes at a cost of a reduction in force during activation. Since the forces required to rotate the eye would be small, the advantage of greater deflection offered a good compromise.

Combinations of SMA springs in parallel and series with a biasing steel spring were considered. This bias spring would decrease the time to reset the SMA spring to the neutral position by adding a force to cause it to return to the neutral state, and prepare for the next cycle. However, the actuation force of the spring would have to be greater than the resistive force of the bias spring. Since there is a dual system, the force of the SMA spring would also have to compensate for the resistive forces due to the opposite spring. As the initial idea developed, the designs became more complicated by increasing the number of springs, introducing torsional springs, and gear and pulley systems. This meant that the general philosophy of the project, simplicity, was not being adhered to, and a new concept had to evolve.

2.8 Final Design

The complete design of the actuator and the supporting components are shown in Figure 2.9. The springs would originate at the main post and prosthetic wall, and connect to the V-brace. A central cup and cone bearing provided a low friction, secure joint for the rotary action between the V-brace and the main post. The SMA springs would be attached to the V-brace at a position where the stroke and force would result in a desired ocular rotation. Electrical connections would be at the main post and the V-brace. For the ocular element to rotate to the right, the SMA spring on the right would be activated electrically. The left SMA spring would be activated for a rotation to the left side. The springs would only be activated one at a time, never simultaneously. A pair of bias springs act to both allow the ocular motion from side to side, as well as to maintain the neutral position when the eyes are in the forward motion.

As the ocular element in the prosthesis was not a solid sphere, the effective 'muscle length' could be increased by utilizing the space inside the eye to amplify the stroke of the SMA spring. To utilize the space on the inside of the ocular element, a V-shaped bar would be attached to the inner surface of the ocular element and held to a main post at a pivot point. The main post would be attached to the back of the prosthesis, thus integrating the actuation structure to the prosthesis. The design of the prosthesis would not have the ocular element resting on the eyelid surfaces, thereby eliminating frictional forces between the ocular element and the silicone prosthesis. This is accomplished by the ocular element being secured to the V-shaped bar and the main post. The ocular element can be recessed from the silicone eyelids by less than a millimetre such that there is no contact between the ocular element and the silicone body of the prosthesis. A transparent plastic hemisphere is to be integrated into the silicone eyelids to act in enclosing the ocular element, actuator and electronics from the environment.

Two SMA springs are to be used in an agonist-antagonist pair to pull the eye from side to side.

Sufficient torque at the joints is required such that the ocular element will move. Another concept of biomimicry is the attachment of the muscle to the structure considering the higher load and moderate strains surrounding a joint.

The remainder of this thesis will focus on a variety of parameters which will help answer the question: Can shape memory alloys act as an actuator to mimic the behaviour of the extraocular muscles? This is addressed in the content of the design previously outlined. To provide that information, several factors must be focussed on, including:

- the forces required for rotation of the eye by SMA and the bias spring;
- the current required to activate the SMA springs;
- the heat transfer of the wire to the surroundings to predict the relaxation time which is dependent of the diameter of the wire;
- the position of the wire to obtain maximum stoke and hence, ocular rotation;
- the geometric variables in the spring to obtain the required force and deflection (wire diameter, coil diameter and number of active turns);
- an exploration of methods to control the SMA.

A prototype model to actively test the operation of the SMA actuators with respect to activation force and response time was developed. The prototype model that was constructed was five times the size of the actual prosthesis. The relevant dimensions required for the modelling are that the radius of the prototype ocular is 50 mm and that the full length of the prosthesis is 100 mm. Only the horizontal movement of the ocular element was investigated in the prototype design.

Figure 2.1: A mold of a typical exenterated orbit. The depth of the orbit is 40 mm and the width is 30 mm.

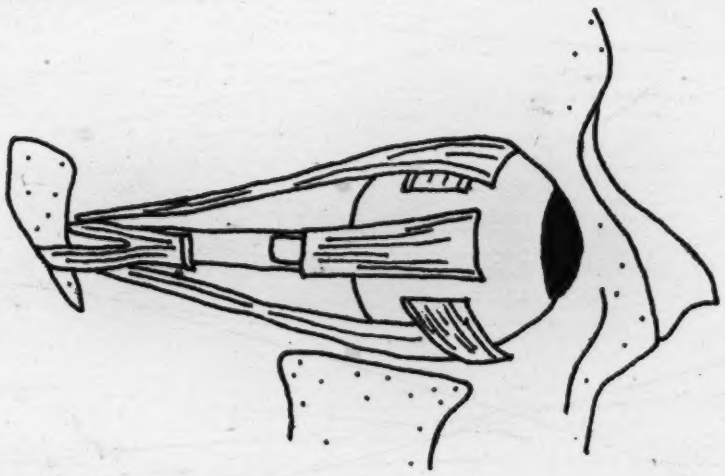

Figure 2.2: Schematic of the anatomy of the eye showing the extraocular muscles, adapted from Gray's Anatomy (1918)

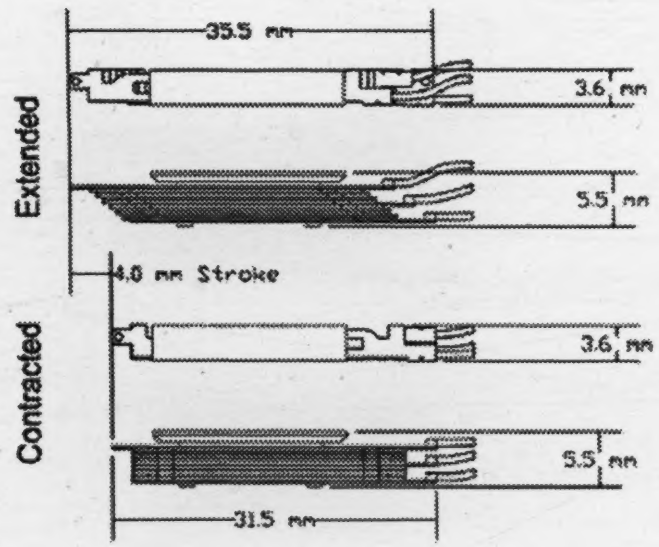

Figure 2.3: Schematic of the NanoMuscle®

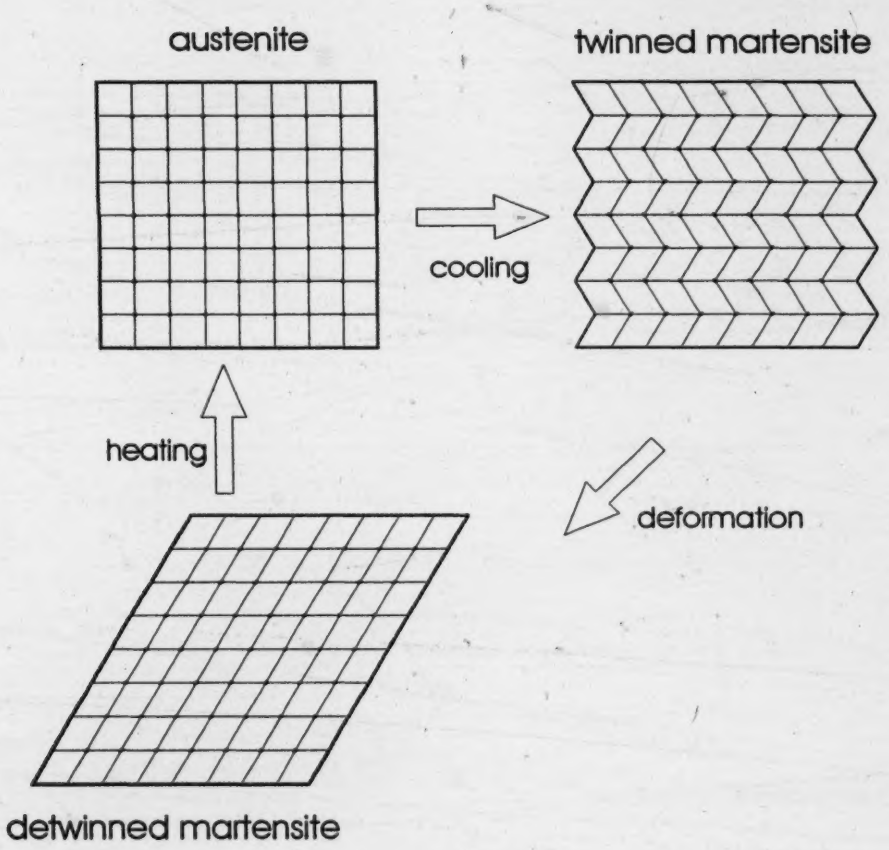

Figure 2.4: Thermal cycle of SMA with respect to crystal type

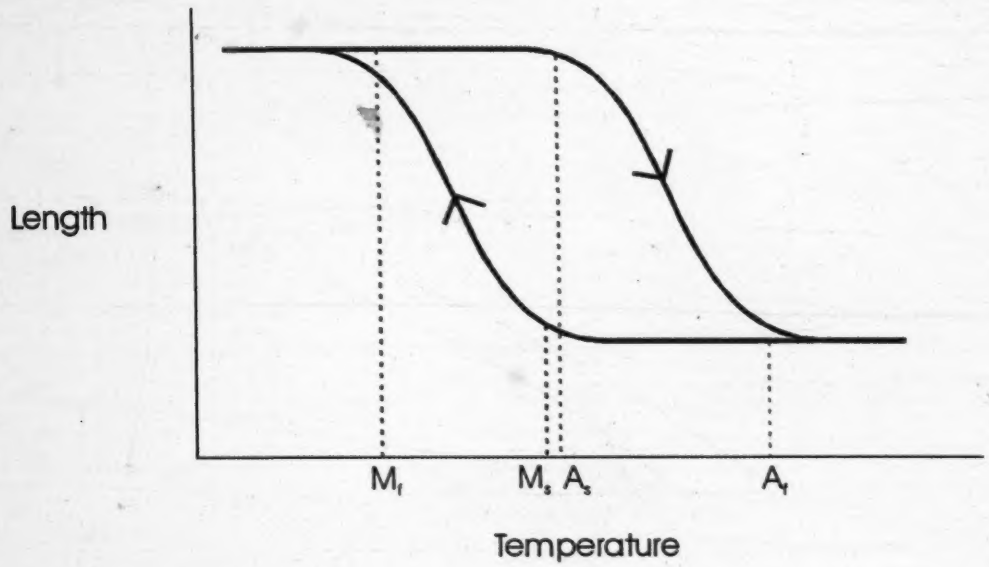

Figure 2.5: Location of transformation temperatures of SMA

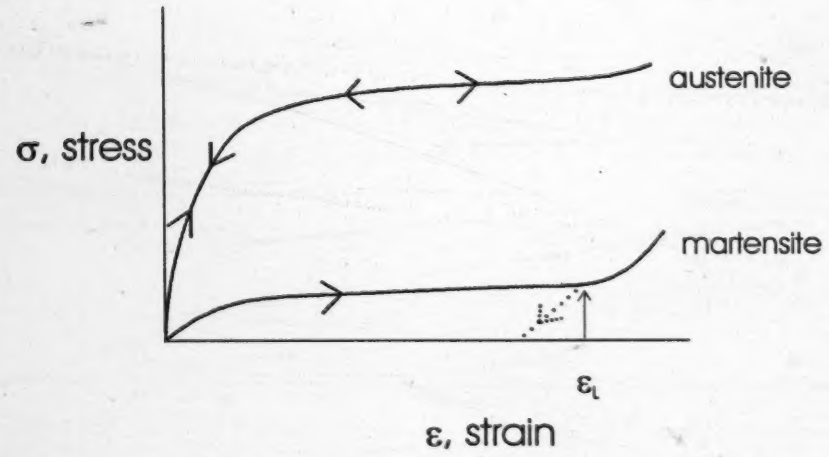

Figure 2.6: Stress-strain behaviour of austenite and martensite, with loading and unloading paths ensuring the strain was within the elastic region of the SMA

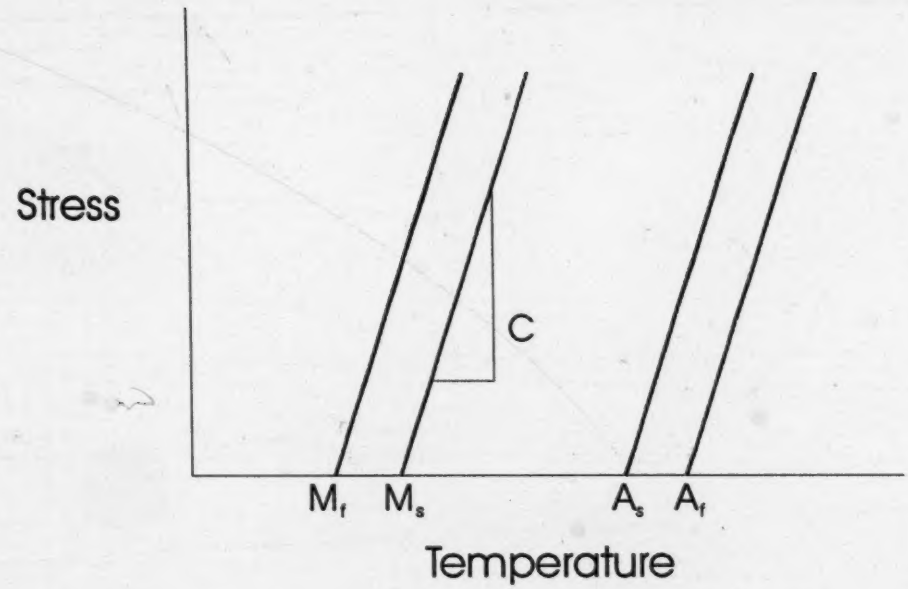

Figure 2.7: General relationship between stress and temperature of SMA, showing that the transformation temperatures increase linearly with increasing stress

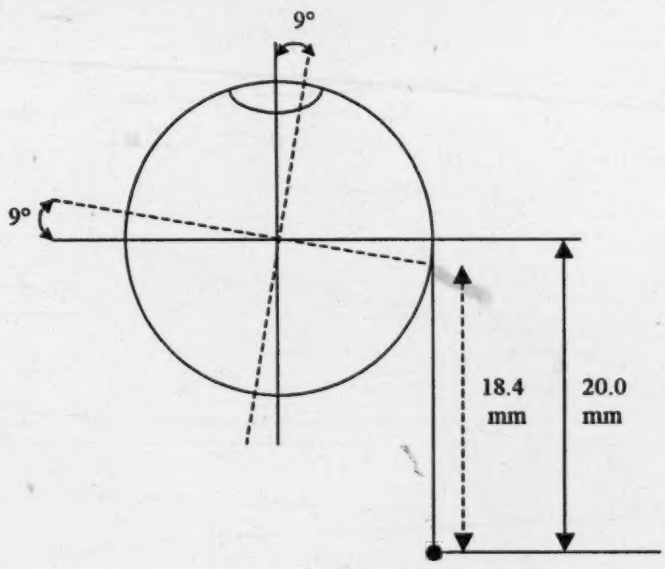

Figure 2.8: Schematic of maximum possible rotation using only SMA wire attached to the surface of the ocular element

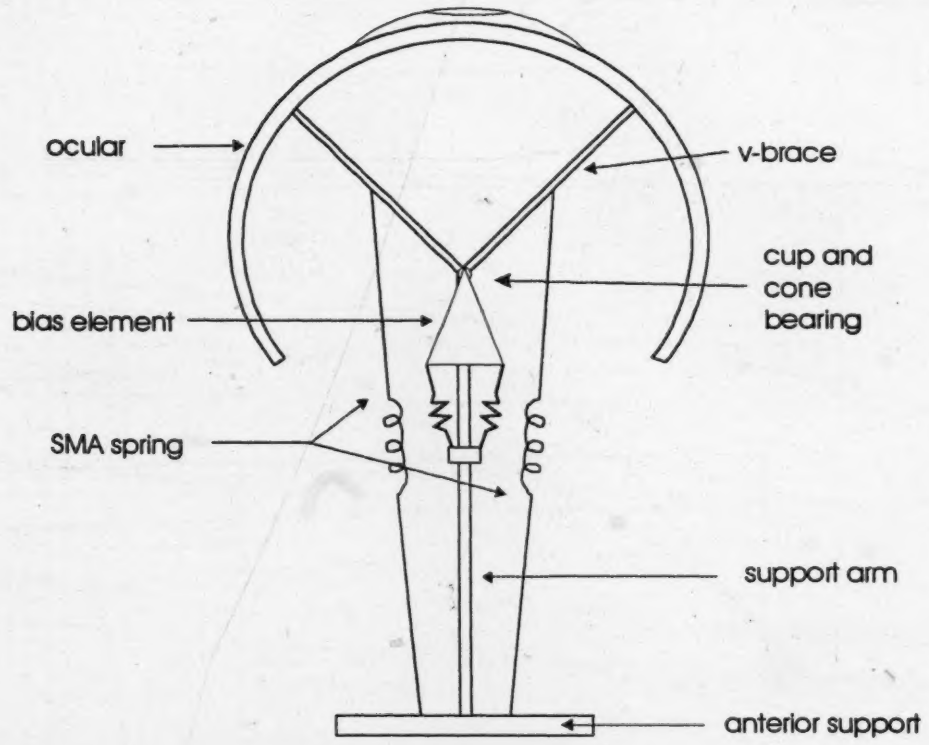

Figure 2.9: Schematic of the SMA actuated orbital eye prosthesis

3 Analysis of Proposed Design

In this chapter, the feasibility of the proposed design is evaluated considering the criteria outlined in the previous section. To accomplish this requires determination of the actuation force required by the SMA spring, as it will dictate the magnitude of the rotation of the eye. The SMA spring force is directly related to the moment of the return bias element. An evaluation of the moment of the return bias element is conducted to ensure that the moment of the bias element does not exceed the force produced by the SMA spring and that the neutral position is maintained.

To predict response time of the actuator, an electro-thermal analysis is conducted.

3.1 Force Model of the Design

The force produced by the SMA spring upon actuation is dependent on the bias spring moment, the opposing SMA spring and the geometry of the design. The geometry of the design is shown in Figure 3.1 in the neutral state, and in Figure 3.2 in the active state. The length of the support arm is l, the position of the attachment point from the centre bearing is x, the initial length of the SMA wire in the neutral position is $l_{SMAintial}$, and the active length of the actuator is denoted as $l_{SMAactive}$. In a general state, the angle between the support post and the V-support is $\pi/2 + \theta$, the angle between the V-support and the SMA spring is denoted as α for the active arm and β for the opposing arm. The angle of rotation of the eye about the neutral state is represented as Φ.

The cosine law allows for an expression of the length of the spring before actuation in 3.1, while when the eye is actuated by a rotation of Φ from the neutral position, the length of the spring changes to 3.2.

$$l^2_{SMAinitial} = l^2 + x^2 - 2lx\sin\theta \qquad (3.1)$$

$$l^2_{SMAactive} = l^2 + x^2 - 2lx\sin(\theta - \Phi) \qquad (3.2)$$

The actuator consists of a pair of agonist-antagonist SMA springs. As the active spring contracts, the opposing resting spring will extend. The length of the opposing spring, l_{SMAopp}, is shown in 3.3.

$$l^2_{SMAopp} = l^2 + x^2 - 2lx\sin(\theta + \Phi) \qquad (3.3)$$

A detailed free body diagram of the V-support is shown in Figure 3.3. The force produced by the SMA is F_{SMA}, the moment produced by the bias spring is M_{spring}

and the force of the opposing SMA spring is F_{SMAopp} respectively. The sum of the moments around the bearing joint is shown in 3.4.

$$\Sigma M_{+} = F_{SMA} x \sin\alpha - M_{spring} - F_{SMAopp} x \sin\beta = 0 \qquad (3.4)$$

The moment of the SMA springs is calculated as the product of the force of the SMA spring and the perpendicular distance to the attachment point. As the design is symmetrical about the pivot, the attachment point for both the active SMA spring and the opposing SMA spring are identical.

To determine the forces shown in the moment balance from 3.4, the angles between the springs and the V-support must be calculated. These angles change with the ocular rotation. The sine law allows for a relationship of the two angles, α for the active side, and β for the opposing side, shown in 3.5 and 3.6.

$$\sin\alpha = \frac{l}{l_{SMAactive}} \sin(\theta - \Phi) \qquad (3.5)$$

$$\sin\beta = \frac{l}{l_{SMAopp}} \cos(\theta + \Phi) \qquad (3.6)$$

Substituting 3.5 and 3.6 into 3.4, results in 3.7; an expression for the force of the active SMA spring.

$$F_{SMA} = F_{SMAopp} \frac{l_{SMAactive}}{l_{SMAopp}} \frac{\cos(\theta + \Phi)}{\cos(\theta - \Phi)} + M_{spring} \frac{l_{SMAactive}}{xl} \frac{1}{\cos(\theta - \Phi)} \qquad (3.7)$$

The values which are unknown at this point are F_{SMAopp} and M_{spring}. The opposing spring is assumed to be in the martensite state, as well as deformed beyond the elastic limit. According to the stress-strain diagram of martensitic shape memory alloy, shown in Figure 2.6, the stress is essentially constant after the elastic yield.

Hence, the force of the opposing SMA spring can be expressed as a constant since the actuation cycle will not exceed the elastic limit, ε_L. The moment of the bias spring is determined in the following section.

3.1.1 Moment Return Requirements

The bias balance spring is included to assist in bringing the prosthetic eye to neutral when no motion is detected from the working eye. This moment will resist the actuating spring, but will also act to assist the antagonist spring in returning from actuation to relaxation. The moment created by the balance spring is denoted as M_{spring} and is necessary in determining the force requirements for designing the SMA actuator.

While initially a torsional spring was considered, the problem of having this spring operate through its unloaded state makes it difficult to maintain a stable neutral position. This moment would not be sufficient to extend the opposing martensitic phase of the SMA spring back to relaxation and its original state and make it difficult to have a stable neutral ocular position.

To overcome this problem, two cantilever beams, initially displaced around an ellipse, were to provide the moment required, as shown in Figure 3.4. Using beam theory, the force due to each of the cantilever beams was calculated. At the contact point between the ellipse and the beam spring, the force of the cantilever beam, W, is given by 3.8 as a function of the contact point between the beam and ellipse, l, the displacement of the beam, v, and the modulus of elasticity, E, and the moment of inertia, I, of the beam.

$$W = \frac{3vEI}{l^3} \tag{3.8}$$

A schematic of the system in action is shown in Figure 3.5.

To calculate the deflection of the cantilever beams, the equation for an ellipse with major and minor axes (a and b) was transformed around the centre through rotation by an angle Φ. The ellipse is attached to the pivot point such that the rotation of the ellipse is the same as the rotation of the ocular. The deflection of the beam is the difference between the maximum horizontal position of the ellipse and the initial displacement of the beam. The length to contact was determined as the difference between the length of the cantilever beam from the beam origin site to the initial and final contact points on the ellipse.

The moment of the bias cantilever spring can be calculated from the product of the forces from both cantilevers, F_1 and F_2, and the distance from the origin to contact point, dy, shown in Figure 3.6.

As a function of the angle of rotation, Φ, the moment for a cantilever beam 0.5 mm in thickness is shown in Figure 3.7. This design provides only a small moment arm in the $\pm 10°$ region and makes the design inadequate.

A simpler concept for the bias element was to retain the cantilever beams, but to use a rectangular piece pinned near one end, as opposed to a complex ellipse pinned at the centre, as shown in Figure 3.8. This would act to constantly increase the moment length, thus increasing the stability of the design. Following the same design parameters and utilizing the same material properties as the previous moment calculation, the moment for the rectangular bias element is shown in Figure 3.9 with respect to the angle of rotation. The relationship still maintains the parabolic shape, with moments of near zero in the $\pm 5°$ region. The moment increases rapidly with this cam shape, however, modifying the thickness and width of the cantilever beam as well as decreasing the length of the rectangular element can decrease the moment. Again, the eye would not be stable at the neutral point.

A triangular element was studied such that the moment length was constant, shown in Figure 3.10. It was considered due to the constant moment length and the fact that a greater increase in slope of the element causes a greater increase in the force of the cantilever beams. In the schematic, d is the distance from the end of the triangle to the rotation centre, L is the distance from the rotation centre to the axis of contact with the cantilever beams and the length of the cantilever beams is denoted as Γ. As Φ increases, the relationship of the force due to the cantilever beams is shown in 3.9.

$$F = \frac{3EI\left[\left(d+\frac{L}{\cos\Phi}\right)\frac{\sin\alpha}{\cos(\Phi+\alpha)}+L\tan\Phi-(d+L)\tan\alpha\right]}{\Gamma^3} \qquad (3.9)$$

The moment of the cantilever beam is denoted in 3.10.

$$M_{spring} = FL \qquad (3.10)$$

The effect of d, L, α and Γ on the bias spring moment are shown in Figure 3.11, for the dimensions given in Table 3.1.

	d (mm)	L (mm)	α (°)	Γ (mm)
A	5	10	30	30
B	2.5	10	30	30
C	5	5	30	30
D	5	10	15	30
E	5	10	30	25

Table 3.1: Changes made to geometry of triangular cam bias element

As seen, the moment-Φ relationship has a distinct slope at the origin. Figure 3.12 shows the detail of $0°<\Phi<10°$. Moments up to 10 times that of the elliptical and rectangular shapes are possible and suggest this is a better design. However, an

investigation into the use of springs as opposed to cantilever beams, shown in Figure 3.13, was conducted for comparison.

It was hoped that the springs would provide a steeper slope of the moment-Φ curve. This would increase the stability of the ocular in the neutral position. Springs were attached between the support arm and the triangle cam, as shown in Figure 3.13. The moment of the system is now correlated to the spring constant, and the initial extension of the bias spring. If a spring, with unstretched length of 7 mm and spring constant of 0.012 N/mm, were attached between the support arm and triangle cam to a length of 18 mm, the moment-Φ relationship is shown in Figure 3.14. The moment changes quickly with the rotation, and begins to level off with increasing Φ. This is considered to be the more ideal for the moment spring designs.

3.1.2 Attachment Point and Stroke

The attachment point of the SMA spring to the mechanical support is shown in Figure 3.1, as the distance x from the pivot point. In equation 3.7, the attachment point needs to be determined to predict the required force of the SMA spring. The attachment point dictates the length of the SMA spring actuator, as well as contributes to the moment of the SMA spring which opposes the moment of the bias spring element.

The length of the SMA spring was determined in both the initial and active positions for angles of rotation up to 30° and for attachment points between 5 mm and 50 mm. The required stroke is the difference between the initial and active lengths. As indicated in Figure 3.15, the relationship between the stroke and attachment point is the difference between $l_{SMAinitial}$ and $l_{SMAactive}$, as calculated from 3.1 and 3.2.

The stroke is limited by the strain in the SMA and the geometry of the mechanical support system of the prosthesis. A linear relationship between the stroke and strain of a spring with respect to the geometrical properties is shown in 3.11 (Waram, 1993).

$$Stroke = \frac{\pi D^2 n \Delta\gamma}{d} \tag{3.11}$$

The stroke is a function of the change in strain, $\Delta\gamma$, and the geometrical parameters of the spring. These parameters are the coil diameter, D, the wire diameter, d, and the number of active coils, n. If the constraint is the maximum amount of strain permitted in the SMA spring, the appropriate stroke values will dictate the attachment point of the SMA spring on the V-support, based on Figure 3.16. As the attachment point increases away from the pivot point, more stroke is required to rotate the eye.

As a function of the attachment point, the shear strain is shown in Figure 3.17, for angles of rotation of 10°, 20° and 30°. The coil dimensions used for this figure were a wire diameter of 250 μm, a coil diameter of 2.38 mm and 10 active turns. To reduce failure by fatigue, it was necessary that the maximum shear strain cycle not exceed 2%. For a maximum eye rotation of 30°, and a shear strain between 1.5% and 2% from Figure 3.17, the attachment point on the prototype model should be approximately 30 mm.

3.1.3 Moment of Inertia of Rotary Components

The moment of inertia of the components will play a role in the acceleration of the ocular element as well as the amount of friction produced on the pivot bearings. In this assessment, the friction of the pivot has been assumed to be negligible. However, as the mass of the ocular element and V-support increase,

their inertia may be important to consider. In the following, the inertia of the components has been neglected.

3.1.4 SMA Force Requirements

From equation 3.7, the forces required by the SMA for static equilibrium can be determined. With a SMA spring with 10 active turns, a wire diameter of 250 μm and a coil diameter of 2.38 mm, the minimum force required in terms of rotation of the ocular element is shown in Figure 3.18 for various attachment points. At an attachment point of 30 mm, the minimum force required to be generated by the SMA spring is 0.5 N.

3.2 Heat Transfer Between the SMA Spring and Surroundings

For the SMA actuator to produce a complete cycle, the activation and contraction temperatures must be achieved. The activation, or contraction, of the SMA spring commences when the temperature of the wire exceeds the austenite start temperature (A_s) and full contraction is obtained at the austenite finish temperature (A_f). This increase in temperature is delivered by resistive heating from a current source.

The time for actuation can be estimated by an energy balance between the energy generated by the resistive current flow and the energy both lost by convection to the surroundings and stored in the SMA, shown in 3.12, and is based on the work of Liang and Rogers (1992).

$$\dot{E}_{stored} = \dot{E}_{generation} - \dot{E}_{convection}$$
$$\frac{d}{dt}(\rho VcT) = I^2RL - hA(T - T_\infty) \qquad (3.12)$$

The generation of energy is a function of the current input, I, the resistance of the SMA, R, and the length of the SMA wire, L. The energy stored in the SMA is a function of the time dependent temperature of the SMA, the density of the SMA, ρ, the specific heat of the SMA, c, and the volume of the spring, V. The convective energy is a function of the heat convection coefficient, h, the surface area of the spring, A, and the difference in the temperature of the wire, T, and the surroundings, T_∞. This energy balance can be integrated to obtain the temperature response of the SMA spring 3.13.

$$T = \frac{I^2RL}{hA} + T_\infty - \frac{\exp(\frac{-hA}{\rho Vc}t)(I^2RL + hAT_\infty - T_o hA)}{hA} \qquad (3.13)$$

For the SMA spring to reset, the wire should be fully martensitic in order that a full contraction will occur on subsequent heating. This requires that the SMA spring cool beyond the martensite finish temperature (M_f). The cooling cycle of the actuator is slower than the heating cycle, as the driving force is that of convection alone.

As one of the COMPRU design requirements was that the ocular element not lag behind the real eye, the actuator must relax in less than 1 s. The actuator relaxation is due to convective still air heat transfer from the wire to the surroundings which is governed by geometry, the temperature difference between the wire and the surroundings, and the convection medium. It has been assumed that the convection medium is still air at a temperature of 32°C, slightly below normal human body temperature.

To determine the cooling behaviour of the SMA spring, the energy balance between the stored energy within the SMA and the surrounding convection medium reduces to 3.14.

$$\dot{E}_{stored} = \dot{E}_{convection}$$
$$\frac{d}{dt}(\rho V c T) = hA(T - T_\infty) \qquad (3.14)$$

Solving the energy balance for temperature with the initial condition that the temperature at start of cooling is T_o, results in 3.15.

$$T = (T_o - T_\infty)\exp(\frac{-hA}{\rho c V}t) + T_o \qquad (3.15)$$

This model requires a term for the heat transfer coefficient that is usually measured experimentally. However, Incropera (1996) has reported that air has a natural convection coefficient between 5 and 35 W/m^2.

It was determined (see Appendix A) that due to the differences in the diameters of the prototype wire and the actual wire, 250μm and 100μm respectively, that the heat transfer coefficients would differ significantly. For a 100 μm wire in free convection, as would be the case of the actual design, the heat transfer coefficient was estimated to be 125 W/m^2. For similar cooling behaviour due to convection of the 250 μm wire for the prototype design, forced air at a temperature of 32°C and velocity of 1 m/s was required. The detailed calculations of the heat transfer coefficient can be found in Appendix A. The heat transfer coefficient for the prototype model was calculated to be 240 W/m^2. Hence, further time dependent experiments were conducted with the use of a fan.

The transformation temperatures of the shape memory alloy will be an important factor to consider in the heat transfer problem, to ensure that the SMA spring

reaches the martensite finish temperature. The higher the temperatures for actuation, the greater the temperature difference between the spring and the surroundings, thus the heat flux will increase and the relaxation time will decrease. However, there is a limit to the increase in transformation temperature as more power would be required to heat the SMA. It may be speculated that temperatures that are too high may produce adverse reactions to the prosthesis or patient.

The heating profile of the SMA wires according to equation 3.13 is shown in Figure 3.19 with heat transfer coefficients in still air for both 100 μm wire and 250 μm wire. A steady-state temperature is achieved within 1 s of heating with currents between 0.1 and 0.4 A. If the austenite finish temperature is approximately 80°C, the current required is greater than 0.3 A and less than 0.4 A. The currents required for actuation decrease and the actuation times decrease for wires of decreasing diameter. Hence, an austenite finish temperature of approximately 80°C is desired.

Shown in Figure 3.20, is the cooling prediction time curve of the 100 μm wire and the 250 μm wire with the forced convection. This curve shows that the modification of the heat transfer coefficient was adequate in showing that the cooling behaviour is similar. This figure also contains information regarding the transformation temperature of the SMA wire. If the wire were at an initial temperature of 75°C, the actuator would reset in 0.1 s with a martensite finish (M_f) temperature of 40°C. If the M_f temperature is above 45°C, the time to reset should be sufficient for a 100 μm wire spring.

3.3 Spring Design

There are two methods which have been used for prediction of the actuation forces of shape memory alloys. The first use linear elastic models, but SMA's are

not linear elastic materials. The latter incorporate the constitutive SMA models into the spring theory.

Traditional alloys have a constant linear force-displacement relationship due to the fact that they operate solely in the linear elastic region of the stress-strain curve of the metal. The force-deflection behaviour of springs constructed of a linear elastic material is shown in below in 3.16 where P is the force, k is the spring constant, and δ the displacement (Shigley, 1989).

$$P = k\delta$$
$$k = \frac{d^4 G}{8D^3 n} \qquad (3.16)$$

The spring constant is a function of the wire diameter, d, the shear modulus, G, the coil diameter, D, and the number of active turns, n.

For these materials, the relationship between shear stress and shear strain is linear, shown in 3.17, with the shear modulus, G, as the proportionality constant.

$$\tau = G\gamma \qquad (3.17)$$

Shape memory alloys have a linear elastic region and a non-linear region due to the transformation that occurs between the austenitic and martensitic phases. At the point where the phase transformation occurs, the force becomes non linear, hence, k is no longer a constant. From 3.16, if k is not a constant, then it follows that since the geometric properties of the spring do not change, that the shear modulus changes during the transformation. This change in shear modulus is due to the atomic rearrangement between the austenite and martensite phases. In the actuator cycle, the change in force is a function of this change in shear modulus.

Stevens (1998) and Waram (1993) have investigated modelling SMA springs using linear spring theory, and limit their discussions to the linear elastic region. This hinders optimal use of the phase transformation effect in actuator design. Since no accurate model exists to describe the forces produced by SMAs, experimental testing is the only means to obtain this information.

Liang and Rogers (1993) have attempted to develop a spring model based on the constitutive SMA models. SMAs are dependent on the martensite fraction and temperature, as discussed in 2.5.2. The general form of the relationship between force, displacement, and temperature is shown in 3.18, where F is the force, y is the displacement, and the subscript e denotes the value at the elastic limit.

$$\frac{F}{F_e} = \frac{y}{y_e} + \frac{\Omega}{\sigma_e}(\xi - \xi_o) + \frac{\theta}{\sigma_e}(T - T_o) \qquad (3.18)$$

This model is considerably more complicated, due to the thermal and phase transformation coefficients. These values must be known for this model to be used predictably and require extensive testing to obtain accurate results.

The force and displacement of the actuator cycle can be shown graphically according to the constitutive models described earlier. The spring will initially be stretched in its martensitic phase, and heated to the austenite finish temperature. The final stress and strain in the spring will be zero, as heating the alloy recovers the initial stresses imposed. The full cycle is illustrated in Figure 3.21. From point 1 to point 2, the phase is fully martensitic and the spring is stretched an amount denoted by γ_o and τ_o. The temperature will increase from T_o to A_s, just to the point before the phase change begins. Between points 2 and 3, the phase change begins to occur, as the temperature and stress increase to A_f and τ_3 respectively. From point 3 to point 4, the fully austenitic spring recovers elastically at constant temperature. The temperature will decrease to T_o, and the cycle is repeated.

The force-displacement results obtained experimentally can be combined to yield a shear stress-shear strain relationship 3.19, derived from hot torsion testing by Dieter (1961).

$$\tau = \frac{2D}{\pi d^3}\left(\delta\frac{\Delta P}{\Delta\delta} + 3P\right)$$
$$\gamma = \frac{d\delta}{\pi D^2 n} \qquad (3.19)$$

This relationship will be the basis of the experimental determination of material properties. These material properties will be used in an algorithm to predict the force produced by the SMA actuation. The relationship between force, P, and displacement, δ, in 3.19 allows it to be applied to non-linear materials.

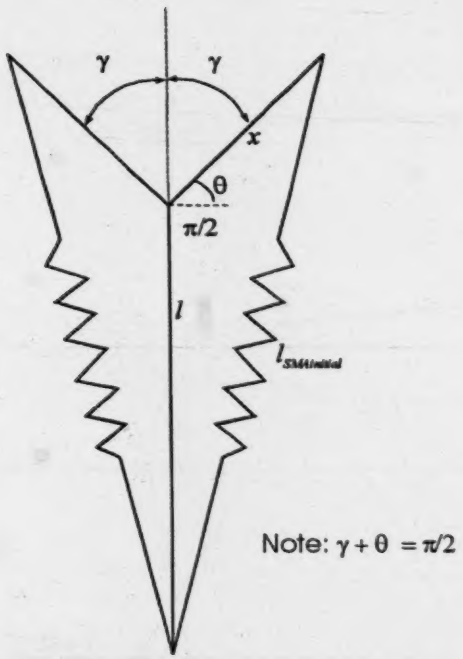

Figure 3.1: Length of initial SMA spring and schematic of angles used

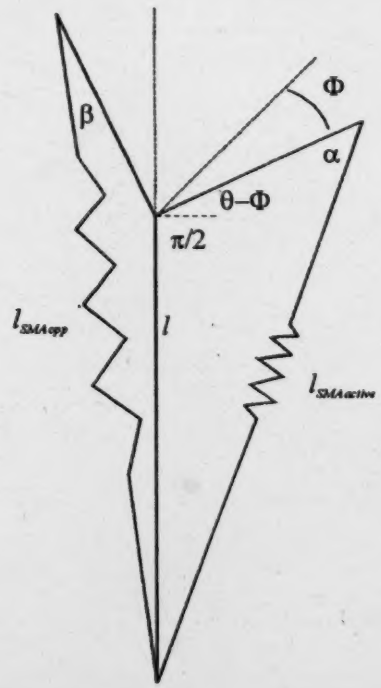

Figure 3.2: Detail of changes in length of SMA spring with respect to angle of rotation

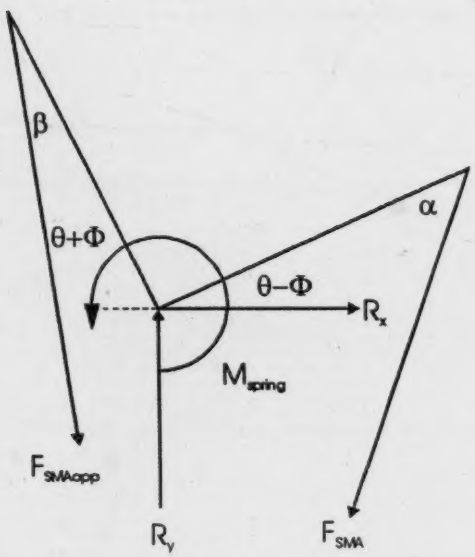

Figure 3.3: Detail of free body diagram about the pivot

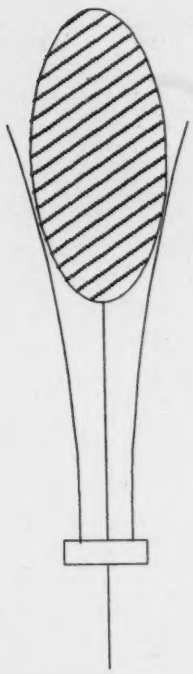

Figure 3.4: Cantilever beam bias return element

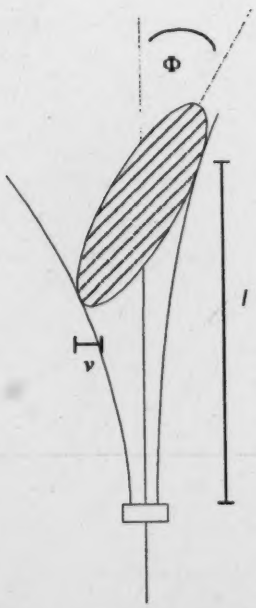

Figure 3.5: Schematic of the active bias spring element

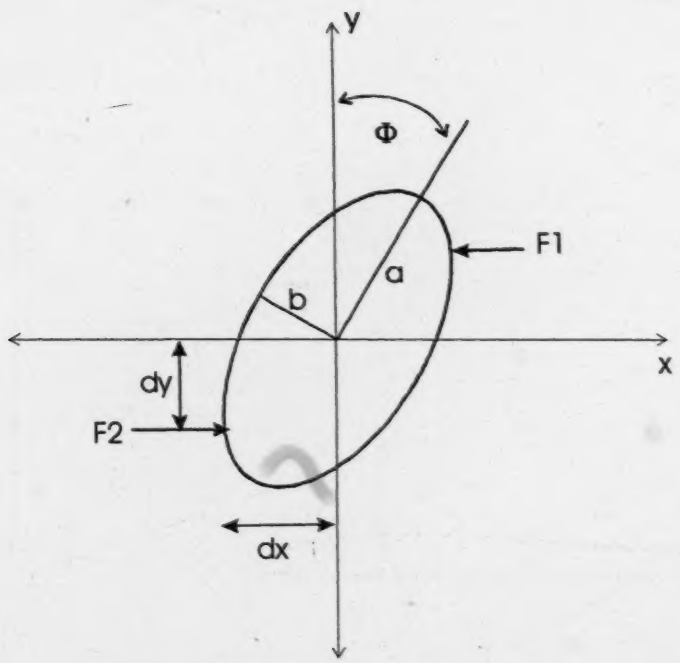

Figure 3.6: Schematic of moment calculation

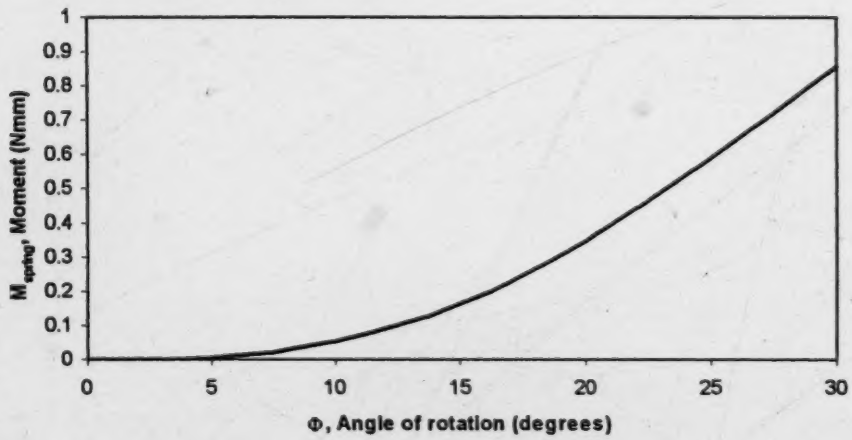

Figure 3.7: Expected Moments of Elliptical Cantilever Beam Bias Element

Figure 3.8: Schematic of the Rectangular Cantilever Bias Element

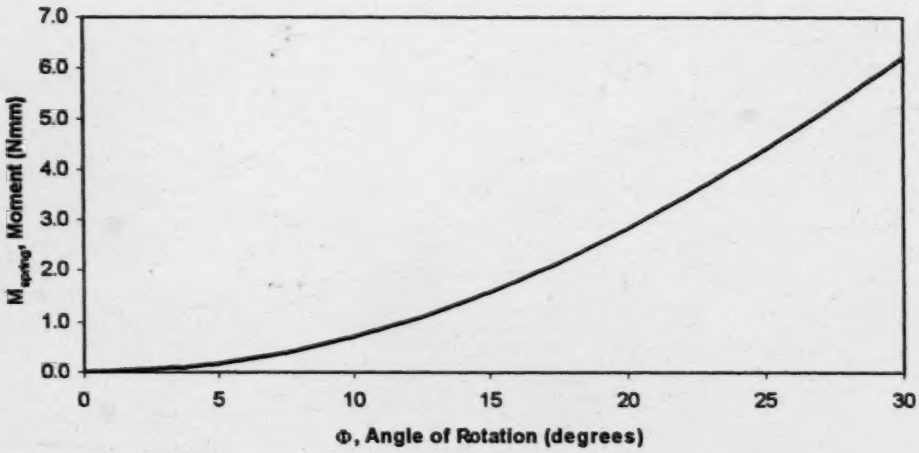

Figure 3.9: Expected Moments of Rectangular Cantilever Beam Bias Element

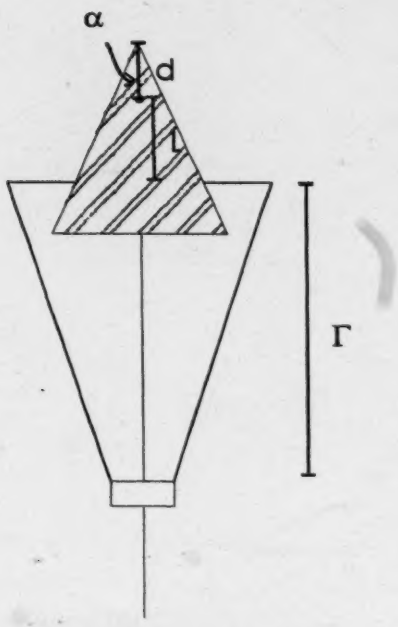

Figure 3.10: Schematic of the triangular cam shaped bias element

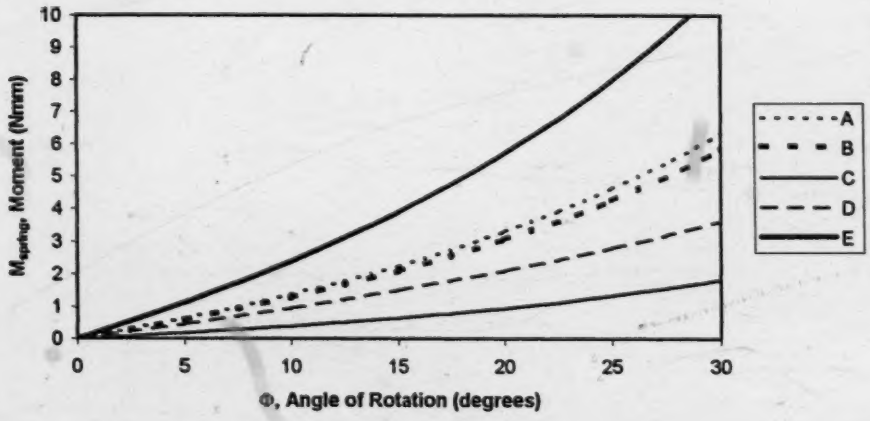

Figure 3.11: Moment of triangular cam bias spring and effects of geometry on the moment

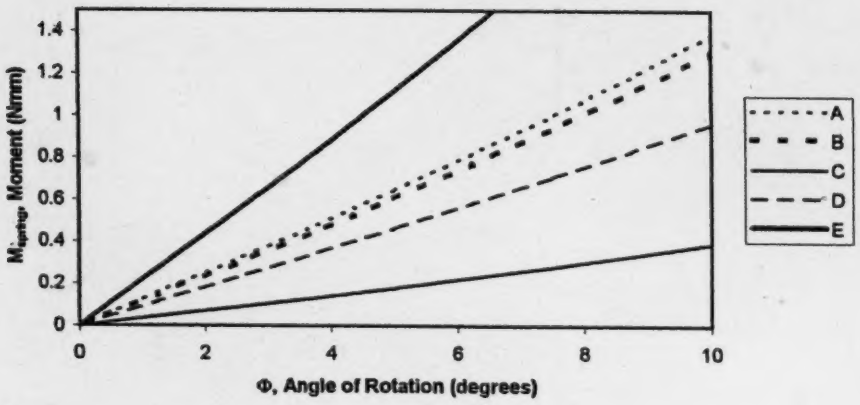

Figure 3.12: Detail of triangular element within a rotation of 10°

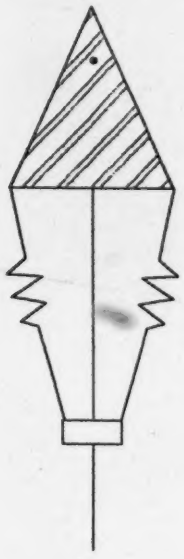

Figure 3.13: Schematic of spring bias element with triangular cam

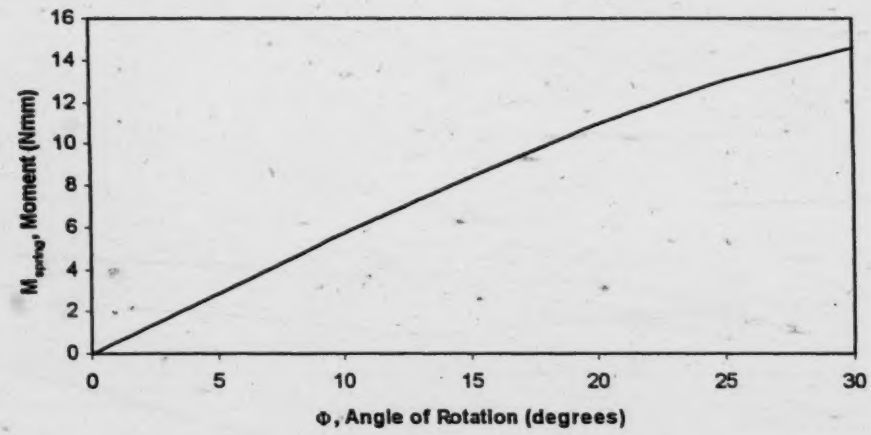

Figure 3.14: Calculated Moment for bias system with springs and triangular element

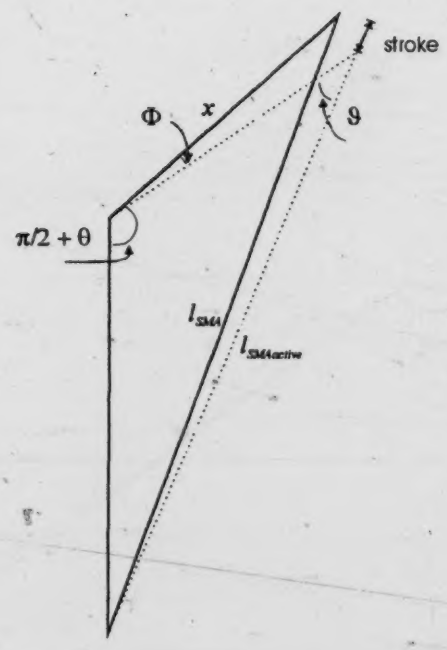

Figure 3.15: Stroke-attachment point relationship

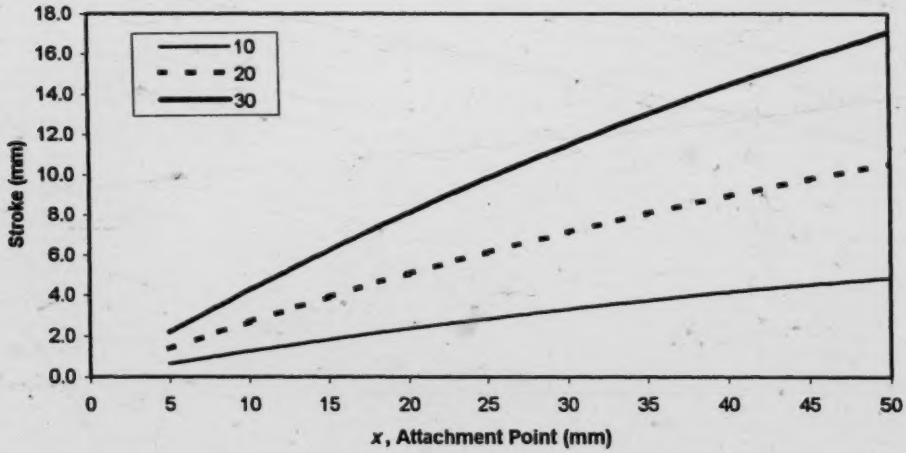

Figure 3.16: Stroke of SMA spring required for eye rotations between 10° and 30°, based of the attachment point

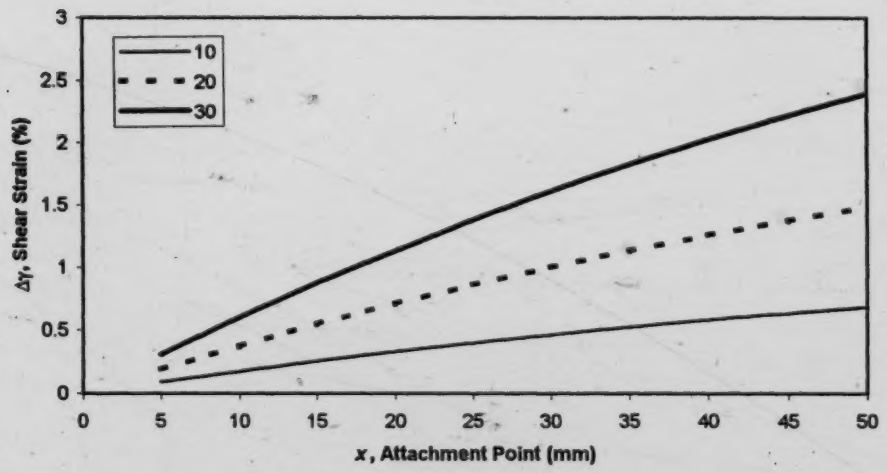

Figure 3.17: Expected Shear Strain in terms of Attachment Point for angles of rotation between 10° and 30°

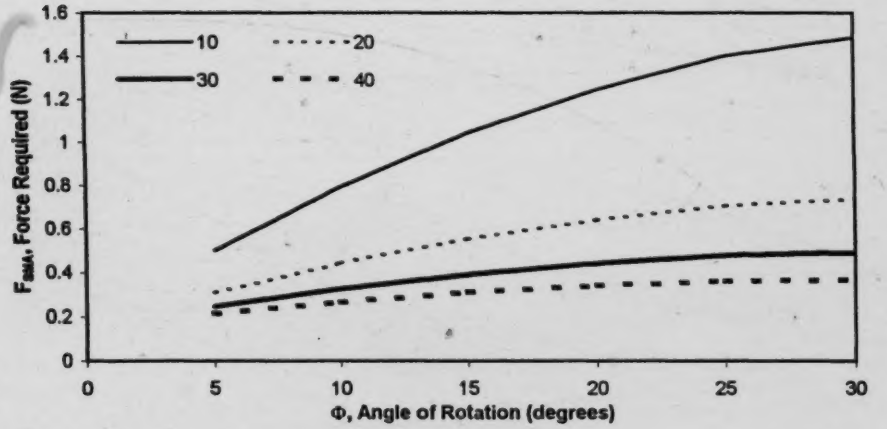

Figure 3.18: Predicted Minimum Force Required by SMA spring to rotate eye based on attachment point.

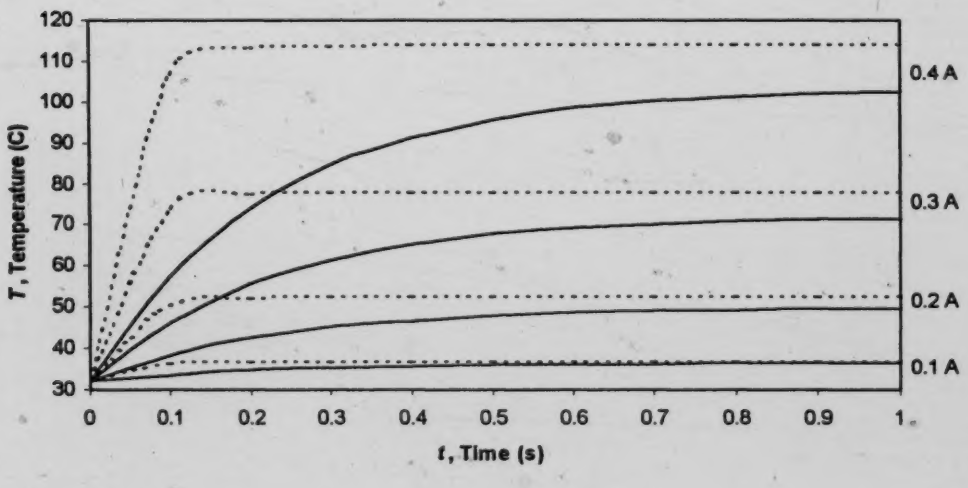

Figure 3.19: Predicted Heating for SMA wires in still air for 250 μm wire (full line) and the 100 μm wire (broken line) at various current inputs

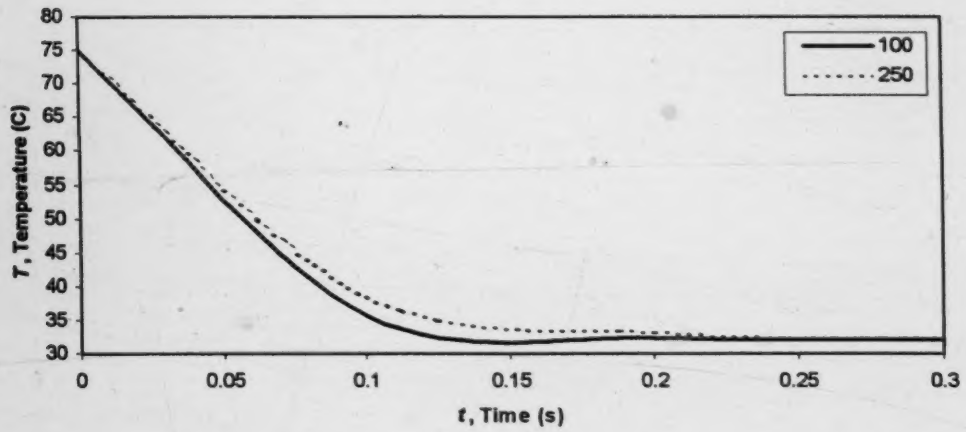

Figure 3.20: Predicted Cooling Behaviour for the 100 μm wire in still air and the 250 μm wire in forced air

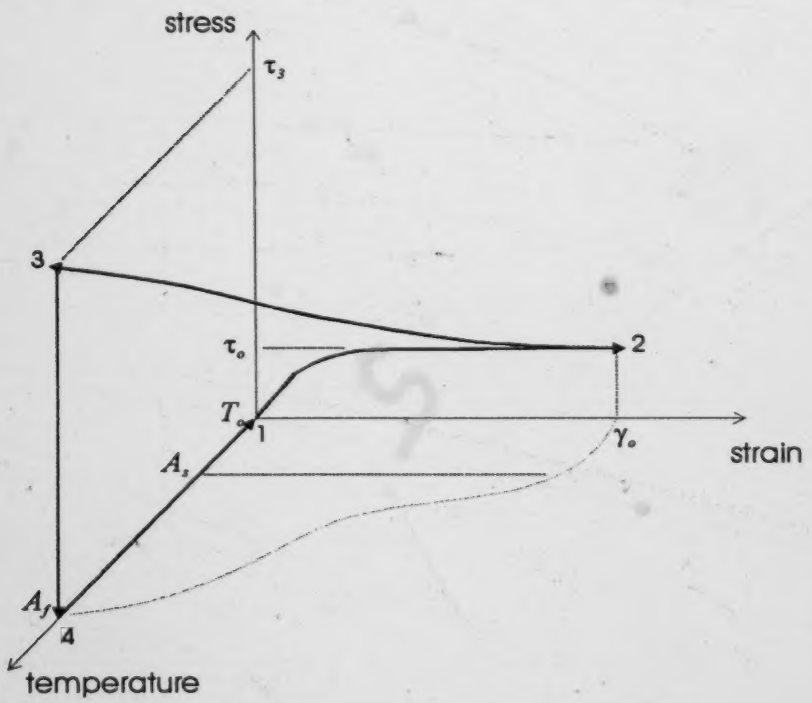

Figure 3.21: Heating cycle of SMA actuator

4 Experimental Considerations

In order to utilize the SMA springs, two general questions were required to be answered: how will the actuator be constructed from the SMA wire; and what are the recovery (actuation) forces? In this chapter, the first section addresses the thermomechanical treatment required to fabricate the SMA springs, while the second section explored the isothermal testing apparatus for measuring the stress, strain and temperature relationship of the actuator, as well as the pulse width modulation circuitry which was introduced to control the actuation.

The final section of this chapter addresses the construction of the prototype model, including the engineering drawings.

4.1 SMA spring actuator construction

Shape memory wire is available as commercially annealed wire. If the design shape is different than a straight wire, the alloy must be set to maintain the desired shape. Thermomechanical treatments are required to set the shape of shape memory alloy, which consists of constraining the deformed SMA shape followed by annealing the constrained shape. According to literature, the annealing temperature should be between 400°C and 500°C, and the anneal time from 8 minutes to 30 minutes. Dynalloy, Inc., the major distributor of Flexinol™ (binary NiTi), suggests an annealing temperature of 300°C. According to the transformation-temperature-time curve for NiTi, shown in Figure 4.1, 300°C is not sufficiently high for annealing, as the Ni_4Ti_3 region is to be avoided. This formation of this phase will act to significantly lower the transformation temperatures.

However, the transformation temperatures of the material change with thermomechanical treatment. Since the transformation temperatures are critical in the response time of the actuator, a series of annealing treatments were explored to examine the effect of time and temperature on the transformation temperatures. In addition, the shape memory effect must be retained, so the anneal cycle must be sufficient to set the new shape of the SMA. The annealing treatments used to determine this effect on the springs made are shown in Table 4.1.

Treatment	Temperature (°C)	Time (min)
A	500	20
B	500	15
C	500	10
D	400	20
E	400	15
F	400	10
G	300	15

Table 4.1: Anneal cycles used for spring construction

The wire used to make the springs was binary NiTi obtained from Dynalloy, Inc., in two A_f temperatures: 78°C and 98°C. These are the 'low temperature' and 'high temperature' actuation temperatures of the SMA wire brand Flexinol™. These specific transformation temperatures were chosen as the actuation completion temperature (A_f) was significantly above human body temperature, thus the temperature gradient for cooling would increase and the reset time of the actuator would decrease. The manufacturer specifications are listed in Table 4.2.

Wire Diameter (μm)	250
Linear Resistance (Ω/m)	20
Recommended Current (mA) - in still air at 20°C	1000
Activation Start Temp (°C) - LT/HT	68/88
Activation Finish Temp (°C) -LT/HT	78/98
Relaxation Start Temp (°C) - LT/HT	52/72
Relaxation Finish Temp (°C) - LT/HT	42/62
Annealing Temp (°C)	300
Young's Modulus (GPa) -Martensite -Austenite	 28 75
Thermal Conductivity (W/cm°C) -Martensite -Austenite	 0.08 0.18
Density (g/cc)	6.45
Heat Capacity (J/g°C)	0.32

Table 4.2: Flexinol™ Muscle Wire Properties for Flexinol™ 250. Transformation temperatures for the low temperature (LT) and high temperature (HT) wires are included.

The wire diameter used for spring construction in the prototype was 250 μm while the diameter considered for the actual model was 100 μm. According to the manufacturers specifications, these diameters would create a maximum recovery force of 5 N for the 100 μm wire in wire form. The time for cooling was between 4 and 6 s for the 250 μm wire and between 0.7 and 1.3 s for the 100 μm wire. The spring must adhere to the design parameters such that the spring index, which is the ratio of the spring diameter to the wire diameter, is between 6 and 10 (Waram, 1993). Thus, the diameters of the spring used were 2.38 mm and 0.8 mm for the wire diameters of 250 μm and 100 μm respectively.

The initial constraint mechanism used to set the spring consisted of a threaded steel rod with two nuts on each end. The wire was wound between the threads and the ends of the wire were secured within two nuts. While this was a simple procedure, the spring's pitch was too large, and it was difficult to obtain fine threaded screws with a diameter of 0.025". In a discussion with Mr. T. Waram (2001), springs with the diameter in the range required could be made with a pin vice, steel rods in the diameters for the inner diameter of the spring, a metal tube with an inner diameter slightly greater than the diameter of the steel rod, and collars. The steel rods are used to set the inner diameter of the spring. The apparatus is shown in Figure 4.2. The SMA wire was secured to the set rod by a collar. The pin vice was turned and the SMA wire was wound around the set rod. When the desired number of turns was achieved, another collar was used to hold the windings tight. When using this technique, it is necessary to both ensure even pitch by pushing the tube over the set rod to compress the windings and to hold a constant winding tension. This tension deforms the wire into the spring shape. The pin vice, set rod, collars and SMA wire were placed in the furnace and annealed. The apparatus was removed from the furnace and was water quenched. The spring was gently pushed off the set rod. The spring was stretched and heated through a number of cycles to ensure the shape was set.

The identification system for the SMA springs includes information regarding the wire diameter, coil diameter and the number of turns. For example, a 250 μm wire formed into a spring of 10 turns and a coil diameter of 2.38 mm would bear the identification tag of Spring 250-2.38-10.

4.2 Determination of Transformation Temperatures

To determine the transformation temperatures of the alloys, differential scanning calorimetry (DSC), which measures the difference in heat input between a sample of SMA and a blank over a range of temperatures, was used. An example of the

output from a DSC is shown in Figure 4.3 and the transformation temperatures are determined at the base of a peak, denoted as the A_s and A_f during heating, and M_s and M_f during cooling.

The transformation temperatures of the thermomechanically treated SMA were determined using this method.

4.3 Spring Characterization Apparatus

There were two types of experimental characterization required to understand the behaviour of the SMA actuator. First, the recovery forces obtained by actuation of the SMA wire were estimated using isothermal force-displacements experiments. The second portion of the experiments were focussed on controlling the actuation forces by the introduction of pulse width modulation.

4.3.1 Isothermal Force-Displacement Experiment

The relationship between stress, strain and temperature was determined from the force-displacement behaviour of the SMA spring using the apparatus shown in Figure 4.4. The spring was immersed in a constant temperature water bath, and anchored to a weight at the bottom of the bath. The spring was connected to a rigid rod which was attached to the end of a cantilever beam. A full Wheatstone bridge was attached at the secured end of the beam. The spring was displaced vertically, which caused a change in the force experienced by the spring.

The strain gauges were calibrated such that the spring force could be determined from the measured beam strain. A series of weights ranging from 1 g to 50 g were hung from the end of the rigid rod. The relationship between the applied force at the end of the beam and the voltage measured by the gauges is shown in

Figure 4.5. The sensitivity of the system is the inverse of the slope of the calibration curve, which is -0.33 V/N.

To obtain the stress, strain and temperature relationship, the spring was immersed into the bath. The temperature of the water bath was kept constant. The spring was displaced a few millimetres and both the displacement and strain gauge output recorded. The spring was displaced until either the strain gauge output began to increase beyond a plateau or the spring began to emerge from the water bath. The strain gauge output was converted to the force, and the force-displacement relationships were converted to shear stress and shear strain. The temperatures used were such that the phase was fully martensitic and fully austenitic. This was achieved by operating in temperatures greater than A_f and less than M_f, according to the manufacturer specifications. The temperatures used for testing the low temperature material only were 20°C and 75°C.

The relationship between stress and temperature was obtained by increasing the temperature of the water bath while holding the position of the spring. The temperature of the water bath was increased at 1°C/minute so that good mixing occurred, as well as to ensure that the temperature of the spring was equal to the temperature of the water bath. An estimate of the transformation temperatures could be obtained from the region where the stress increases rapidly. The variation of transformation temperatures with applied stress could be observed by holding various amounts of strain while increasing the temperature.

To calculate the actual strain in the spring, the displacement of the point where the beam attached to the vertical displacement device was used. However, as the force increased, the end of the beam deflected. Hence, the actual displacement of the spring was not the vertical displacement alone. The correction for the cantilever deflection can be found in Appendix B. The end deflection of the beam due to the spring force was determined to be a factor of 0.037 of the spring force.

This contribution to the total force is on the order of 0.01% and can be neglected in the deflection range of 10-40 mm.

4.3.2 Pulse Width Modulation

Applying constant current to the SMA spring could result in overheating, a non-steady state force due to continued heating and in possibly destroying the shape memory effect. To limit the heating and to better control the electrical excitation of the SMA spring, pulse width modulation was used. Pulse width modulation modulates the current by rapidly turning a switch on and off in pulses of various duty cycles. The duty cycle is the ratio between when time the current is on and the sum of time the current is on and off. An example of the output from pulse width modulation is shown in Figure 4.6. Each combination of input current, duty cycle and frequency results in a steady-state force. A circuit was developed in order to alter the current, duty cycle and frequency. The photograph of the circuit is shown in Figure 4.7 and full electrical details can be found in Appendix C.

For testing, the SMA spring was held between the cantilever beam and anchored weight. The strain gauges on the cantilever beam measured the force produced by the SMA spring. Before each test, the spring was heated to above the austenite finish temperature by electrical means, and air cooled to below the martensite finish temperature to ensure that the phase was completely martensitic. The spring was stretched according to the calculated stroke value, which was at a strain value of approximately 1.5%. Two leads were clamped to the either end of the SMA spring to connect it in series with the circuit board, as shown in the Figure 4.8. A 12 V DC battery was used to provide power for the system. The frequency range switch had three positions low, medium and high which relate to values of <1 - 22 Hz, 8 - 200 Hz, 80 - 4000 Hz respectively. The frequency and duty cycle were modified using the current and frequency adjustments, shown in Figure 4.7.

An oscilloscope measured the current, frequency and duty cycle of the input signal through the SMA spring. The oscilloscope was hooked up in parallel to a 0.96 Ω resistor which was in series with the SMA spring. The voltage output on the oscilloscope was multiplied by 0.96 to obtain the actual current delivered to the SMA spring.

The current was adjusted between 0.8 A to 1.0 A, the duty cycles between 5% and 50% and the frequencies between 1 and 400 Hz. The circuit was activated and the time varying voltage output from the strain gauges and circuit output were collected using an InstruNet Model 100 A/D I/O System. The voltage output was converted to a force using the same methodology as the isothermal experiment procedure. The relationship between SMA force output and time was obtained for the various factors. The actual frequency and duty cycle were determined from the circuit output data.

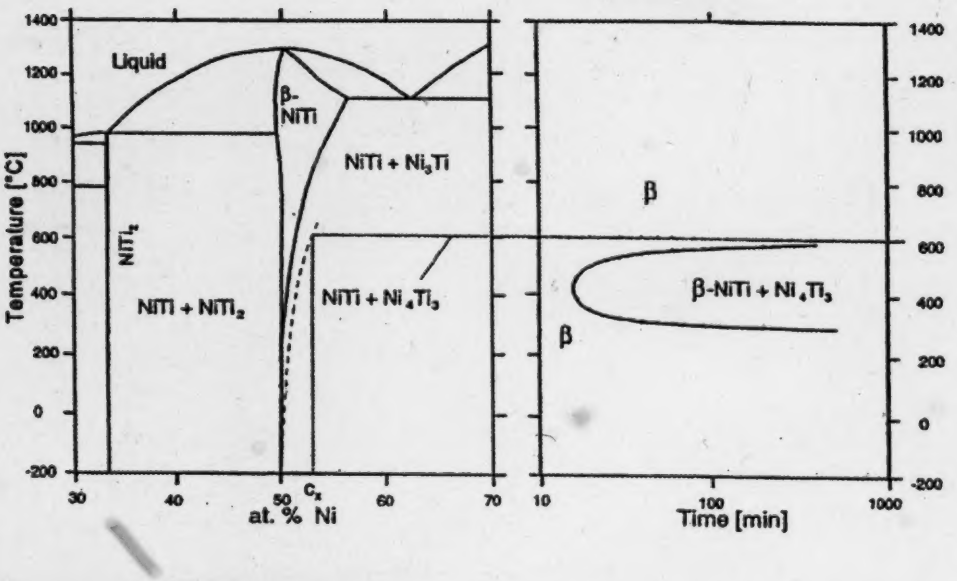

Figure 4.1: Phase diagram and corresponding time-temperature-transformation curve for NiTi (adapted from Hornbogen (1997))

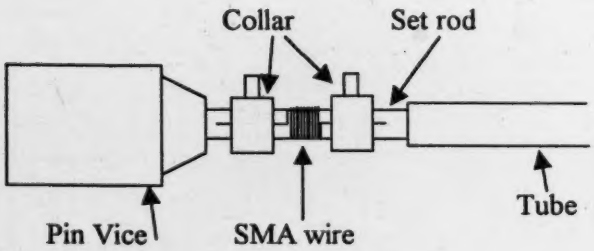

Figure 4.2: Schematic of Apparatus for Setting SMA Springs

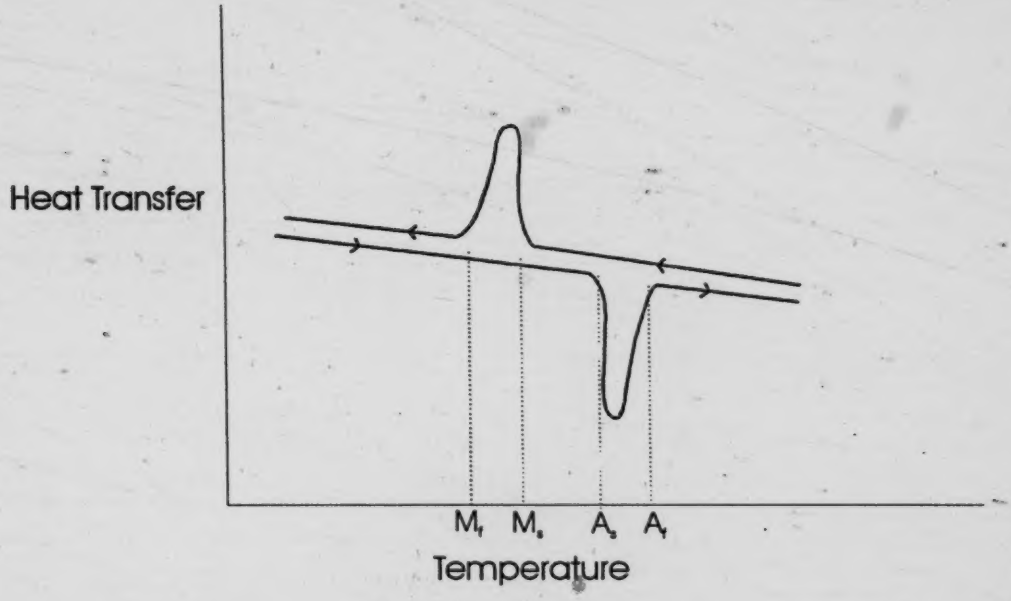

Figure 4.3: Example of output from DSC

a)

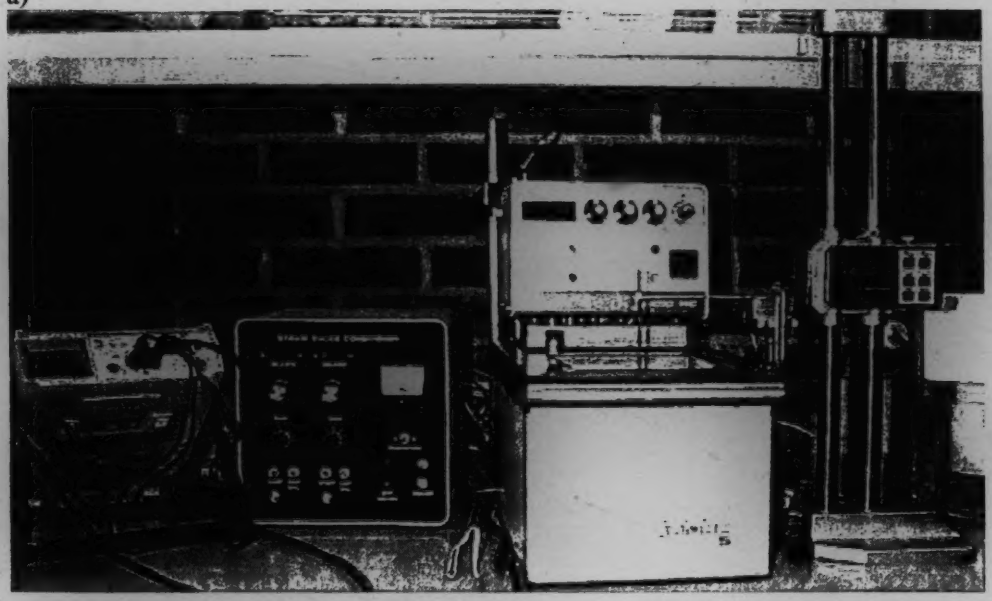

b)

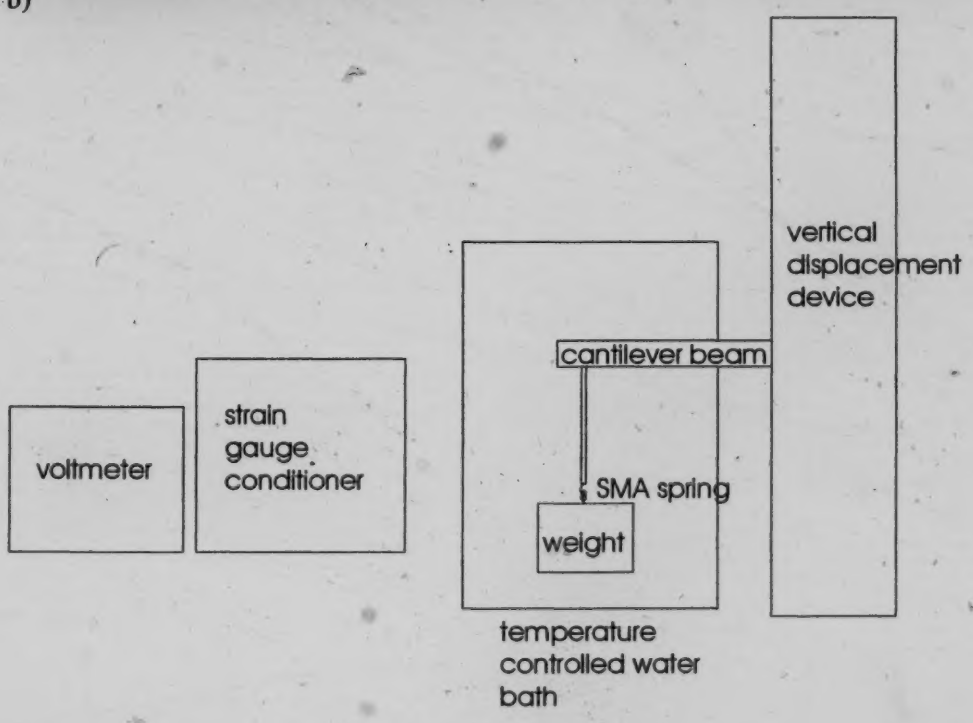

Figure 4.4: Isothermal Force-Displacement Apparatus a) digital photograph and b) block diagram

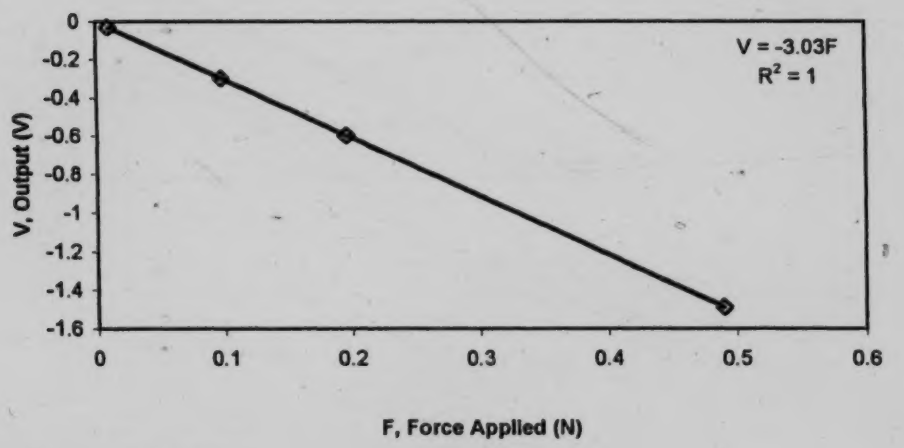

Figure 4.5: Calibration of Strain Gauges on Cantilever Beam

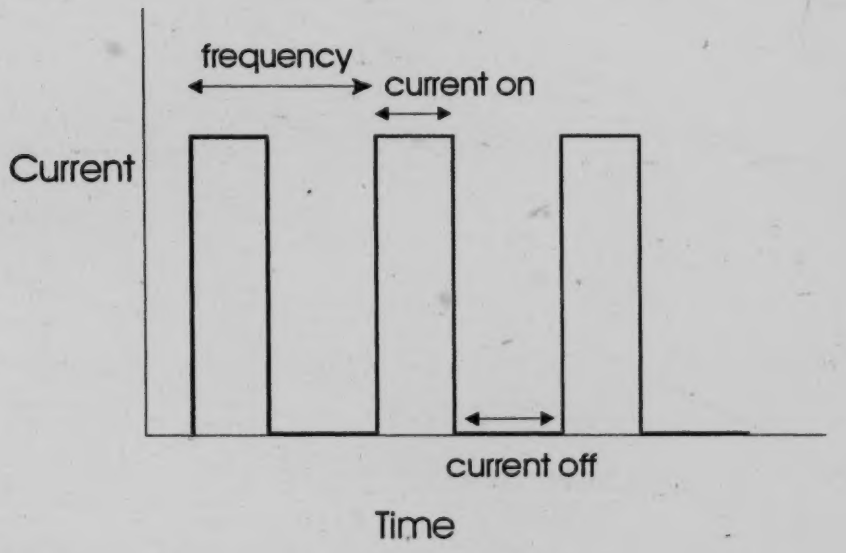

Figure 4.6: Step output of PWM denoting frequency and duty cycle. Duty cycle is the ratio between the time current is on and the sum of the time the current is on and off.

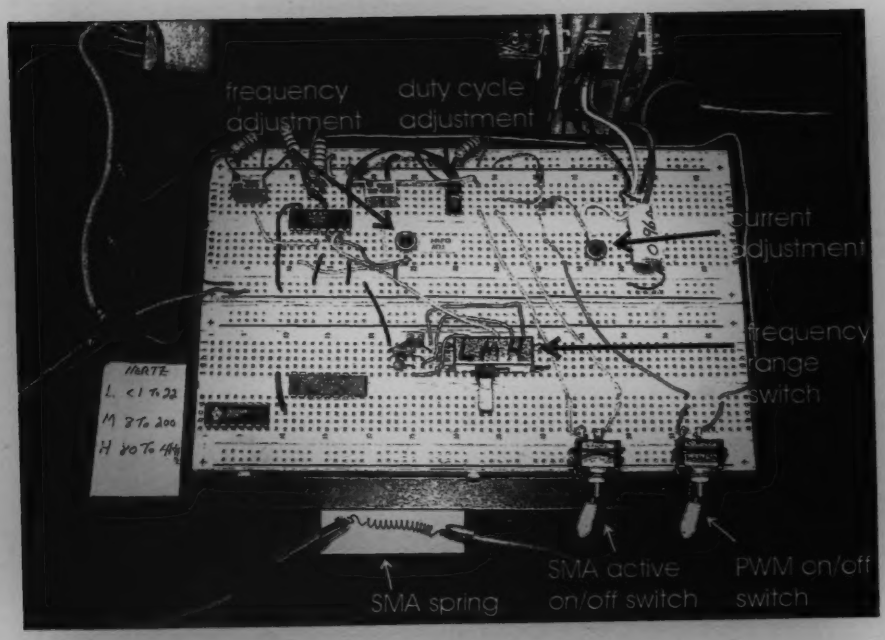

Figure 4.7: Schematic of Pulse Width Modulation Circuit

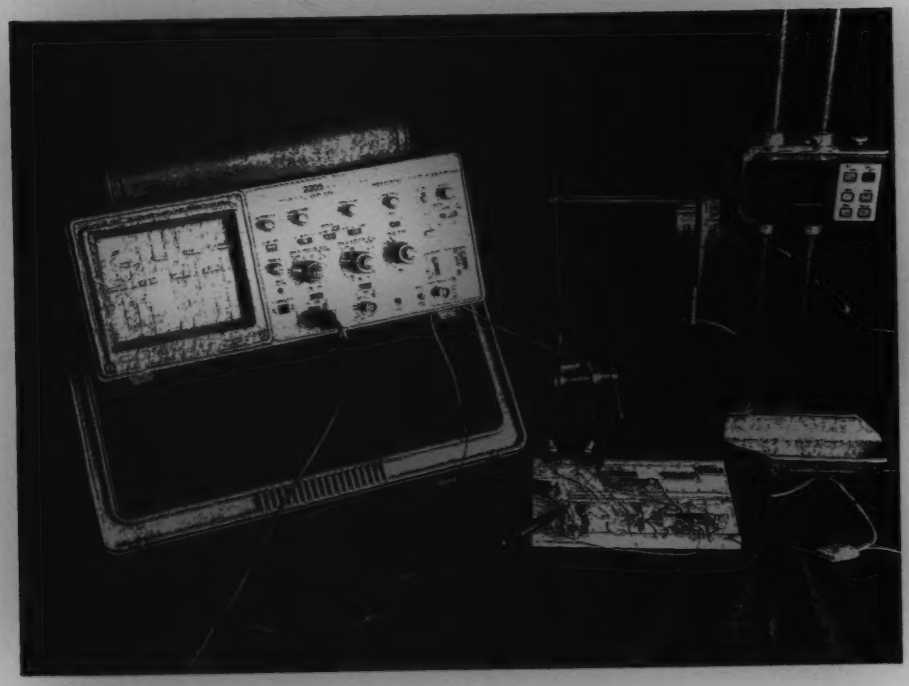

Figure 4.8: Assembly for PWM experimentation of SMA spring

5 Results and Discussion

The results regarding the questions posed in Chapter 2 are discussed, with respect to:

- the forces obtained by SMA springs;
- the current required to activate SMA springs;
- the transformation temperatures of the SMA which play a role in the heat transfer and relaxation time;
- the use of pulse width modulation to control the SMA spring.

5.1 Actuation Forces of the SMA Spring

The SMA spring was tested in the water bath at two temperatures to ensure that the force-displacement characteristics are measured when the spring was fully austenitic and fully martensitic. According to the manufacturer specifications, the martensite finish temperature was 42°C and the austenite finish temperature was 78°C for the low temperature activating material. During the experimental design stage, however, the austenite finish transformation temperature was advertised on the website as 70°C. As such, the temperatures were chosen as 25°C for martensite and 75°C for austenite. It is later revealed that the transformation for the low temperature material is complete at 70°C. The force-displacement output is shown for Spring 250-2.38-65 in Figure 5.1. The triangle data series is the output for the martensitic phase, and the circle data series is the austenitic phase. The portion of the martensite curve which changes slope is the point where the twin boundaries are being removed - this will be called the yielding force. The yielding force for the martensite is 0.2 N at a spring extension of 60 mm. The force increases to 0.43 N upon heating to the austenite phase. According to the force required for the prototype model of at least 0.5 N, this spring design is not sufficient to deliver actuation to the rotation of the ocular element of the prosthesis.

As the slope of the initial linear portion of the graph is related to the shear modulus of the SMA, Figure 5.1 indicates that the slope of the austenite phase is significantly larger than that of the martensite phase. Hence, the difference in mechanical properties of the two phases is apparent.

The number of active turns of the spring was decreased to 20 for the second experiment. The results of this experiment are shown in Figure 5.2, which includes the unloading path as well. The loading portion of the test for the austenite phase is the upper circle data points. The lower data points of the

austenite curve represent the unloading of the axial stress. The axial loading and unloading for the austenite phase followed a closed loop, that is, there is no accumulated displacement. This does not occur with the martensite loading and unloading cycle. In the martensite phase, the twin boundaries are removed by the application of the axial force, and upon the removal of the force the reversal of the twin boundaries does not occur, and hence, there is an accumulation of displacement.

The yield force of the martensite phase estimated from Figure 5.2 is 0.15 N at a displacement of 10 mm. The austenite yielding point is more difficult to determine, however, it was selected as the point at which the loading and unloading cycles meet. As such, the force is 0.45 N at a displacement of 15 mm. Although the yielding forces are similar for the two springs, the maximum force obtained from the spring with 20 active turns is up to 0.8 N, which is greater than the maximum observed with the 65 turn spring of 0.45 N.

As the yielding forces of both springs are similar, the number of active turns does not appreciably affect the yielding force, but do play a role in the difference in displacement between the martensite and austenite phases. This difference increases the stroke available for the actuation cycle.

The force-displacement results obtained were converted to shear stress-shear strain values so that the change in shear strain could be determined to ensure that the limit of 2% is adhered to for fatigue minimization. Shown in Figure 5.3 is the shear stress-shear strain relationship for Spring 250-2.38-20. For this spring, the shear strain cycle tested was up to 1%, which is less than the 2% strain maximum imposed by the design criteria of the SMA. Consequently, the displacement cycle of the spring can be increased up to 70 mm without concern for fatigue failure.

A spring was constructed of the 100 μm diameter SMA with a coil diameter of 0.8 mm and 55 active turns. The spring was loaded axially at three different

temperatures: 25°C, 54°C and 75°C. The middle temperature of 54°C was chosen to determine how the force and displacement change with temperature. The results of this experiment are shown in Figure 5.4. The maximum forces obtained are 0.06 N in the martensite phase and 0.25 N for the austenite phase. The trial at 54°C does not show the repeatability that the runs at 75°C and 25°C demonstrate. This may be due to the fact that the temperature control was not consistent. Small variations in temperature significantly affect the response of shape memory alloys when the temperature is between the transformation start and finish temperatures.

The effect of martensite fraction on the behaviour of mechanical properties of SMA is demonstrated. A linear regression of the slopes of the initial portion of the graph was performed and the results compared. As explained previously, the slopes are directly proportional to the shear modulus. The martensite fraction decreases with increasing temperature between 25°C and 75°C. The linear assumption of the change of shear modulus with martensite fraction, described in Chapter 2, is reasonable according to Figure 5.5, even though only three data points are present.

The transformation temperatures of two springs were estimated by applying a strain of 1.5%, heating the bath of the water and measuring the reaction force. The reaction force was converted to shear stress using equation 3.19. The graphical results are shown in Figure 5.6. The transformation temperatures are estimated from the point where the slope changes significantly, the first change being the austenite start temperature and the second change being the austenite finish temperature. Although a crude method, the transformation temperatures for the springs are significantly less than those reported by the manufacturer of 68 °C and 78 °C for austenite start and finish temperatures respectively. The results are summarized in Table 5.1.

Transformation Temperature	Spring 250-2.38-20	Spring 250-2.38-65
Austenite Start	42 °C	45 °C
Austenite Finish	50 °C	55 °C

Table 5.1: Transformation Temperatures Estimated by the Water Bath Apparatus

The effect of initial strain (or stress) on the SMA spring is shown in Figure 5.7. As the strain increases, the transformation temperatures increase. The austenite start temperatures are estimated at 42 °C for both strain levels, however the austenite finish temperature increases from 45 °C at no strain to 50 °C at 0.6% strain. This coincides with the results described by Tanaka (1984) who found that the transformation temperatures increase linearly with stress. Since the transformation temperatures estimated from Figure 5.6 are similar with those found in Figure 5.7, it was concluded that the strain and thermomechanical treatments imposed on the SMA spring affect the transformation temperatures.

5.2 Current Activation by Pulse Width Modulation (PWM)

Combinations of duty cycle and frequency were explored to investigate the increase in force and the actuation velocity. While the maximum current recommended by the manufacturer was 1 A, to minimize the currents used in the experiment, those investigated were 0.8 to 0.9 A. The currents were reduced to utilize less power. Currents less than 0.8 A for the 250 μm wire took the SMA spring significantly longer time to contract.

Shown in Figure 5.8, is the increase in force with respect to time with various duty cycles. As the duty cycle increases, the maximum force is obtained within a faster time. In addition, the stability of the force increases with duty cycles above 20%.

The increase in force due to the PWM frequency for Spring 250-2.38-20 is shown in Figure 5.9. It can be seen that as the frequency increases, the change in force decreases non-linearly. The force approaches to a maximum of approximately 0.5N as the frequency is decreased. With a frequency greater than 50 Hz, the change in force can be estimated as a constant depending on the duty cycle. An increase in the duty cycle results in an increasing change in force, for frequencies below 40 Hz. This is due to the fact that as the duty cycle increases, the effective current increases. The increase in current will increase the temperature of the SMA wire. It appears that a minimum duty cycle, and hence a minimum current, is required for complete activation, as there is no significant difference in the results for duty cycles of 45% and 61%. This would correspond to a minimum average current of 0.3A.

The speed of activation changes more significantly with duty cycle than the increase in force. Shown in Figure 5.10, a non-linear relationship between actuation speed and frequency is observed. The speed increases with duty cycle; comparison of the steady-state actuation speeds are 0.03 N/s, 0.08 N/s and 0.15 N/s for 28%, 45% and 61% duty cycles respectively. This is due to the fact that the effective current increases with increasing duty cycle. Thus, the increase in current causes the temperature of the SMA wire to increase which in turn results in the time to reach the transformation temperature to decrease. As the frequency decreases, the actuation speeds converge to value of 0.05 N/s, 0.015 N/s and 0.2 N/s for duty cycles of 28%, 45% and 61% respectively.

With an applied current of 0.9 A at 100% duty cycle, the Spring 250-2.38-20 obtained a change in force of 0.48 ± 0.05 N with a change in actuation force with respect to time of 0.34 ± 0.02 N/s. The change in force is not a significant increase over the lower duty cycle tests; however, the change in actuation force with respect to time has significantly increased. As a result, for the most rapid changes in eye rotation, the upper limits of current and duty cycle are required.

This behaviour is shown in Figure 5.11, with Spring 250-2.38-20 of low temperature material. The offset of the two configurations is due to a difference in starting time, as the runs were held independently. If the two were adjusted to begin at the same time, differences in the two runs would be difficult to determine. This figure shows that:

- If the frequency is decreased to the low frequency selector range, step like changes in force occur. This is beneficial when mimicking quick changes in eye rotation.
- The amount the spring is initially stretched will dictate the amount of maximum force obtained by the spring. As long as the shear strain cycle is less than 2%, failure should not be a problem in the design.
- The time to reset of the spring is increased when more initial extension is applied to the spring. The additional force will expedite the time for the spring to return to its previous shape.

Further modelling of the PWM experimental results would be able to create a look-up table with respect to the desired amount of eye rotation, velocity and acceleration.

5.3 Transformation Temperatures

The transformation temperatures were determined from the output of the differential scanning calorimeter (DSC) and are summarized in Table 5.2. The most readily available DSC was capable only in controlled heating, so only austenite temperatures could be accurately detected.

Material	Thermomechanical Treatment	Austenite Start (°C)	Austenite Finish (°C)
Low Temperature Flexinol™	400 °C, 20 min	44 ± 2	54 ± 2
	400 °C, 10 min	44	58
	500 °C, 20 min	42 ± 9	47 ± 12
	500 °C, 10 min	39	44
High Temperature Flexinol™	400 °C, 20 min	65	77
	400 °C, 10 min	63	75
	500 °C, 20 min	87 ±1	96 ± 2
	500 °C, 10 min	87	-

Table 5.2: Results of DSC Analysis for austenite transformation temperatures from Thermomechanical Treatments of Flexinol™ Shape Memory Alloy

As can be seen, the transformation temperatures are significantly affected by the thermomechanical treatment imposed, as well as the specific material used.

The transformation temperatures of the As-Is material, shown in Table 5.3, were not within experimental error of the manufacturers specifications, shown in Table 4.2. They were found to be up to 30 °C less on the high temperature material. Although the manufacturers specifications are averages, the confidence limits associated with their results were not available. The martensite transformation temperatures for the low temperature material were unable to be accurately determined using DSC analysis. SMA-Inc. (San Jose, CA, USA) reported that the transformation temperatures of partially cold worked materials can lead to inconclusive results.

Material	Austenite Start (°C)	Austenite Finish (°C)	Martensite Start (°C)	Martensite Finish (°C)
Low Temperature	47.9 ± 8.9	60.5 ± 3.4	-	-
High Temperature	74.1 ± 2.4	76.0 ± 2.2	47.9 ± 1.3	36.2 ± 0.6

Table 5.3: Results of DSC Analysis for the transformation temperatures from As-Is Flexinol™ Shape Memory Alloy

The differences in transformation temperatures is due to the fact that thermomechanical treatments modify the number of lattice defects in the material and as such, affects the nucleation and propagation of diffusionless transformations. From Figure 4.1, a third metastable phase, Ni_4Ti_3, is formed under certain conditions. If the composition is not exactly 50 at. % Ni and 50 at. % Ti, and the alloy is heated, this phase precipitates out of solution. This phase is bounded by the nose-shaped curve, and is a function of the composition. As the alloy composition reaches a pure binary state, this nose curve disappears. If this phase does not appear, then as the thermomechanical treatment severity increases, the transformation temperatures should decrease. The presence of this metastable phase should act to compound the effect. Treppmann and Hornbogen (1997) found that the transformation temperatures are shifted a significant amount when the annealing temperature is above 200°C. They also stated that defects introduced in the austenite phase are carried into the martensite phase which act to lower the M_s.

The transformation temperatures obtained in Table 5.2 and Table 5.3 do not follow expected results. It was anticipated that the transformation temperatures would decrease with an increase in annealing temperature and time. However, this is not shown in the high temperature material. This leads to the fact the strain imposed on the shape memory alloy before the thermal treatment is very important in the depression of transformation temperatures. In addition, the annealing temperature has a greater effect on the transformation temperatures than does the annealing time within the range of factors tested.

Due to the variation in the results shown in Table 5.2, the transformation temperatures were obtained again using stricter controls. A spring was constructed in the same manner as used for the actuator, (made from both the low temperature and high temperature materials), and subjected to the annealing temperatures shown in Table 5.4. The annealing time was 15 minutes for all tests. The DSC at the Alberta Research Council was used to determine austenite and

martensite temperatures, as well as the effect of transformation temperature on heating/cooling rate.

Material	Annealing Temperature (°C)	Martensite Start (°C)	Martensite Finish (°C)	Austenite Start (°C)	Austenite Finish (°C)
Low Temperature Flexinol™	289 ± 16	57.6 ± 2.7	39.1 ± 1.6	38.5 ± 0.6	64.5 ± 3.9
	390 ± 6	55.2	40.5	43.4	58.5
	493 ± 8	40.2	36.9	40.3	43.8
High Temperature Flexinol™	289 ± 16	64.7	39.6	41.9	67.1
	390 ± 6	59.4 ± 0.4	54.0 ± 1.0	59.3 ± 1.6	73.8 ±5.8
	493 ± 8	56.6 ± 0.4	52.2 ± 0.3	85.5 ± 1.5	91.4 ± 1.3

Table 5.4: Transformation temperatures of SMA springs

Several important factors arise from the information in Table 5.4. Firstly, the martensite finish temperatures for the low temperature material are relatively constant, and are too low for application in the robotic eye, as they are below 45°C. It is desirable to have the martensite transformation temperatures as high as possible, while ensuring that the austenite transformation temperatures are as low as possible.

Secondly, a trend of the austenite transformation temperatures for both the low temperature and high temperature material was investigated, and shown in Figure 5.12 and Figure 5.13 respectively. This nonlinear trend indicates that an event occurs surrounding an anneal temperature of 250°C. The nose-curve described in Figure 4.1 can be the cause of this event, with the nose peaking at 250°C. At an anneal temperature of 300°C, the metastable phase is being produced, which acts to depress the transformation temperatures more than expected. As the anneal temperature increases beyond the nose-curve region, the transformation temperatures rise due to the lack of the metastable particles. It is expected that with an increase in annealing time or temperature that these temperatures would begin to decrease.

Thirdly, the low temperature and high temperature material show different trends, which could be attributed to the manufacturing, processing or chemical composition. This information was not available, so the exact cause to the differences could not yet be determined.

The thermomechanical treatment recommended for this application is restricted for use only on the high temperature material, due to the ranges of transformation temperatures obtained. Due to the possible presence of a metastable phase, and any further complications this may introduce to the problem, the 300°C anneal was not recommended.

The 500°C anneal appears adequate according to the transformation temperatures obtained. The variation at the 95% confidence interval is ± 1.5°C. However, two additional phenomenon suggest this anneal is inappropriate. Shown in Figure 5.14, is the DSC output for the 500°C annealed high temperature material. Upon, cooling, two peaks appear: the first one is called the R-phase transformation and the second is the martensite transformation. This R-phase is a third phase which has been shown to appear in shape memory alloy transformations, and can attribute to an approximately 0.5% change in strain. Although this only appears in the relaxation state, where control of the SMA is not key, it is unclear what other complications may arise. More importantly is the range of austenite transformation temperatures. With a larger range, better control of the SMA spring with respect to displacement can occur. The range of austenite temperatures with the 500°C anneal was 5.7°C, whereas the range for the 400°C anneal was 18.7°C. Shown in Figure 5.15 is the DSC output for the 400°C anneal of the high temperature material, which shows the expected DSC output behaviour of equal magnitude peaks, with the austenite start temperature coinciding with the martensite start temperature. This behaviour is typical of austenite-martensite behaviour.

As such, the recommended anneal for constructing the SMA springs given the high temperature Flexinol™ wire is 400°C for 15 minutes.

5.4 Prototype Validation

The drawings to manufacture the robotic eye prototype are shown in Appendix D. The material chosen was stainless steel for the mechanical support, due to the high humidity inside the eye cavity. Shown are two separate components, the V-brace and the support arm. The V-brace is held in the support arm by two setscrews. The SMA springs are attached between the V-brace, 30 mm from the pivot point, and the base of the support arm. To construct the actual model, the scale can be adjusted such that the actuation system fits inside the orbital.

Shown in Figure 5.16 are digital photographs of the prototype model from the top (a), side (b) and front (c). The model was connected to the PWM circuit board through a pulsed spray controller. This controller sends the current from one activation SMA wire to the other, in order to simulate an eye moving back and forth. The top view of the prototype in an active state is shown in Figure 5.17 which shows a detailed view of both directional rotations. A full view of the system in the active state is shown in Figure 5.18.

The spring design used for the model was high temperature 250-2.38-15, initially stretched to 80 mm. The spring would be able to contract to 60 mm, which provides for the maximum stroke required to rotate the eye to 30° as well as a maximum force of 1.2 N, sufficient for the 0.5 N requisite.

The settings on the circuit were adjusted to determine if the system could be controlled in this manner to obtain various speeds and angles. The results are summarized in Table 5.5.

Frequency (Hz)	Duty Cycle (%)	Spray time (seconds)	Angle (°), from zero
8	47	5/10	±20
11	30	5/10	±10
11	47	5/10	±15
11	60	5/10	±15
28	47	5/10	±20 °
28	47	2.5/5	±11
28	47	1/10	10° to 20°
111	47	5/10	±20
275	47	5/10	±25
Continuous	47	5/10	±30
Continuous	47	2.5/5	±30

Table 5.5: Summary of angle of rotation available for PWM variables with an input current of 0.8 A. The first number in the spray time is the amount of time the PWM signal was delivered to one arm of the actuator. The second is the total time of the spray cycle, that is, the time the PWM is delivered to one arm followed by the other.

When the frequency was in the lower frequencies, the SMA spring contracted in step like motions. If used in combination with a one second on/one second off cycle, the eye can rotate back and forth in a 5° range. As the frequency is decreased, the steps become longer and the movement range increases to 10°.

The unit was left to operate for 1000 cycles and no failure occurred.

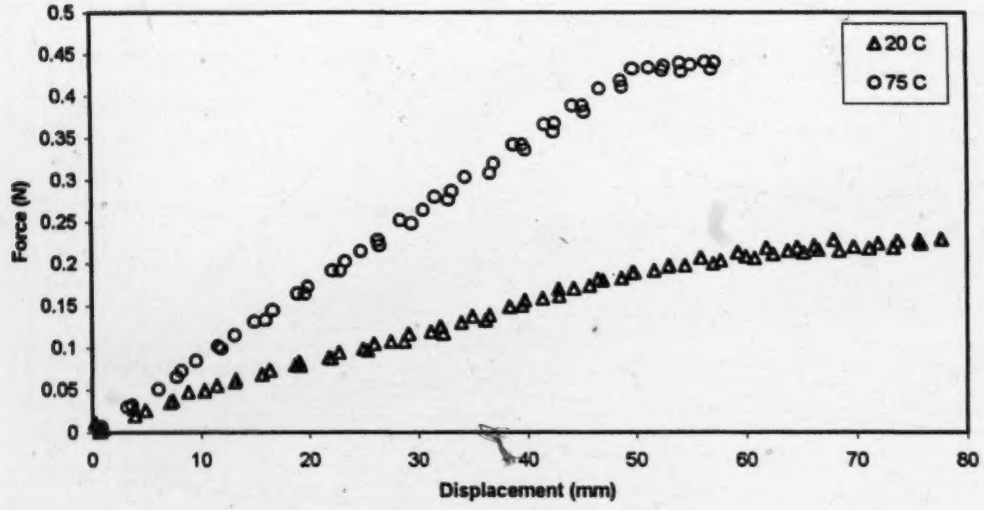

Figure 5.1: Isothermal Force-Displacement Results for Spring 250-2.38-65

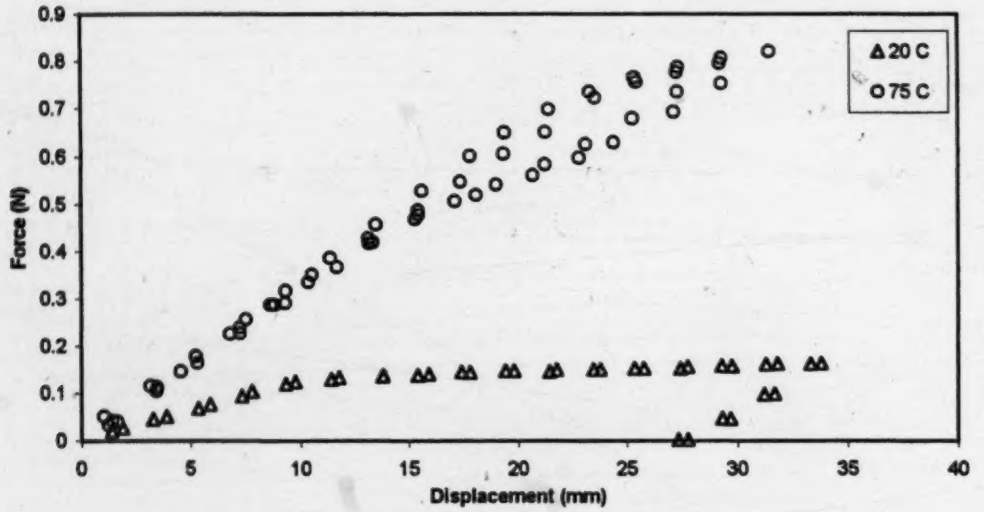

Figure 5.2: Isothermal Force-Displacement Results for Spring 250-2.38-20

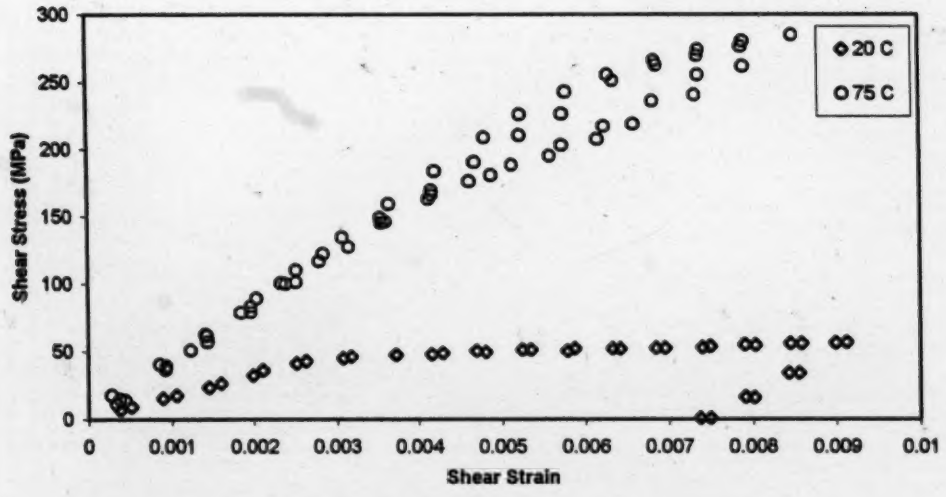

Figure 5.3: Shear stress-shear strain relationship for Spring 250-2.38-20

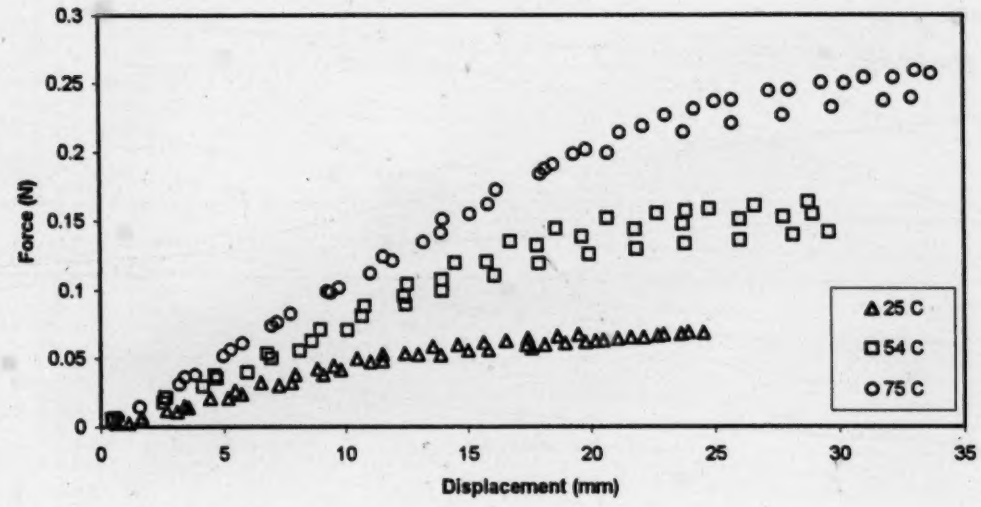

Figure 5.4: Isothermal Force-Displacement Results for Spring 100-0.8-55

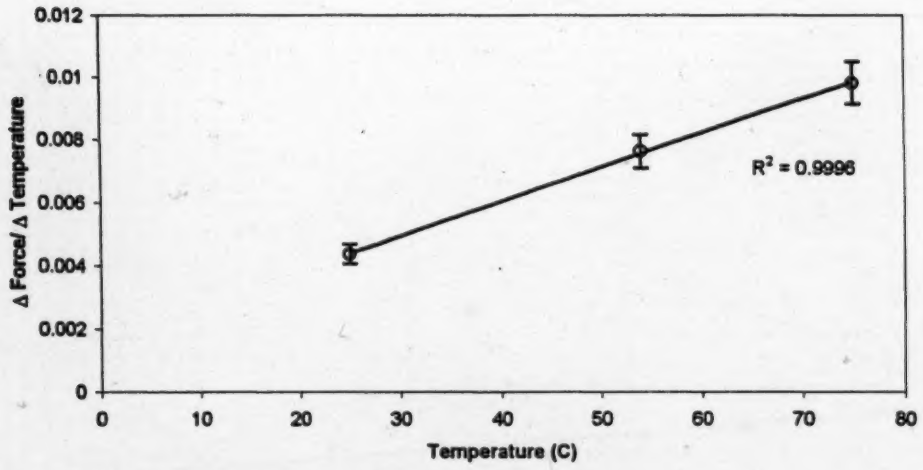

Figure 5.5: Change in mechanical properties with temperature (martensite fraction)

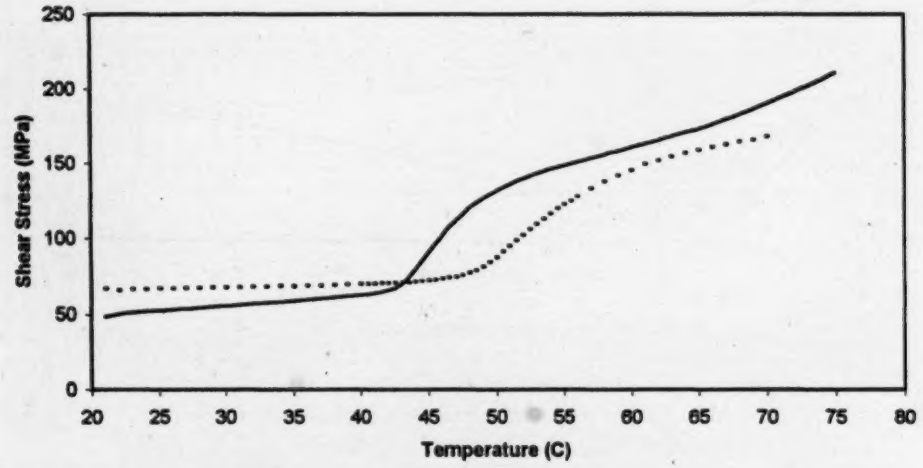

Figure 5.6: Isostrain (ε=1.5%) relationship between stress and temperature to estimate transformation temperatures. The full line is Spring 250-2.38-20 and the broken line is Spring 250-2.338-65.

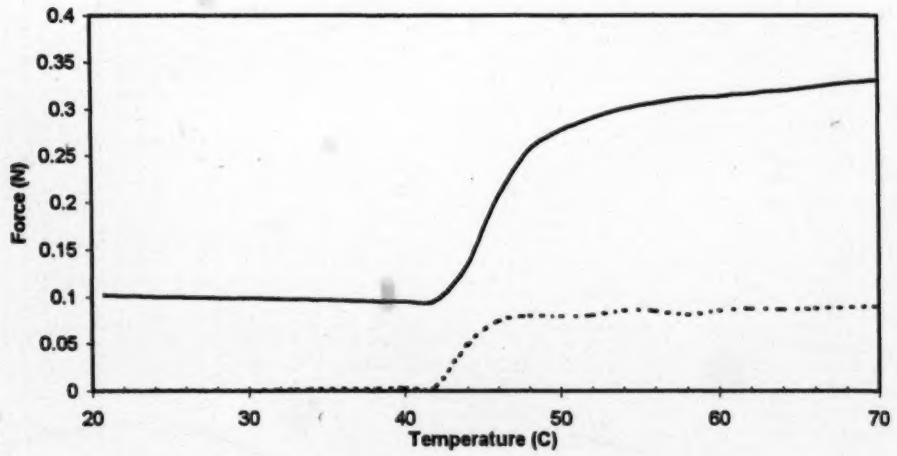

Figure 5.7: Change in transformation temperatures with differing initial strains on Spring 250-2.38-65. The solid line has a strain of 0.6% and the broken line has no initial strain.

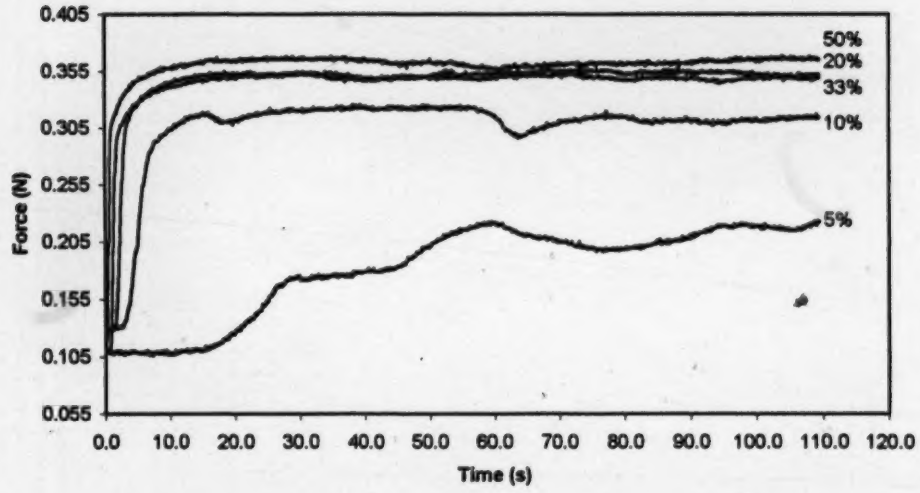

Figure 5.8: Change in Force with Increasing Duty Cycle for Spring 250-2.38-20 (Current=0.8A, Frequency=400Hz)

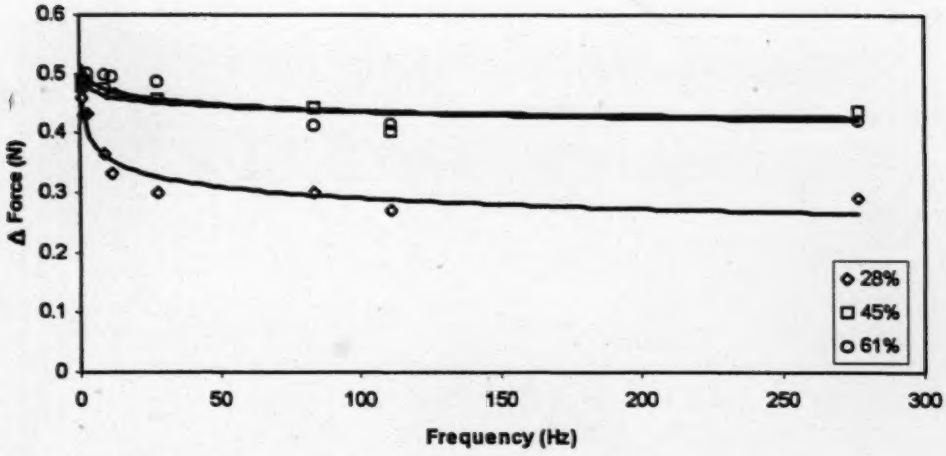

Figure 5.9: Increase in Force with Frequency based on 3 variations of duty cycle (Spring 250-2.38-20)

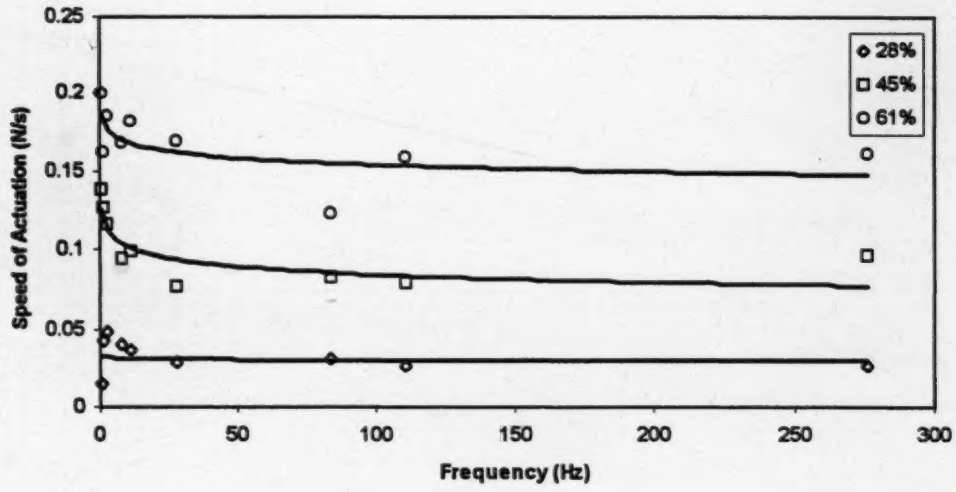

Figure 5.10: Actuation Speed with Frequency based on 3 variations of duty cycle (Spring 250-2.38-20)

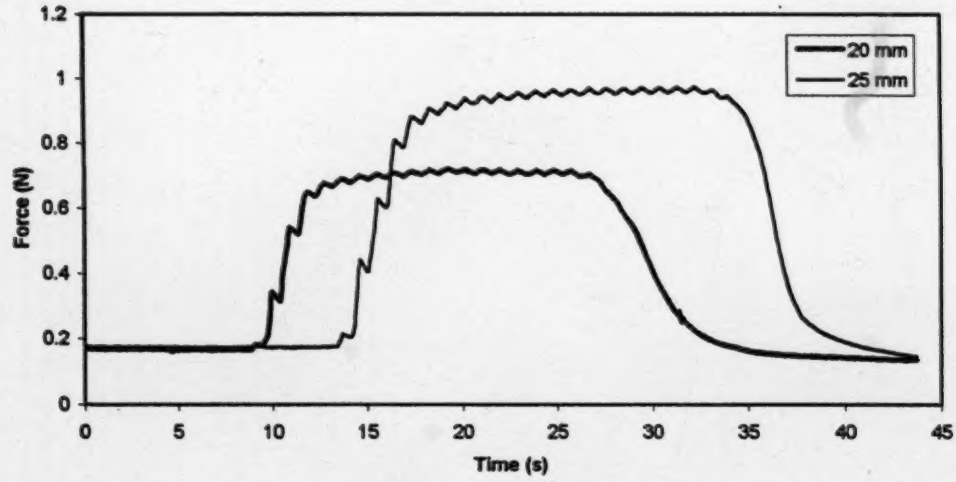

Figure 5.11: Step-like force changes for Spring 250-2.38-20 with low frequency, and increase in force with increase in stroke. The spring was extended both 20 mm and 25 mm from its original length.

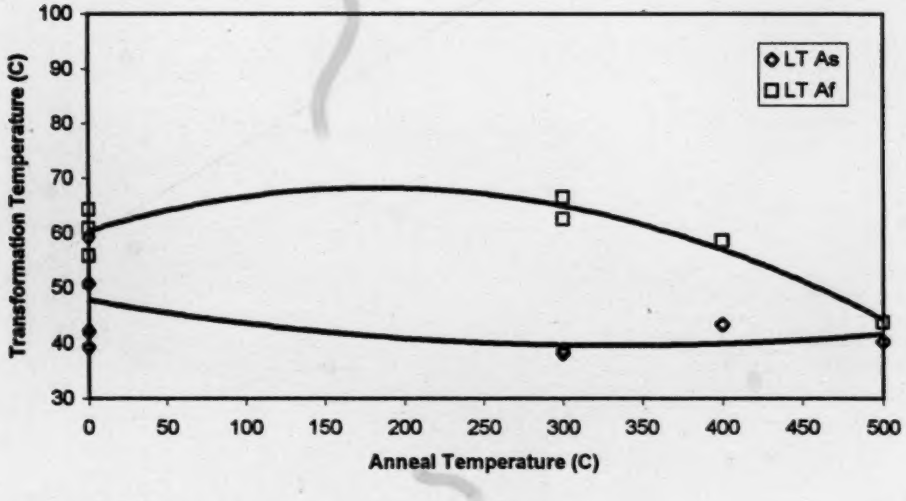

Figure 5.12: Transformation Temperature of Flexinol™ 250 μm Low Temperature SMA at Anneal Temperatures up to 500°C.

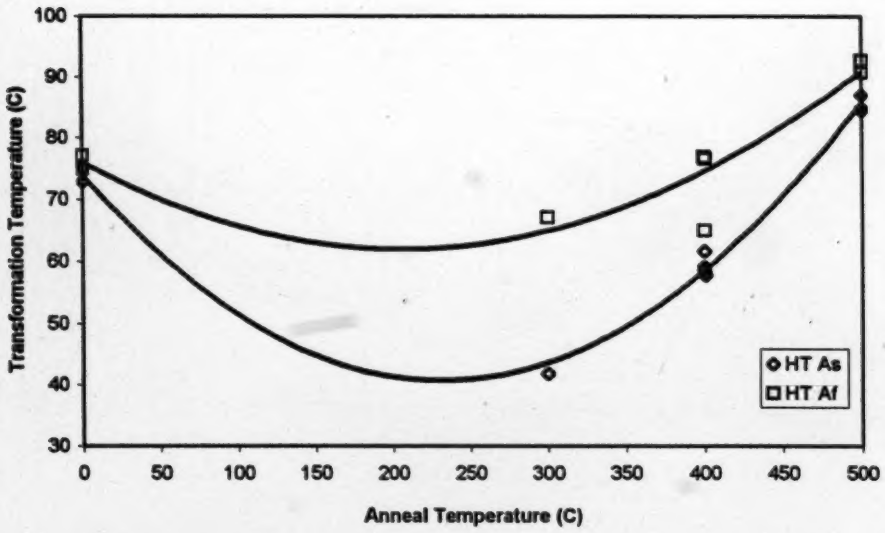

Figure 5.13: Transformation Temperatures for Flexinol™ 250um High Temperature SMA at Anneal Temperatures up to 500°C.

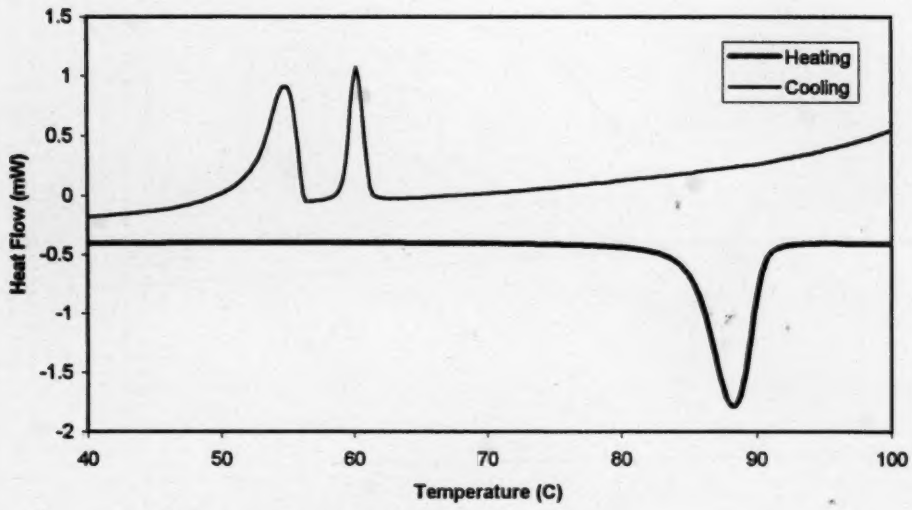

Figure 5.14: DSC Output for high temperature material annealed at 500°C for 15 minutes with Flexinol™ 250 μm High Temperature SMA.

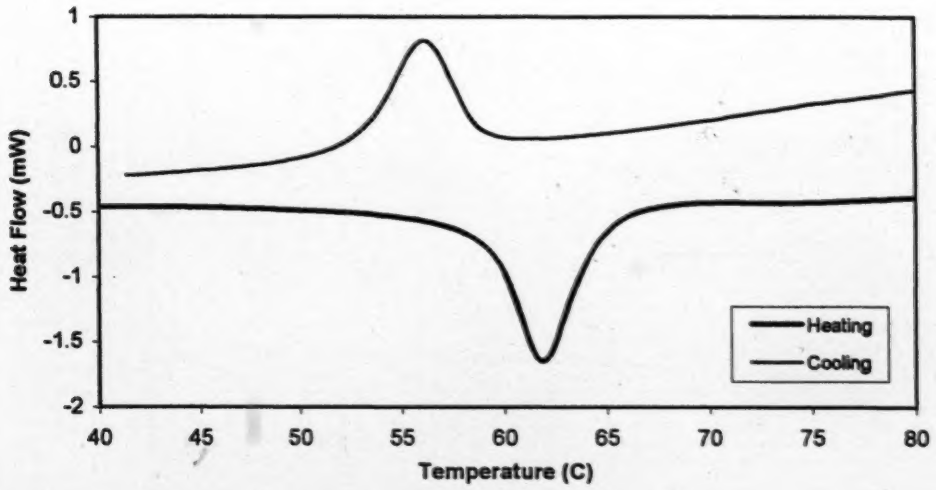

Figure 5.15: DSC Results for Thermomechanical Treatment of 400°C for 15 minutes with Flexinol™ 250 μm High Temperature SMA.

a)

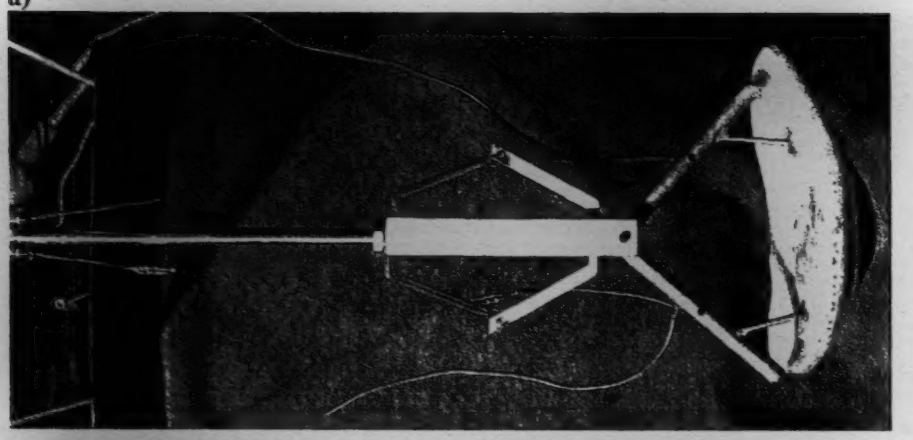

b)

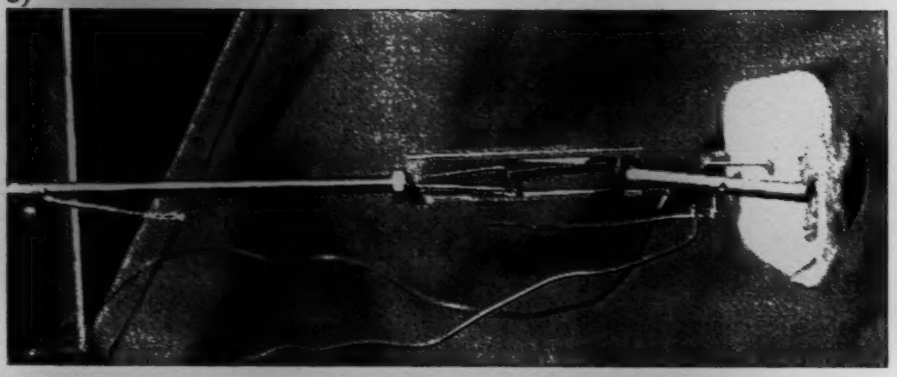

c)

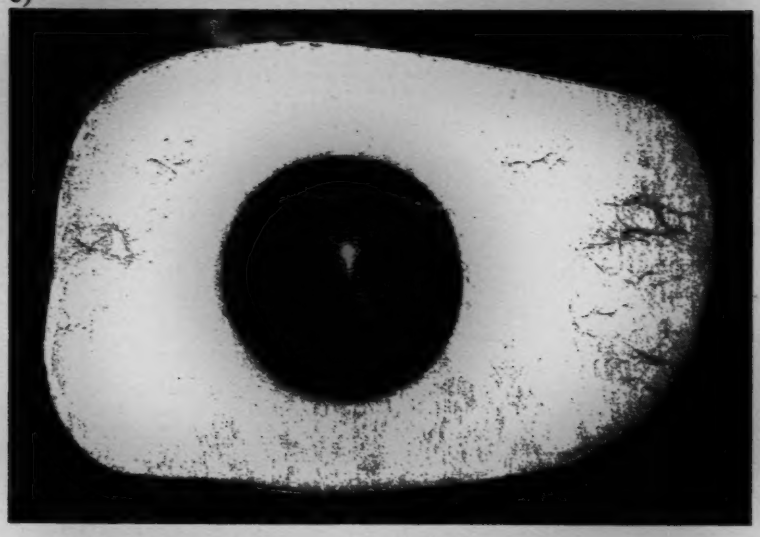

Figure 5.16: Photographs of the Prototype model from a) top, b) side and c) front views.

a)

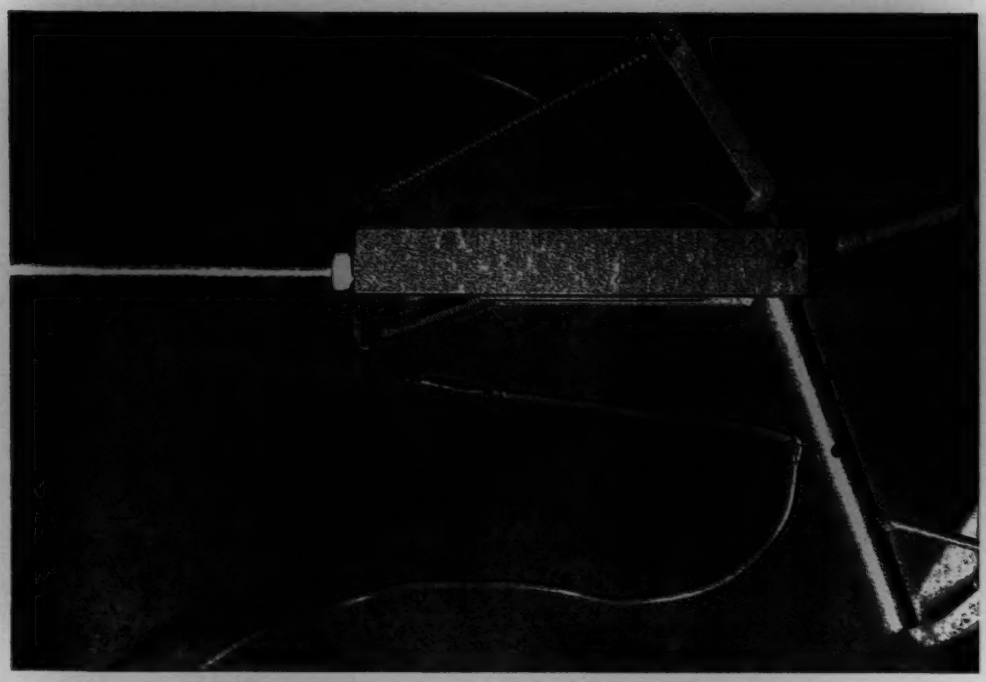

b)

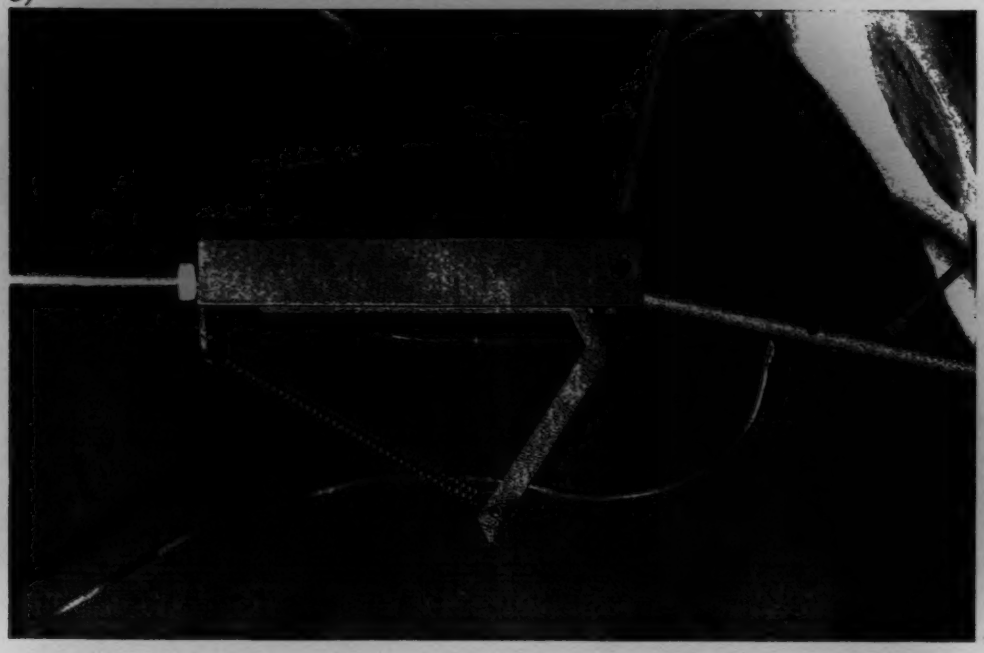

Figure 5.17: Top view of prototype in active state a) in one direction and b) in other direction

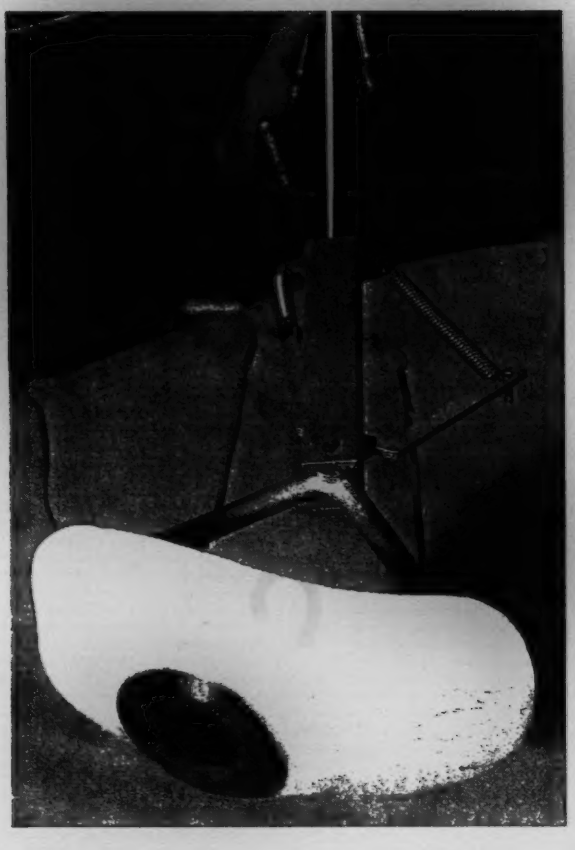

Figure 5.18: Full view of active system

6 Conclusions and Future Research

The quality of life of patients at COMPRU who wear an orbital prosthesis would be improved if their prosthesis were made more realistic by means of vertical and horizontal motion. Both an appropriate actuation and control system are required to create an intelligent prosthesis. A method of actuation that fit the design criteria as described by COMPRU was not available. This thesis developed a system which adhered to the criteria, as well as followed the design philosophy of biomimicry, simplicity and space optimization. Various methods of actuation were considered, and shape memory alloys were chosen for their high power density, high actuation forces and high displacements. The behaviour of shape memory alloys as an actuator was investigated by means of the force obtained, the transformation temperatures and the processing. Pulse width modulation was chosen to control the SMA springs. A prototype model was constructed to validate the design.

6.1 Conclusions of Current Work

Shape memory alloys in the form of springs have been shown to be a possible actuator for the intelligent prosthetic eye. They contract when heated, and return to their original length when cooled, which simulates the contraction of a muscle - a concept of biomimicry. Because SMA can be shaped, the wires are thermomechanically treated to form a spring. The design is simple as the number of components is minimal, and as such, space is optimized.

The force obtained by SMA springs is a function of the number of turns of the spring, the amount of extension and the current input. As the number of turns decreases, the force available for actuation increases, however, the shear strain cycle increases. This increase will reduce the life of the spring.

Control of the SMA actuator was applied by pulse width modulation. A combination of frequency, duty cycle and current input can provide for various actuation force magnitudes and duration, which act to move the eye in a more realistic manner. Low frequencies cause step-like contractions of the SMA spring which can be used to simulate quick cyclic eye patterns. As the duty cycle decreases, the speed of actuation decreases, which is due to the decrease in effective current.

The transformation temperatures of SMA are very sensitive to both thermomechanical treatment and manufacturing processing. When the anneal temperature is less than 20 minutes, there is no significant variation in transformation temperature for the same annealing temperature. A metastable phase, which is dependent on the alloy composition, depresses the transformation temperatures only in the region where this phase exists. It was not desirable to have this phase present for the actuator application, as the transformation temperatures were depressed beyond the design specifications. The high

temperature material was found to have more repeatable values in the transformation temperature range desired for the actuator application.

The prototype functioned well in that it revealed that shape memory alloys were a potential actuation system for the intelligent prosthetic eye. The model was successful in that the objectives of ±30° eye rotation were met, and that other angles could be achieved with the implementation of variable control.

6.2 Future Research

Since the prototype model was successful, a real-size model should be constructed. The model will be sized appropriately to a shell that can fit into the orbital cavity. The springs will be made from 100 μm diameter high temperature wire. This was chosen because the wire diameter is sufficiently small such that cooling occurs in less than 0.5 s in still air. The mechanical support structure should be constructed such that the posts are tubes and not solid, to reduce the overall weight. This will reduce the moment of inertia that will act to increase the angular acceleration of the unit.

Shape memory alloys doped with 10 at.% Cu have been shown to have better mechanical properties for use in actuation systems, as well as prolonged life (Waram, 1993). This material could not be obtained for testing in this thesis, but should be considered with further development. In addition, shape memory polymers are being developed (Hayashi, 1995) which may be possible substitutes to spring formation though thermomechanical means.

Integration of the actuator and the control system is key to the success of the project. As mentioned, Grant and Hayward (1997, 2000) are assigning a significant portion of their research to the control of the non-linear SMA. Majima, Kodama and Hasegawa (2001) developed a proportional integration

differential (PID) controller for a bias-type SMA actuator that incorporates the material hysteresis into the system. The problem of control of the SMA is being investigated by researchers proficient in electrical engineering.

The pulse width modulation and the accessory circuitry can be miniaturized to fit into the orbital space. A method of delivering power is required, as shape memory alloys require a significant amount of current, which would continually draw on a battery. However, the limiting road block of the project at this time is the power requirements. Currently, no rechargeable battery that fits into the dimensions of the orbit exists.

A sensor is required to measure the angle of rotation in order to provide feedback to the controller. García-Córdova, López-Coronado, and Guerrero-González (1999) are developing an anthropomorphic finger using shape memory alloys, and have used Hewlett-Packard HEDS-9040 optical encoders at each finger joint. This technology could be used at the pivot point and V-support to measure the angle the ocular element has rotated.

Movement in both the vertical and horizontal planes could be achieved by replacing the cup and cone joint with a ball and socket joint. The SMA spring system could be duplicated in the vertical plane. However, several problems arise, such as maintaining the neutral position with 3 degrees of freedom, as opposed to just one.

In-vivo and in-vitro testing of the system would be required. An ethics approval would be necessary to implement the actuation and control systems on a patient.

References

Amalraj JJ, Bhattacharyya A, Faulkner MG, *Finite-element modeling of phase transformation in shape memory alloy wires with variable material properties*, Smart Materials and Structures, 2(2002): 622-631.

Bandyopadhyay K, *Smart Materials and aerospace structures*, Proc. of SPIE Int. Soc. for Optical Engineering, 3903(1999): 312-324

Bar-Cohen Y, Xue T, Joffe B, Lih SS, Shahinpoor M, Simpson J, Smith J, Willis P, *Electroactive Polymers Low Mass Muscle Actuators*, SPIE International Conference, Smart Structures and Materials Symposium, San Diego, CA, 3-6 March 1997.

Benyus JM, Biomimicry: innovation inspired by nature, Quill, NY, 1997.

Brinson LC, *One-Dimensional Constitutive Behaviour of Shape Memory Alloys: Thermomechanical Derivation with Non-Constant Material Functions and Redefined Martensite Internal Variable*, J. Int. Mat. Sys. and Struc., Vol. 4, 1993, pp.229-242.

Clark CR, Marcelli DP, *Shape Memory Alloy Actuator Fatigue Properties*, SPIE Conf. Smart Materials Technologies, 3675(1999): 311-320.

Cunfu H, Bin W, Baoqi T, Jiang J, *Theoretical and experimental studies of torsion deformation of a thin-walled tube with wound and pasted shape memory alloy wires*, Smart Mater. Struct., 9, 2000, pp.660-664.

Dieter GE, Mechanical Metallurgy, New York, N.Y. : McGraw-Hill, 1961.

Dobelle WH, *Artificial Vision for the Blind by Connectivg a Television Camera to the Visual Cortex*, ASAIO Journal 2000, 3-9.

Galante T, Frank J, Bernard J, Chen W, Lesieutre A, Koopman GH, *Design, Modeling, and Performance of a High Force Piezoelectric Inchworm Motor*, J. Int. Mat. Sys. Struct., 10(1999): 962-972.

García-Córdova F, López-Coronado J, Guerrero-González A, *Design of an anthropomorphic finger using shape memory alloy springs*, IEEE, (1999): 794-799.

Grant D, *Shape Memory Alloy Actuator with and Application to a Robotic Eye*, Masters Thesis, Dept. of Electrical Engineering, McGill University, February 1995.

Grant D, Hayward V, *Variable Structure Control of Shape Memory Alloy Actuators*, IEEE Control Systems, (1997): 80-88.

Grant D, Hayward V, *Constrained Force Control of Shape Memory Alloy Actuators*, IEEE Int. Conf. on Robotics and Automation, San Francisco, CA, (2000): 1314-1320.

Gray H, Anatomy of the Human Body, 1918, (www.bartleby.com/107/227.html)

Gu JJ, Meng M, Cook A, Faulkner MG, *A study of natural eye movement detection and ocular implant movement control using processed EOG signals*, Proceedings IEEE International Conference on Robotics and Automation, v2, 2001, pp.1555-1560.

Hayashi S, Kondo S, Kapadia P, Ushioda E, *Room Temperature Functional Shape Memory Polymers*, Plastics Engineering, v51, n2(1995): 29-31

Histand MB, Alciatore DG, Introduction to Mechatronics and Measurement Systems, WCB/McGraw-Hill, 1999

Homma D, Miwa, Y, Iguchi N, *Micro Robots and Micro Mechanisms Using Shape Memory Alloy*, Integrated Micro-Motion Systems - Micromaching, Control and Applications, Elsevier Science Publishers, 1990.

Honda M, Niimi A, Ueda M, *New Orbital Prosthesis with a Blinking Eyelid: Report of a Case*, J. Oral and Maxillofacial Surgery, 57(1999): 730-733.

http://www.micromo.com

http://www.nanomuscle.com

http://www.sma-inc.com

Incropera FP, DeWitt DP, Fundamentals of Heat and Mass Transfer, John Wiley & Sons, Inc., USA, 1996.

Klein M, Menneking H, Schmitz H, Locke HG, Bier J, *A new generation of facial prostheses with myoelectrically driven moveable upper lid*, The Lancet, 353(May 1, 1999): 493.

Klein M, Menneking H, Schmitz H, Locke HG, Bier J, *A New Orbital Prosthesis with a Mobile Upper Eyelid*, J. Facial and Somato Prosthetics, 11-17.

Koga A, Suzumori K, Sudo H, Iikura S, Kimura M, *Electrostatic Linear Microactuator Mechanism for Focusing a CCD Camera*, J. Lightwave Technology, 17:1(1999): 43-47.

Kube J, Zoeppig V, Hermann R, Hoffmann A, Kallenbach E, *Electromagnetic miniactuators using thin magnetic layers*, Smart Mat. Struct. 9(2000): 336-341.

Liang C, Rogers CA, *One-Dimensional Thermomechanical Constitutive Relations for Shape Memory Materials*, J. Int. Mat. Sys.Struct., 1990, vol 1(2), pp.207-234.

Liang C, Rogers CA, *Design of Shape Memory Alloy Actuators*, J. Mech. Design, 114(1992): 223-230.

Liang C, Rogers CA, *Design of Shape Memory Alloy Springs With Applications in Vibration Control*, J. Vibration and Acoustics, 115(1993): 129-135.

Liu C, Bar-Cohen Y, Leary S, *Electro-statically stricted polymers (ESSP)*, SPIE Conf. Electroactive Polymer Actuators and Devices, 3669(March 1999): 186-190.

Majima S, Kodama K, Hasegawa T, *Modeling of Shape Memory Alloy Actuator and Tracking Control System with the Model*, IEEE Transactions on Control Systems Technology, 9(January 2001): 54-59.

Mihálcz I, *Fundamental Characteristics and Design Method for Nickel-Titanium Shape Memory Alloy*, Periodica Polytechnica Ser. Mech. Eng., v45, 1(2001): 75-86.

Miranda EG, Habakuk SW, *Artificial Movement as Applied to Prostheses of the Orbit: A Literature Review*, J. Facial and Somoto Prosthetics, v6,2(2000): 95-108.

Mondo-Tronics Robot Store Catalog 20

Reynaerts D, Van Brussel H, *Design Aspects of shape memory actuators*, Mechatronics, 8(1998): 635-656.

Shigley JE, Mischke CR, Series in Mechanical Engineering. McGraw-Hill, New York, 1989, pg. 413-445.

Srinivasan AV, Smart Structures: Analysis and Design, Cambridge University Press, 2001

Stevens CG, *Designing Shape Memory Alloy Springs for Linear Actuators*, Springs Magazine, 1998.

Tabib-Azar M, Microactuators, Kluwer Academic Publishers, USA, 1998

Tanaka K, *A Thermomechanical Sketch of Shape Memory Effect: One Dimensional Tensile Behavior*, Res. Mech., vol 18, 1986, pp.251-263.

Torii A, Kato H, Ueda A, *A Miniature Actuator with Electromagnetic Elements*, Electrical Engineering in Japan, 134: 4(2001): 40-45.

Treppmann D, Hornbogen E, *On the Influence of Thermomechanical Treatments on Shape Memory Alloys*, J. Phys IV France 7, 1997, Colloque C5, pp.211-220.

Waram T, Actuator Design Using Shape Memory Alloys, 2nd Ed., T.Waram, Canada, 1993.

Witting JH, Ayers J, Safak K, *Development of a biomimetic underwater ambulatory robot: advantages of matching biomimetic control architecture with biomimetic actuators*, Sensor Fusion and Decentralized Control in Robotic Systems III, Proceedings of SPIE, 4196(2000): 54-61.

APPENDIX A:

Detailed Analysis of Heat Transfer Coefficient

Reference: Incropera and DeWitt (1996)

The heat transfer coefficients can be estimated considering the average convection coefficient, h. It is customary to express the convection coefficient in a non-dimensional form called the Nusselt number, Nu, as shown in A.1. This equation also includes the thermal conductivity of the fluid, k_f, and the diameter of the wire in the model, D.

$$Nu = \frac{hD}{k_f} \qquad \text{(A.1)}$$

The air inside the prosthesis can be considered as stagnant, so that the correlations will follow free convection behaviour. The parameter governing free convection problems is the Grashof number, Gr, and the Rayleigh number, Ra. The relationship for the Grashof number is shown in A.2 as a function of the gravitational acceleration, g, the volumetric thermal expansion of the fluid, β, the temperature of both the element (T) and the surroundings (T_∞), the diameter of the wire, D, and the kinematic viscosity of the fluid, υ. The kinematic viscosity is defined as the ratio between the dynamic viscosity of the fluid, μ, and the density of the fluid, ρ.

$$Gr = \frac{g\beta(T - T_\infty)D^3}{\upsilon^2} \qquad \text{(A.2)}$$

The Rayleigh number, shown in A.3, is the product of the Grashof number and the Prandtl number, Pr. The Prandtl number is determined for air under standard conditions to be ≈ 0.7.

$$Ra = Gr\,\mathrm{Pr} \tag{A.3}$$

The Nusselt number for free convection for a cylinder is shown in A.4, with the condition that the Rayleigh number is greater than 10^{-5} and less than 10^{12}. The convection coefficient can now be determined from A.1 and A.4.

$$Nu = \left\{ 0.60 + \frac{0.387 Ra^{\frac{1}{4}}}{\left[1 + \left(\frac{0.559}{\mathrm{Pr}} \right)^{\frac{9}{16}} \right]^{\frac{8}{27}}} \right\}^2 \tag{A.4}$$

However, the prototype model will have a wire with a larger diameter than the actual model. As such, the heat transfer for the prototype spring and the actual spring will be considerably different. To ensure that the convection coefficients are the same for both models, forced convection correlations will have to be used for the larger diameter wire to determine the velocity of the air for the prototype spring which will bring about the same convection coefficient as the stagnant smaller real-sized model.

The number which is similar to the Rayleigh number in forced convection is the Reynolds number, *Re*, a dimensionless number shown in A.5, which is a function of the density of the fluid, ρ, the velocity of the fluid, V, the diameter of the wire, D, and the dynamic viscosity of the fluid, μ.

$$\mathrm{Re} = \frac{\rho V L}{\mu} \tag{A.5}$$

The Nusselt number for forced convection over a cylinder with Prandtl number greater than 0.2 is shown in A.6.

$$Nu = 0.3 + \frac{0.62\,\mathrm{Re}^{\frac{1}{2}}\,\mathrm{Pr}^{\frac{1}{3}}}{\left[1+\left(\frac{0.4}{\mathrm{Pr}}\right)^{\frac{2}{3}}\right]^{\frac{1}{4}}}\left[1+\left(\frac{\mathrm{Re}}{282000}\right)^{\frac{5}{8}}\right]^{\frac{4}{5}} \qquad \text{(A.6)}$$

The factors that can be varied are the geometry and temperature of the wire. The cross-sectional area of the wire is circular and to maximize heat transfer the wire should have the smallest diameter possible taking into consideration the force requirements.

APPENDIX B:

Validation of Negligible Deflection at Cantilever Beam End

To verify that the deflection at the end of the beam due to the reaction force of the spring is negligible, a cantilever beam moment analysis was conducted. This determined the deflection at Point B, q_B, due to the force of the SMA. A free body diagram of the beam is shown in Figure B.1 where Point A is fixed and Point B is attached to the SMA spring.

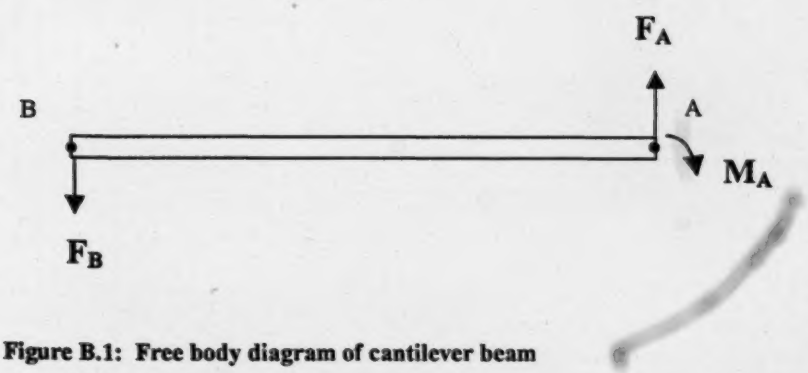

Figure B.1: Free body diagram of cantilever beam

Isolating the beam at point B, shown in Figure B.2, and taking the moment around point B allows the deflection to be determined using Castigliano's Theorem, shown in B.1. The distance from the end of the beam at point B to the site of the moment balance is z. The moment is a function of the distance z, and is shown in B.2.

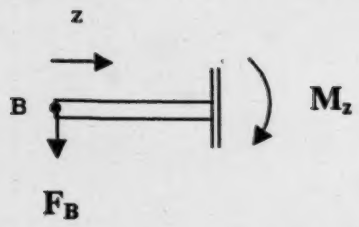

Figure B.2: Beam isolated at a distance z from the free end B

$$q_B = \frac{1}{EI}\int_0^l M \frac{dM}{dF_B} dz \qquad \text{(B.1)}$$

$$M(z) = F_B z$$
$$\frac{dM}{dF_B} = z \qquad \text{(B.2)}$$

By completing the integral shown in B.1, an analytical solution for the deflection is shown in B.3.

$$q_B = \frac{Fl^3}{3EI} \qquad \text{(B.3)}$$

The dimensions and material properties of the cantilever beam used for the experiments are shown in Table B.1. The equations used for the calculation of the moment of inertia, I, were such that the cross section of the beam was rectangular.

l (mm)	w (mm)	t (mm)	E (GPa)	I (mm^4)
105.1	10.1	1.747	68.9	149.9

Table B.1: Physical properties of the cantilever beam

The relationship between the deflection of the beam and the recovery force of the SMA spring is shown in B.4. When the forces are on the order of 0.5 N, the deflection incurred is 0.0187 mm. The amount of total extension to obtain 0.5 N was 20 mm for Spring 250-2.38-20. The percent of the total extension due to deflection of the cantilever beam would be 0.09%.

$$q_B = 0.0374F \tag{B.4}$$

APPENDIX C:

Electrical PWM circuit diagrams

The circuit diagram, shown in Figure C1, contains the components listed in Table C1.

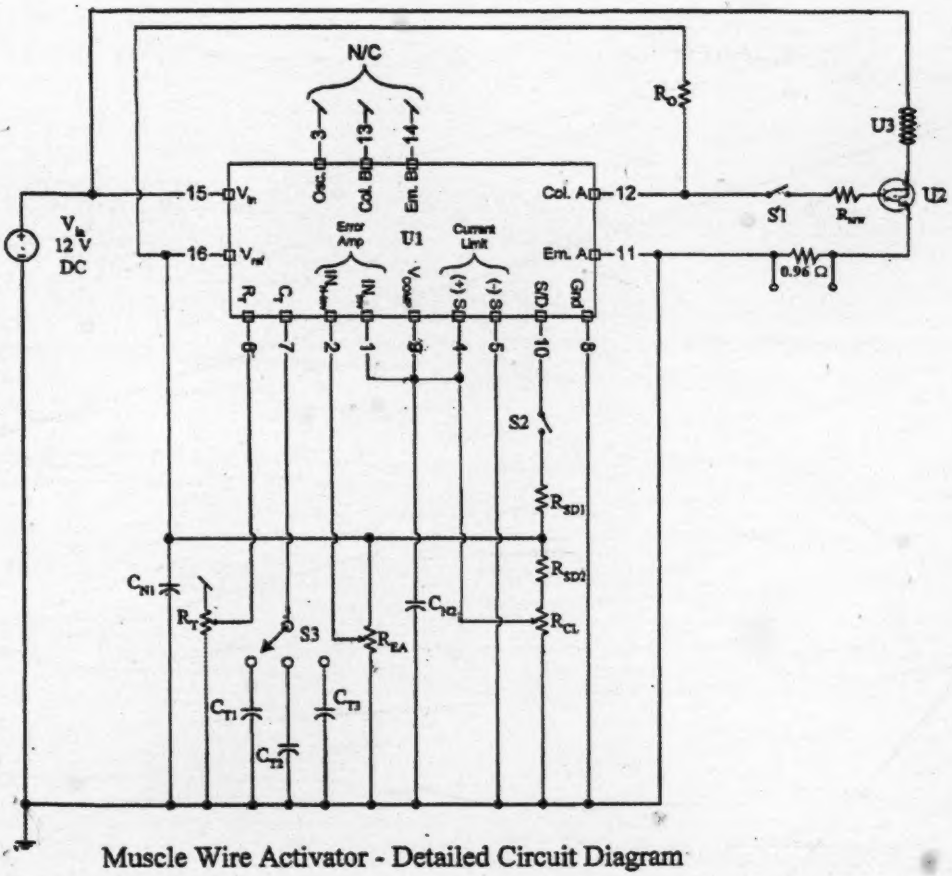

Muscle Wire Activator - Detailed Circuit Diagram

Figure C1: Circuit diagram for Pulse Width Modulation Control of SMA Spring

Symbol	Part	Description
U1	UC3524AN	Voltage Regulating Pulse Width Modulator
U2	ECG272	Darlington Power Transistor
U3	SMA Wire	
S1	On-Off Miniature Bat Handle Toggle (5A, 120V)	Muscle Wire Circuit Enable Switch
S2	On-Off Miniature Bat Handle Toggle (5A, 120V)	PWM Shutdown Switch
S3	Selector taken from old stereo system	Oscillator Capacitor Selector Switch
V_{in}	12 V DC	12 V DC Voltage Supply
C_{N1}	0.1 µF 50 V ± 10% Axial Monolithic	VREF Noise Capacitor
C_{T1}	0.1 µF 50 V ± 5% Dip Ceramic	Oscillator Timing Capacitor #1
C_{T2}	1 µF ± 10% Dip Ceramic	Oscillator Timing Capacitor #2
C_{T3}	10 µF 50 V ± 10% Military Ceramic	Oscillator Timing Capacitor #3
C_{N2}	0.1 µF 50 V ± 10% Axial Monolithic	VCOMP Noise Capacitor
R_T	Trimmer Potentiometer 200 kΩ, 20 Turn 3006P-1-204	Oscillator Timing Potentiometer
R_{EA}	Trimmer Potentiometer 10 kΩ, 24 Turn 3299W-1-103	Error Amplifier Control Potentiometer
R_{SD1}	2 kΩ, 1% Metal Film, 0.25 W	PWM Shutdown Resistor #1
R_{SD2}	6200 Ω, 1% Metal Film, 0.25 W	PWM Shutdown Resistor #2
R_{CL}	Trimmer Potentiometer 1 kΩ, 24 Turn 3296W-1-102	Current Limit Control Potentiometer
R_O	2.2 kΩ, 2% Metal Film, 1 W	Output Resistor (2 in parallel)
R_{MW}	10 kΩ and 50 kΩ pot	Muscle Wire Current Limiting Resistor

Table C1: Components for Circuit in Pulse Width Modulation of SMA spring

The specifications for the PWM unit are detailed in the following pages.

ABSOLUTE MAXIMUM RATINGS

Supply Voltage (V_{IN}) 40V
Collector Supply Voltage (V_C) 60V
Output Current (each Output) 200mA
Maximum Forced Voltage (Pin 9, 10) ..... -3 to +5V
Maximum Forced Current (Pin 9, 10) ..... ±10mA
Reference Output Current 50mA
Oscillator Charging Current 5mA
Power Dissipation at T_A = +25°C 1000mW
Power Dissipation at T_C = +25°C 2000mW
Operating Temperature Range ..... -55°C to +125°C
Storage Temperature Range ..... -65°C to +150°C
Lead Temperature, (Soldering, 10 seconds) ..... +300°C
Note: Consult packaging section of Databook for thermal limitations and considerations of package.

DIL-16, SOIC-16 (TOP VIEW)
J or N Package, DW Package

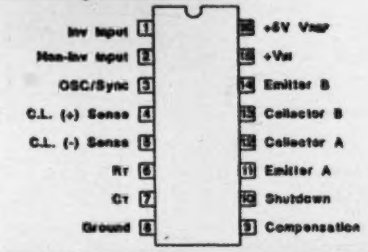

CONNECTION DIAGRAMS

PLCC-20, LCC-20 (TOP VIEW)
Q or L Package

PACKAGE PIN FUNCTION	
FUNCTION	PIN
N/C	1
Inv. Input	2
Non-Inv. Input	3
OSC/SYNC	4
C.L. (+) sense	5
N/C	6
C.L. (-) sense	7
R_T	8
C_T	9
Ground	10
N/C	11
Compensation	12
Shutdown	13
Emitter A	14
Collector A	15
N/C	16
Collector B	17
Emitter B	18
+V_{IN}	19
+5V V_{REF}	20

ELECTRICAL CHARACTERISTICS: Unless otherwise stated, these specifications apply for T_A = -55°C to +125°C for the UC1524A, -25° to +85°C for the UC2524A, and 0°C to + 70°C for the UC3524A; V_{IN} = V_C = 20V, T_A = T_J.

PARAMETER	TEST CONDITIONS	UC1524A / UC2524A			UC3524A			UNITS
		MIN	TYP	MAX	MIN	TYP	MAX	
Turn-on Characteristics								
Input Voltage	Operating Range after Turn-on	8		40	8		40	V
Turn-on Threshold		6.5	7.5	8.5	6.5	7.5	8.5	V
Turn-on Current	V_{IN} = 6V		2.5	4		2.5	4	mA
Operating Current	V_{IN} = 8 to 40V		5	10		5	10	mA
Turn-on Hysteresis*			0.5			0.5		V
Reference Section								
Output Voltage	T_J = 25°C	4.95	5.00	5.05	4.90	5.00	5.10	V
	Over Operating Range	4.9		5.1	4.85		5.15	V
Line Regulation	V_{IN} = 10 to 40V		10	20		10	30	mV
Load Regulation	I_L = 0 to 20 mA		20	25		20	35	mV
Temperature Stability*	Over Operating Range*		20	25		20	35	mV
Short Circuit Current	V_{REF} = 0, 25°C ≤ T_J ≤ 125°C		80	100		80	100	mA
Output Noise Voltage*	10Hz ≤ f ≤ 10kHz, T_J =25°C		40			40		μVrms
Long Term Stability*	T_J =125°C, 1000 Hrs.		20	50		20	50	mV

* *These parameters are guaranteed by design but not 100% tested in production.*

ELECTRICAL CHARACTERISTICS: Unless otherwise stated, these specifications apply for T_A = -55°C to +125°C for the UC1524A, -25° to +85°C for the UC2524A, and 0°C to + 70°C for the UC3524A; V_{IN} = V_C = 20V, T_A = T_J.

PARAMETER	TEST CONDITIONS	UC1524A / UC2524A			UC3524A			UNITS
		MIN	TYP	MAX	MIN	TYP	MAX	
Oscillator Section (Unless otherwise specified, R_T = 2700Ω, C_T = 0.01 mfd)								
Initial Accuracy	T_J = 25°C	41	43	45	39	43	47	kHz
	Over Operating Range	40.2		45.9	38.2		47.9	kHz
Temperature Stability*	Over Operating Temperature Range		1	2		1	2	%
Minimum Frequency	R_T = 150kΩ, C_T = 0.1mfd			140			120	Hz
Maximum Frequency	R_T = 2.0kΩ, C_T = 470pF	500			500			kHz
Output Amplitude*		3	3.5		3	3.5		V
Output Pulse Width*		0.29	0.5	1.0	0.3	0.5	1.0	µs
Ramp Peak		3.3	3.5	3.7	3.3	3.5	3.7	V
Ramp Valley	T_J = 25°C	0.7	0.8	0.9	0.7	0.8	0.9	V
Ramp Valley T.C.			-1.0			-1.0		mV/°C
Error Amplifier Section (Unless otherwise specified, V_{CM} = 2.5V)								
Input Offset Voltage			0.5	5		2	10	mV
Input Bias Current			1	5		1	10	µA
Input Offset Current			.05	1		0.5	1	µA
Common Mode Rejection Ratio	V_{CM} = 1.5 to 5.5V	70	80		70	80		dB
Power Supply Rejection Ratio	V_{IN} = 10 to 40V	70	80		70	80		dB
Output Swing (Note 1)		5.0		0.5	5.0		0.5	V
Open Loop Voltage Gain	ΔVo= 1 to 4V, R_L ≥ 10MΩ	72	80		64	80		dB
Gain-Bandwidth*	T_J = 25°C, Av = 0dB	1	3		1	3		MHz
DC Transconductance*§	T_J = 25°C, 30kΩ ≤ R_L ≤ 1MΩ	1.7	2.3		1.7	2.3		mS
P.W.M. Comparator (R_T = 2kΩ, C_T = 0.01mfd)								
Minimum Duty Cycle	V_{COMP} = 0.5V			0			0	%
Maximum Duty Cycle	V_{COMP} = 3.8V	45			45			%
Current Limit Amplifier (Unless otherwise specified, Pin 5 = 0V)								
Input Offset Voltage	T_J = 25°C, E/A Set for Maximum Output	190	200	210	180	200	220	mV
	Over Operating Temperature Range	180		220	170		230	mV
Input Bias Current			-1	-10		-1	-10	µA
Common Mode Rejection Ratio	$V_{(pin\ 5)}$ = -0.3V to + 5.5V	50	60		50	60		dB
Power Supply Rejection Ratio	V_{IN} = 10 to 40V	50	60		50	60		dB
Output Swing (Note 1)	Minimum Total Range	5.0		0.5	5.0		0.5	V
Open-Loop Voltage Gain	ΔVo = 1 to 4V, R_L ≥ 10MΩ	70	80		70	80		dB
Delay Time*	Pin 4 to Pin 9, ΔV_{IN} = 300mV		300			300		ns
Output Section (Each Output)								
Collector Emitter Voltage	I_C = 100µA	60	80		60	80		V
Collector Leakage Current	V_{CE} = 50V		.1	20		.1	20	µA

** These parameters are guaranteed by design but not 100% tested in production.*

§ DC transconductance (gM) relates to DC open-loop voltage gain according to the following equation: Av = gMRL where RL is the resistance from pin 9 to the common mode voltage.

The minimum gM specification is used to calculate minimum Av when the error amplifier output is loaded.

Note 1: Min Limit applies to output high level, max limit applies to output low level.

ELECTRICAL CHARACTERISTICS: Unless otherwise stated, these specifications apply for T_A = -55°C to +125°C for the UC1524A, -25° to +85°C for the UC2524A, and 0°C to + 70°C for the UC3524A; V_{IN} = V_C = 20V. T_A = T_J.

PARAMETER	TEST CONDITIONS	UC1524A / UC2524A			UC3524A			UNITS
		MIN	TYP	MAX	MIN	TYP	MAX	
Output Section (cont.) (Each Output)								
Saturation Voltage	I_C = 20mA I_C = 200mA		.2 1	.4 2.2		.2 1	.4 2.2	V V
Emitter Output Voltage	I_E = 50mA	17	18		17	18		V
Rise Time*	T_J = 25°C, R = 2kΩ		120	400		120	400	ns
Fall Time*	T_J = 25°C, R = 2kΩ		25	200		25	200	ns
Comparator Delay*	T_J = 25°C, Pin 9 to output		300			300		ns
Shutdown Delay*	T_J = 25°C, Pin 10 to output		200			200		ns
Shutdown Threshold	T_J = 25°C, R_C = 2kΩ	0.6	.7	1.0	0.6	.7	1.0	V
S/D Threshold Over Temp.	Over Operating Temperature Range	0.4		1.2	0.4		1.0	V
Thermal Shutdown*			165			165		°C

** These parameters are guaranteed by design but not 100% tested in production.*

OPEN-LOOP CIRCUIT

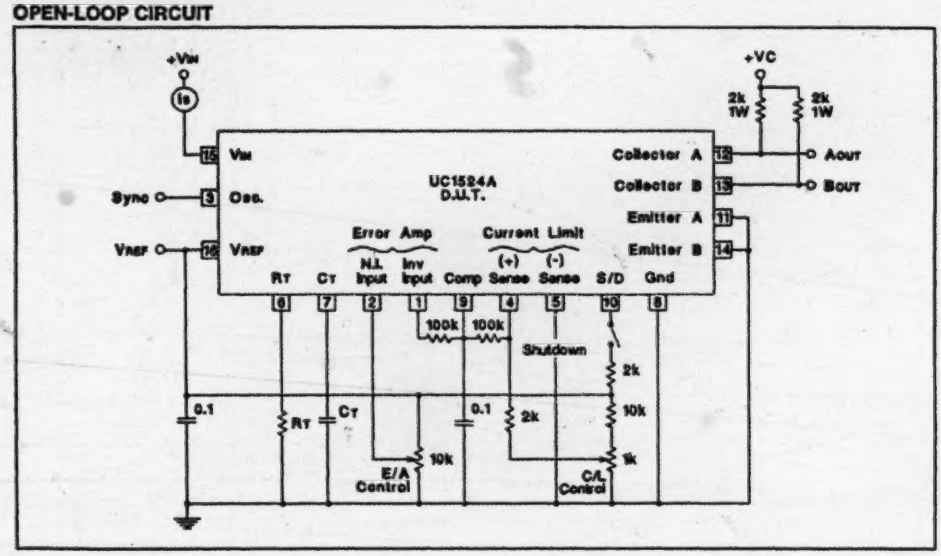

BLOCK DIAGRAM

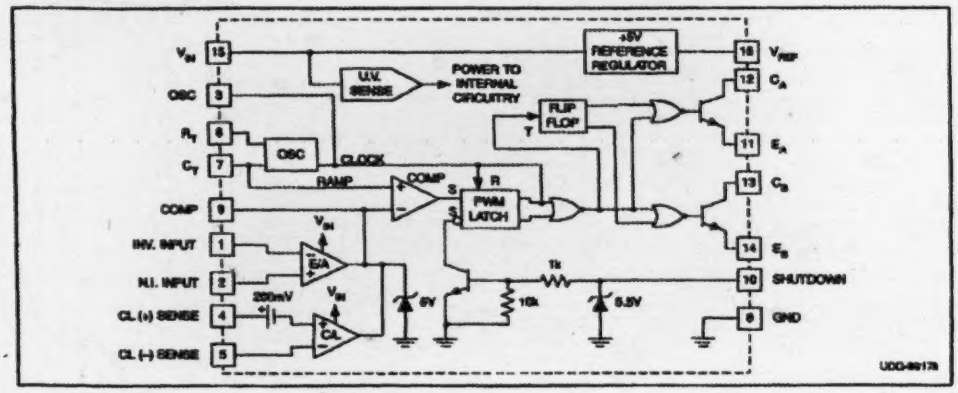

APPENDIX D:

CAD drawings of prototype design

Isometric view of support structure and v-brace

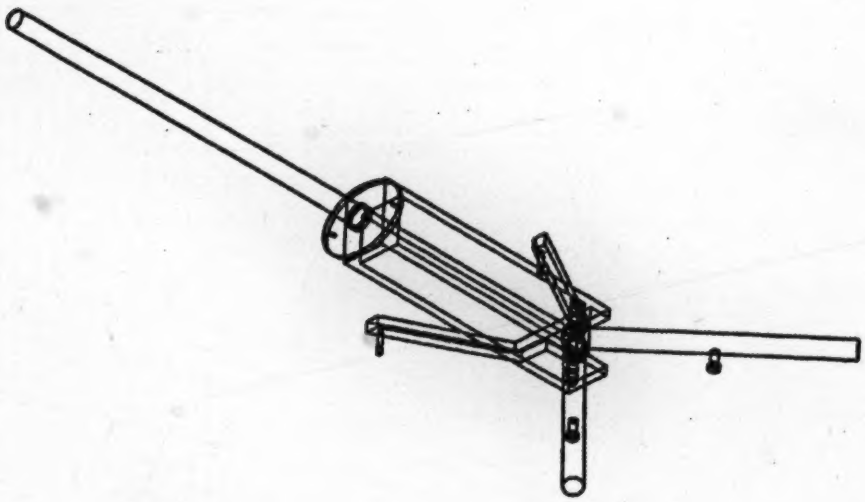

Engineering drawing of support structure, made of stainless steel, dimensions in mm

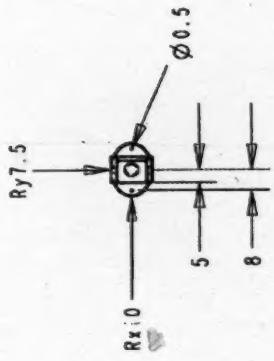

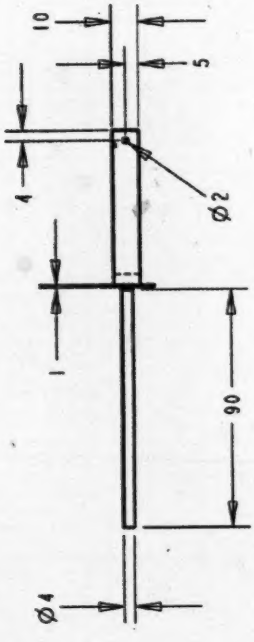

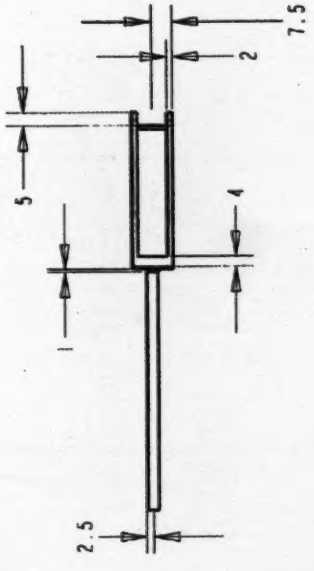

Engineering drawing of v-brace, made of stainless steel, dimensions in mm.